

AN ABSTRACT OF THE DISSERTATION OF

Barath Palanisamy for the degree of Doctor of Philosophy in Industrial Engineering,
presented on June 17, 2013.

Title: Micromixer Assisted Continuous Flow Synthesis of Nanoparticles of Binary Compounds and their Application

Abstract approved:

Brian K Paul

In this work, continuous synthesis routes for binary nanoparticles using advantages of microchannel mixing (low diffusion distances and higher mass transfer) and fast heating rates provided by ultrasound induced heating are investigated. In addition, the application of silica nanoparticles in anti-reflective coatings on glass and understanding the structure-property-performance correlation in these coatings is investigated.

Batch synthesis of nanoparticles often results in wide variation of particle size, less control over particle shape and involves long processing times along with creation of large volume of chemical waste. By carrying out mixing in a microchannel mixer for nanoparticle synthesis the above issues can be resolved. Engulfment flow in T-micromixers has been reported to be a good mixing condition at Reynolds no above 250 for water. Typical T-mixer based continuous synthesis chemistries use low flow rates with low throughputs and use flow regimes less than Re 250. At these regimes there is no mixing enhancement as the flow is still stratified and diffusion occurs only at the symmetry line where two fluid streams come in contact. While engulfment flow in T-shaped microchannel mixers has been shown to provide better mixing characteristics, very little work has been reported to date on exploiting these findings for nanoparticle synthesis. In this work, engulfment flow – mixing condition is used to drive ceria nanoparticle synthesis and control over particle size, shape and crystallinity is exhibited using this approach.

Processing becomes harder to control in batch synthesis especially when higher than room temperature reactions are involved in nanoparticle synthesis. The objective is to investigate the fast heating rates provided by cavitation in a liquid subjected to ultrasound exposure in a low volume continuous flow reactor for synthesis of cadmium sulfide nanoparticles. Batch synthesis of cadmium sulfide typically takes two hours for completion. Again, by employing an upstream mixing stage using a T-micromixer and subjecting the mixed reactants in small control volumes to high intensity ultrasound the processing time is reduced to less than a minute. Under comparison, continuous synthesis yields an average size of 22 nm with a coefficient of variation of 25% suggesting better process control. High aspect ratio nanoparticles in the shape of hexagonal platelets with uncommon cubic crystal structure for CdS were synthesized using this approach. Typically, temperatures above 800°C are used to produce high aspect ratio CdS nanoparticles and yields hexagonal crystal structure. This approach appears to stabilize the metastable cubic CdS.

While exhibiting better control over nanoparticle characteristics, to use these nanoparticles in an application requires investigating the fundamental correlation between structure-properties-processing. Synthesized silica nanoparticles used to develop gradient structure based anti-reflection coatings on glass substrates are evaluated. The term Biomimetics refers to replicating applications from nature. Motheyes have subwavelength structures that reduce reflection of light and ensure higher percentage of light transmitted for better vision. In this work, silica nanoparticle based anti-reflection coatings that have a gradient structure similar to motheye that are tuned towards solar cover glass applications are produced and studied. Since solar panels are exposed to elements of nature, optical performance has to be complemented by mechanical durability. Optical and abrasion performance are evaluated in light of the mechanical properties and physical structure of the films using mechanistic and statistical models. The results suggest that the mechanical performance of these gradient coatings can be modified without adversely affecting optical performance in the design of these coatings.

©Copyright by Barath Palanisamy
June 17, 2013
All Rights Reserved

Micromixer Assisted Continuous Flow Synthesis of Nanoparticles of Binary Compounds
and their Application

by
Barath Palanisamy

A DISSERTATION

submitted to

Oregon State University

in partial fulfillment of
the requirements for the
degree of

Doctor of Philosophy

Presented June 17, 2013
Commencement June 2014

Doctor of Philosophy dissertation of Barath Palanisamy presented on June 17, 2013.

APPROVED:

Major Professor, representing Industrial Engineering

Head of the School of Mechanical, Industrial and Manufacturing Engineering

Dean of the Graduated School

I understand that my dissertation will become part of the permanent collection of Oregon State University libraries. My signature below authorizes release of my dissertation to any reader upon request.

Barath Palanisamy, Author

ACKNOWLEDGEMENTS

I would like to thank all the numerous people who gave me support during these long four years of my PhD studies. Foremost, I would like to thank my parents and my brother for stimulating my intellectual thirst when I was a kid. Thanks to them for shaping my mindset into a highly self motivated individual.

My sincere thanks to my dissertation advisor Dr Brian Paul, for constantly providing me new technological directions for my research. His constant encouragement and inspiration kept me going relentlessly in my research. He is a great role model for a career in both research and academia. I thank him for his time on all the discussions we had which gave me directions and path forward around obstacles. Thanks to him for providing timely resources to complete my work.

I would also like to thank my dissertation committee, Professors Chih-Hung Chang, Karl Haapala, Sundar Atre and John Sessions for their invaluable time, suggestions, support and encouragement along the various stages of my doctoral studies.

I earnestly thank my lab colleagues past and present, Daniel Peterson, Anna Garrison and Dr Ravi Eluri for their valuable feedback and ideas that helped me along. I wish them the very best in their career endeavors. I would also like to thank Jack Rundell, Neill Thornton, Kevin Harada, Kathy Han, Jair Lizarazo-Adarme, Don Higgins, Shankar and Sudhir Ramprasad at MBI for their timely help in some of my experiments. I wish them a joyous life for them to continue helping others in need.

I would also like to thank Dr Yi Liu for training me on the transmission electron microscope and for being a great teacher. I would also like to thank Teresa Sawyer for her support in electron microscopy throughout my research. I would also like to thank Peter Eschbach for his patient demeanor and for training me well in the focused ion beam milling technique. I would like to thank Dr S.Y. Han for his help on using some of the processing and characterization tools.

I would like to thank all my numerous friends in Corvallis for being great people and helping me appreciate the world and keeping my life in balance.

I would like to dedicate this dissertation to my parents for being the source of all my energy and for bringing me up with values. I hope to keep them proud of me.

CONTRIBUTION OF AUTHORS

Dr Chih-Hung Chang assisted with interpreting some of the data in my second chapter on sonochemical synthesis of CdS nanoparticles. His insights helped broaden the understanding and bring out key contributions in this article.

TABLE OF CONTENTS

	<u>Page</u>
Chapter 1	1
1. Introduction	1
1.1 Mixing regimes in T-Mixers.....	2
2. Chapters.....	4
Chapter 1.....	4
Chapter 2.....	4
Chapter 3.....	5
3. References	7
Chapter 2.....	11
CONTINUOUS FLOW SYNTHESIS OF CERIA NANOPARTICLES USING STATIC T-MIXERS.....	11
Abstract	11
1. Introduction	11
2. Methods.....	14
2.1. Flow Conditions	14
2.2. Flow Chemistry	17
3. Experimental procedure	18
4. Results and discussion.....	19
5. Conclusions	31
6. Acknowledgements	32
7. References	33

TABLE OF CONTENTS (Continued)

	<u>Page</u>
Chapter 3.....	41
CONTINUOUS SONOCHEMICAL SYNTHESIS OF CADMIUM SULFIDE NANOPLATELETS USING AN AZEOTROPIC SOLVENT	
	41
Abstract	41
1. Introduction	41
2. Development of a continuous flow sonochemical reactor	47
3. Experimental methods.....	50
3.1. Bubble dynamics	51
3. Results and discussion.....	52
4. Conclusions	65
5. Acknowledgements	65
6. References	66
Chapter 4.....	69
THE ABRASION RESISTANCE OF SILICA NANOPARTICLE-BASED MOTHEYE ANTIREFLECTIVE COATINGS ON GLASS	
	69
Abstract	69
1. Introduction	70
1.1 Thin Film Mechanical Behavior.....	71
1.2 Models of Thin Film Mechanical Behavior	73
1.3 Factors Affecting the Mechanical Properties of Nanoparticle Thin Films.....	78
1.4 Objective.....	80
2. Experimental methods.....	80

TABLE OF CONTENTS (Continued)

	<u>Page</u>
3. Results and discussion.....	85
3.3. Understanding mechanical behavior	85
4. Conclusions	103
5. References	104
Appendix 1	107
Appendix 2	108

LIST OF FIGURES

<u>Figure</u>	<u>Page</u>
Figure 1. Flow regimes in a T-mixer	3
Figure 2. Flow transition in static T-mixer observed in CFD numerical simulation (a) Contour map of species mass fraction near outlet – cross section/top view (b) Streamlines colored by species mass fraction – front view	16
Figure 3. Nanoparticle size from TEM for a) Re = 40 b) Re = 245 c) Re = 325 and size distribution d) for image b and e) for image c	20
Figure 4. X-ray diffraction patterns of ceria nanoparticles at various synthesis conditions (a) Re = 40 (b) Re = 245 and (c) Re = 325	23
Figure 5. High resolution TEM images of ceria nanoparticles synthesized at (a) Re = 40 (b) Re = 245 and (c) Re = 325	24
Figure 6. Monte-Carlo simulation of electron interaction volume in ceria sample	27
Figure 7. Simultaneous TGA/DSC results for a)Re = 40, b)Re = 245 and c) Re = 325...	30
Figure 8. Sonochemistry in a bubble based on concept discussed by Mason et al.....	44
Figure 9. Cross-section of continuous flow reactor a) without insert and b) with insert..	48
Figure 10. Effect of volume reduction on heating rate	49
Figure 11. Schematic of continuous sonochemical reactor setup	50
Figure 12. Bubble growth dynamics in various stages during acoustic cavitation.....	52
Figure 13. Particle morphology of CdS in batch sonochemical synthesis. It can be seen from comparison between left and right images there exists at least a bimodal distribution in particle size	53
Figure 14. Particle morphology of CdS in continuous synthesis a)Transmission electron micrographs b) corresponding particle size distributions	55

LIST OF FIGURES (Continued)

<u>Figure</u>	<u>Page</u>
Figure 15. a) Change in CdS NP morphology as a function of quench delay and b) corresponding particle size distribution.....	57
Figure 16. Cross sectional TEM image showing differentiation in contrast from various layers and zoomed areas showing structure.....	59
Figure 17. Particle morphology of CdS in batch conventional heating induced synthesis60	
Figure 18. Crystal structure identification of CdS nanoparticles using x-ray diffraction [SS - Onset of steady state in continuous ultrasound heating, Bat – Batch ultrasound induced heating, BTHT – Batch conventional heating].....	61
Figure 19. Compositional homogeneity shown as atomic % ratio of Cd to S in various samples (BHT – Batch conventional heating, BAT – Batch ultrasound heating, SS – Continuous ultrasound heating at steady state).....	64
Figure 20. Schematic of the silica based ARC for (a) 1L and (b) 3L	82
Figure 21. Schematic of abrasion test rig for felt abrasion test	84
Figure 22. Performance indicators as a function of annealing time and temperature for a) 1L and b) 3L.....	86
Figure 23. Top surface scanning electron micrographs of the films a) 1L and b) 3L. Green, red, and yellow conditions are shown from top to bottom.....	91
Figure 24. Simultaneous DSC/TGA and Mass Spec analysis during annealing of single layer TMOS-NP-base gel film.....	92
Figure 25. Cross sectional transmission electron micrographs of the films a) 1L and b) 3L. Green, red, and yellow conditions are shown from left to right.....	96
Figure 26. Mechanical properties of 1L and 3L Line plot on the left shows the coating thickness.....	97
Figure 27. Crack resistance depicted as critical load for cracking under indentation and fracture toughness	98

LIST OF FIGURES (Continued)

<u>Figure</u>	<u>Page</u>
Figure 28. Scratch resistance depicted using critical loads (LC1) and delamination resistance depicted using work of adhesion.....	100
Figure 29. Spallation resistance depicted using strain energy release rate	102

LIST OF TABLES

<u>Table</u>	<u>Page</u>
Table 1. Comparison of lattice parameters for fluorite structured ceria	24
Table 2. Nanoparticle size comparison	26
Table 3. Measured atomic percentage of ceria nanoparticles for case $Re = 245$	27
Table 4. Measured atomic percentage of ceria nanoparticles for case $Re = 325$	27
Table 5. Ceria nanoparticle characteristics based on application	31
Table 6. Nanoparticle size distributions reported in the literature	45
Table 7. Experimental conditions for sonochemical synthesis of CdS	51
Table 8. Particle size statistics for CdS NPs synthesized via continuous sonochemistry.	56
Table 9. Effect of quench delay on mean particle size	57
Table 10 Descriptive terms for mechanical behavior of ARC thin films	72
Table 11. General factorial design for annealing conditions	83
Table 12. Analysis of variance on annealing parameters	87
Table 13. Regression models describing performance indicators as function of time and temperature	88
Table 14. Film coinditons selected for structural analysis.....	89

Chapter 1

1. Introduction

Microchannel mixers have specific advantages for precipitation-based nanoparticle reactions in that they accelerate the mixing of reactants compared with batch stir mixing. Typically, this is achieved through shorter diffusional distances provided by the microchannel dimensions. For typical solution-phase chemistries, diffusivities will dictate diffusional distances of tens of micrometers to approach hundred millisecond mixing times. For a precipitation chemistry, these fast mixing times can lead to rapid supersaturation and burst nucleation with smaller particle sizes, better particle size control [1] and increased throughput [2] compared with batch reactions. With fast mixing, nucleation is almost instantaneous and the residence time for the nuclei corresponds directly to the growth time.

Taking Cadmium sulfide (CdS) as an example, which is useful as photoactive and buffer layers in thin film solar cells [3] their nanoparticles (NPs) can be synthesized as quantum dots (QDs). QDs have size-related optical properties that can be used to tune the absorption and emission spectra of the material. The synthesis of CdS QDs using micromixers has recently been reported to improve process reproducibility and significantly reduce reaction time compared with batch reaction. In a particular research, mixing of reactants involved channeling the two fluid streams in a Y-shaped contactor followed by convective micromixing within a magnetic micromixer. CdS QDs of size 3 to 5.4 nm were synthesized at 220°C within capillary tubing having an inner diameter of

462 μm and a residence time of 68 sec [4]. For CdS nanoparticles to behave like quantum dots the particle size has to be less than 10 nm. It can be seen that a high degree of size control is required for QD applications and NPs in general.

One challenge with the use of micromixers for precipitation chemistries is the vulnerabilities to clogging. Some of the ways to prevent this is tuning channel dimensions, creating a two piece design for the micromixer or even by changing the reactant concentrations. Static T-mixers have been widely used in optimal mixing of fluids particularly due to their ease of availability and manufacturing [5]. The flow regimes can be varied inside a T-mixer for affecting the nanoparticle size characteristics. Hence it is important to know the flow regimes occurring inside a T-mixer at various Reynolds numbers (Re).

1.1 Mixing regimes in T-Mixers

In static microchannel T-mixers, two reactant fluids are injected into the two inlets at a constant flow rate and the fluids are mixed within an outlet channel. The flow is typically laminar with Re not generally exceeding 1000. Various mixing modes in T-mixers have been extensively studied and mapped as a function of the Reynolds number by other researchers [6-10]. Based on prior research, the mixing modes have been broadly classified into

a) Stratified flow

This occurs at Re less than 50 in which the fluid streams are stratified resulting in diffusion-controlled mixing which is relatively slow.

b) Vortex flow

As Re increased from 50 to 150 vortices begin to occur within the flow. There is a plane of symmetry observed about the axis of the T-intersection in the T-mixer. This results in reduced fluid contact and hence worse mixing

c) Engulfment flow

Engulfment flow begins to occur characterized by the fluid streams crossing over the central plane providing the best mixing conditions in this regime. In some cases the transition onset has been observed at Re slightly higher than 300 [11].

The flow transitions for a 300 μm depth T-mixer is shown in Figure 1.

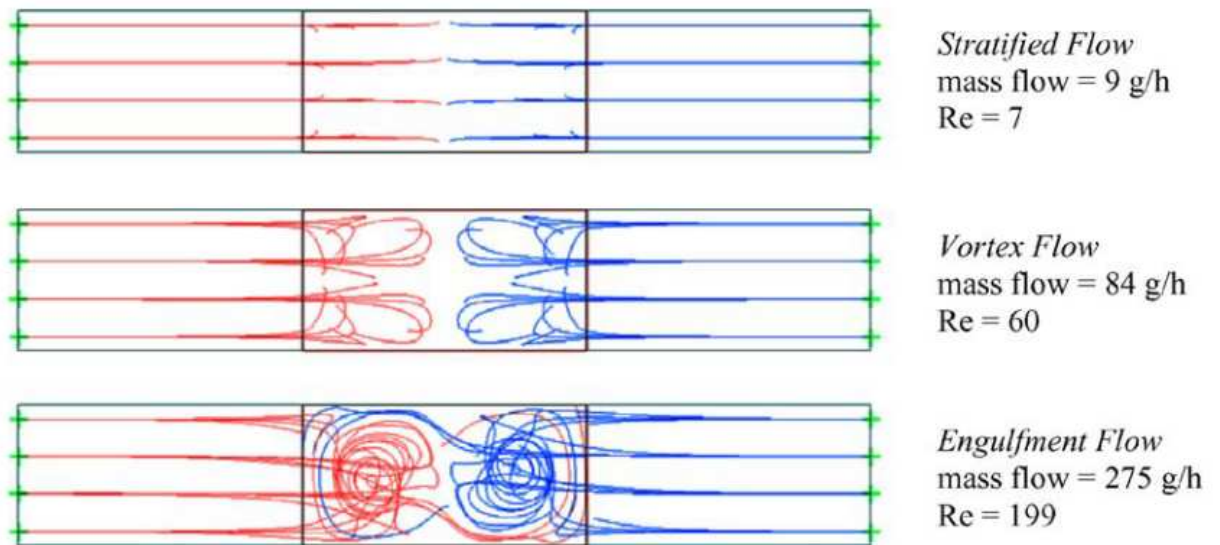


Figure 1. Flow regimes in a T-mixer [6]

2. Chapters

Chapter 1

The *objective* of this chapter is to investigate the effects of flow conditions and flow chemistry within a static microchannel T-mixer on the size, size distribution, crystallinity and agglomeration of ceria nanoparticles.

Engulfment flow in T-mixers has been reported to be a good mixing condition at Reynolds no above 250 for water [1-3]. Typical T-mixer based continuous synthesis chemistries use low flow rates with low throughputs and use flow regimes less than Re 250. At these regimes there is no mixing enhancement as the flow is still stratified and diffusion occurs only at the symmetry line where two fluid streams come in contact. These flow regimes have been already identified in T-mixers by Engler et al [4]. While engulfment flow in T-shaped microchannel mixers has been shown to provide better mixing characteristics, very little work has been reported to date on exploiting these findings for nanoparticle synthesis [5, 6]. In this work, engulfment flow – mixing condition is used to drive ceria nanoparticle synthesis and control over particle size, shape and crystallinity is exhibited using this approach.

Chapter 2

Processing becomes harder to control in batch synthesis especially when higher than room temperature reactions are involved in nanoparticle synthesis. The *objective* of this chapter is to investigate the fast heating rates provided by cavitation in a liquid subjected

to ultrasound exposure in a low volume continuous flow reactor for synthesis of cadmium sulfide nanoparticles.

Batch synthesis of cadmium sulfide for similar chemistry typically takes [7] two hours for completion. By employing an upstream mixing stage using a static T-mixer and subjecting the mixed reactants in small control volumes to high intensity ultrasound the processing time is reduced to less than a minute. Under comparison, continuous synthesis yields an average size of 22 nm with a coefficient of variation of 25% suggesting better process control. High aspect ratio nanoparticles in the shape of hexagonal platelets with uncommon cubic crystal structure for CdS were synthesized using this approach. Typically, temperatures above 800°C are used to produce high aspect ratio CdS nanoparticles and yields hexagonal crystal structure [8]. This approach appears to stabilize the metastable cubic CdS [9] which reverts to hexagonal CdS upon heating to 300°C in general [10].

Chapter 3

While exhibiting better control over nanoparticle characteristics, to use these nanoparticles in an application requires investigating the fundamental correlation between structure-properties-processing.

The *objective* of this chapter is to investigate the fundamental correlation between structure-properties-processing of silica nanoparticle based anti-reflection coatings on glass substrates.

Inspired by nature, the term Biomimetics refers to replicating applications from nature [12]. In this case moth eye-like structures that reduce reflection of light and ensure higher percentage of light entering its eye [13, 14] has caused spurious research on producing subwavelength structures that reduce reflection [15, 16]. In this work, the silica based anti-reflection coatings that are tuned towards solar cover glass applications are produced and studied. Since solar panels are exposed to elements of nature, optical performance has to be complemented by mechanical durability. Several models describe thin film failure modes due to abrasion which is a primary requirement for these coatings [17-19]. The proposal includes measurement of material properties, measuring mechanical performance against abrasion and will focus on improving mechanical properties without negatively impacting the optical performance.

3. References

- [1] Schabas, G., Yusuf, H., Moffitt, M. G., and Sinton, D., 2008, "Controlled self-assembly of quantum dots and block copolymers in a microfluidic device," *Langmuir*, 24(3), pp. 637-643.
- [2] Amador, C., Gavriilidis, A., and Angeli, P., 2004, "Flow distribution in different microreactor scale-out geometries and the effect of manufacturing tolerances and channel blockage," *Chemical Engineering Journal*, 101(1-3), pp. 379-390.
- [3] Mugdur, P. H., Chang, Y. J., Han, S. Y., Su, Y. W., Morrone, A. A., Ryu, S. O., Lee, T. J., and Chang, C. H., 2007, "A Comparison of Chemical Bath Deposition of CdS from a Batch Reactor and a Continuous-Flow Microreactor," *Journal of The Electrochemical Society*, 154(9), pp. D482-D488.
- [4] Wan, Z., Yang, H. W., Luan, W. L., Tu, S. T., and Zhou, X. G., 2010, "Facile Synthesis of Monodisperse CdS Nanocrystals via Microreaction," *Nanoscale Research Letters*, 5(1), pp. 130-137.
- [5] Kockmann, N., 2007, *Transport phenomena in micro process engineering*, Springer Verlag.
- [6] Engler, M., Kockmann, N., Kiefer, T., and Woias, P., 2004, "Numerical and experimental investigations on liquid mixing in static micromixers," *Chemical Engineering Journal (Lausanne)*, 101(1-3), pp. 315-322.
- [7] Soleymani, A., Yousefi, H., Ratchananusorn, W., and Turunen, I., 2010, "Pressure drop in micro T-mixers," *Journal of Micromechanics and Microengineering*, 20(1), p. 015029.
- [8] Wong, S., Ward, M., and Wharton, C., 2004, "Micro T-mixer as a rapid mixing micromixer," *Sensors and Actuators, B: Chemical Sensors and Materials*, 100(3), pp. 359-379.
- [9] Dreher, S., Kockmann, N., and Woias, P., 2008, "Characterization of laminar transient flow regimes and mixing in T-shaped micromixers," *Heat Transfer Engineering*, 30(1-2), pp. 91-100.
- [10] Galletti, C., Roudgar, M., Brunazzi, E., and Mauri, R., 2012, "Effect of inlet conditions on the engulfment pattern in a T-shaped micro-mixer," *Chemical Engineering Journal (Lausanne)*.
- [11] Kockmann, N., Kastner, J., and Woias, P., 2008, "Reactive particle precipitation in liquid microchannel flow," *Chemical Engineering Journal (Lausanne)*, 135, pp. S110-S116.
- [12] Bernhard, C. G., Gemne, G., and Sällström, J., 1970, "Comparative ultrastructure of corneal surface topography in insects with aspects on phylogensis and function," *Journal of Comparative Physiology A: Neuroethology, Sensory, Neural, and Behavioral Physiology*, 67(1), pp. 1-25.
- [13] Bernhard, C., Boethius, J., Gemne, G., and Struwe, G., 1970, "Eye ultrastructure, colour reception and behaviour."
- [14] Schmitt, O. H., "Some interesting and useful biomimetic transforms," *Proc. Proceeding, Third International Biophysics Congress, Boston, Mass., Aug, p. 297.*

- [15] Gombert, A., Glaubitt, W., Rose, K., Dreibholz, J., Bläsi, B., Heinzl, A., Sporn, D., Döll, W., and Wittwer, V., 1999, "Subwavelength-structured antireflective surfaces on glass," *Thin Solid Films*, 351(1–2), pp. 73-78.
- [16] Sun, C. H., Jiang, P., and Jiang, B., 2008, "Broadband moth-eye antireflection coatings on silicon," *Applied Physics Letters*, 92(6), pp. 061112-061112-061113.
- [17] Bull, S. J., 1991, "Failure modes in scratch adhesion testing," *Surface and Coatings Technology*, 50(1), pp. 25-32.
- [18] Bull, S. J., and Rickerby, D. S., 1990, "New developments in the modelling of the hardness and scratch adhesion of thin films," *Surface and Coatings Technology*, 42(2), pp. 149-164.
- [19] Blees, M. H., Winkelman, G. B., Balkenende, A. R., and den Toonder, J. M. J., 2000, "The effect of friction on scratch adhesion testing: application to a sol–gel coating on polypropylene," *Thin Solid Films*, 359(1), pp. 1-13.

**CONTINUOUS FLOW SYNTHESIS OF CERIA NANOPARTICLES
USING STATIC T-MIXERS**

B. Palanisamy and B. Paul,

Chemical Engineering Science

Vol. 78, pp. 46-52, 2012.

Chapter 2

CONTINUOUS FLOW SYNTHESIS OF CERIA NANOPARTICLES USING STATIC T-MIXERS

Abstract

Ceria nanoparticles are of interest owing to their interesting properties like photo-absorption and ability to absorb oxygen. Several batch synthesis routes exist however these methods often lack particle size control, result in agglomeration and typically require high temperature processing. In this paper, a continuous flow microchannel synthesis method based on precipitation is demonstrated with a static T-mixer, showing improved size control without agglomeration through the manipulation of flow parameters. Three flow rates were chosen representing different mixing modes and computational fluid dynamics simulations were used to visualize flow conditions. The nanoparticles were characterized for composition, size and size distribution using transmission electron microscopy, wave dispersive spectroscopy and x-ray diffraction. The engulfment flow condition, corresponding to the highest Reynolds number in this study, gave the narrowest particle size distribution (15.0 ± 4.7 nm) and best compositional uniformity.

1. Introduction

Cerium oxide (CeO_2) has been widely investigated due to its distinctive characteristics in UV absorptivity [1] and high reactivity to oxygen [2]. More recently, the size-induced property changes of ceria nanoparticles (NPs) have led to reductions in response times

within oxygen sensors [1] and decreases in sintering temperatures [2]. Cerium oxide NPs have been proposed as a substitute for silica in chemical mechanical planarization (CMP) owing to its higher hardness and better material removal characteristics [3]. Other applications for ceria NPs include radical scavenging [4], catalysis [5], sintering [6], solid oxide fuel cells [7, 8] and in sunscreens due to the UV absorbing properties [9]. Attributes of importance for these applications include narrow size distribution, shape, crystallinity and deagglomeration of nanoparticles.

Several approaches exist in the technical literature for the synthesis of ceria nanoparticles. Most batch chemistries involve a cerium salt like nitrate or chloride or acetate which is then reduced by a base like ammonium hydroxide or sodium hydroxide or amines. It has been found that pH is a critical variable for the synthesis of ceria and can affect the particle formation [10]. Depending on the solvent used (water/alcohol) and the reactant combination, the morphology of the particles has been demonstrated to vary from spheres to cubes and rods. Hydrothermal processing typically involves reacting cerium salts at high temperatures and pressures to create a gel precursor consisting of a cerium salt complex and drying precipitates in an oxygen environment [11]. Using cerium nitrate and sodium hydroxide, Mai *et al* produced ceria nanoparticles in various morphologies including spheres, cubes and rods by changing the base concentration and the hydrothermal processing temperature [12]. Microemulsion is another route that has been demonstrated for the synthesis of ceria nanoparticles. Rebellato *et al* successfully produced ceria of average size 3 nm though the particles appear to have wide size distributions and low crystallinity [8]. Electrochemical deposition has been used to yield

20 nm diameter ceria nanoparticles, however, additional heat treatment at 650 °C was used to improve the crystallinity. The process also involves tedious process control and equipment maintenance [13]. Sonochemical synthesis is yet another route characterized by long processing times (several hours) and agglomerated nanoparticles [14]. Despite the many routes for ceria synthesis, control over particle, size, crystallinity and agglomeration during synthesis remain a challenge.

For many applications, precipitation is an attractive route to ceria NP synthesis due to the cheap salt precursors, simple operation, and ease for mass production [15, 16]. However, traditional precipitation approaches in batch reactors often face long cycle times and difficulties in controlling particle size due to poor heat and mass transfer. Due to these same transport issues, batch reactors are difficult to scale to production volumes. Microchannel reactors offer accelerated heat and mass transfer which allows for rapid changes in reaction temperatures and concentrations leading to more uniform heating and mixing [17]. During nucleation, microchannel mixers offer the possibility of reducing mixing times through shorter diffusional distances and, in some cases, advective assistance. Edel et al were able to reduce the mixing time for the synthesis of CdS to the order of milliseconds by utilizing microchannels [18]. During NP growth, microchannel reactors are attributed to facilitating better control over reaction temperature and residence time [19]. Consequently, microreactors have been demonstrated to have dramatic impacts on macromolecular yields [20, 21] and nanoparticle size distributions [22-25]. The cycle time advantages of using a static microchannel T-mixer for the synthesis of ceria nanoparticles was demonstrated by Tseng et al [26]. The objective of

this paper is to investigate the effects of flow conditions and flow chemistry within a static microchannel T-mixer on the size, size distribution, crystallinity and agglomeration of ceria nanoparticles.

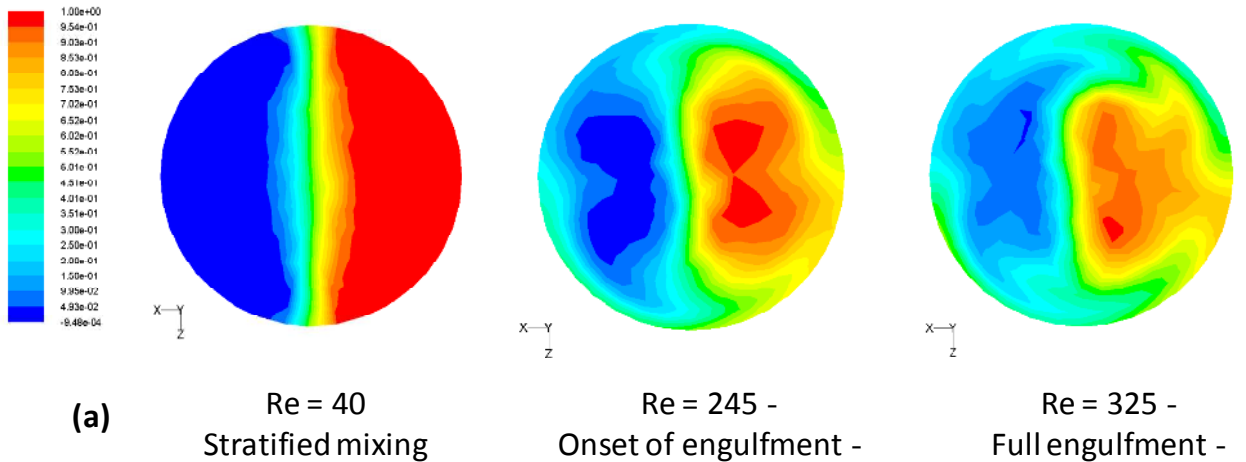
2. Methods

2.1. Flow Conditions

In static microchannel T-mixers, two reactant fluids are injected into the two inlets at a constant flow rate and the fluids are mixed within an outlet channel. The flow is typically laminar with Reynolds numbers (Re) not generally exceeding 1000. Three dominant kinds of flow have been observed [27]. At a Re of less than 50, the fluid streams are stratified resulting in diffusion-controlled mixing which is relatively slow. As Re increases, vortices begin to occur within the flow along a plane of symmetry about the axis of the outlet [28]. As the Re approaches about 240, engulfment flow begins to occur characterized by the fluid streams crossing over the central plane providing the best mixing conditions in this regime. Several researchers have validated these flow regimes using CFD simulations and experiments for microchannels with square and rectangular cross-sections [27, 29, 30]. However many off-the-shelf static T-mixers have circular cross-sections.

Numerical simulations were performed for the actual geometry of the T-mixer used in the experiments to help visualize mixing conditions within the circular mixing channel. A 3D model was created using Gambit 2.4.6 and imported into ANSYS Fluent 12.1 for solving mass and momentum conservation equations. Results were exported after convergence

and are shown in Figure 2. Figure 1a shows the cross-section of flow in the outlet near the end of the flow as shown in Figure 2b. The images in Figure 2b show the two fluids flowing through inlets from the left and right and into an outlet on the top. As shown, the mixing conditions change from a diffusion-limited, stratified flow to a diffusion-enhanced, advective flow. In the case of the lowest Re (40), it can be seen that there is no cross-over resulting only in diffusional mixing at the liquid-liquid interface. At a Re of 245, the fluid streams begin to cross-over indicating the onset of engulfment flow. At a Re of 325, it is clear that the fluid streams have intimate mixing due to engulfment flow. These Re are similar to those reported in the literature for the onset of engulfment flow [27, 29, 30].



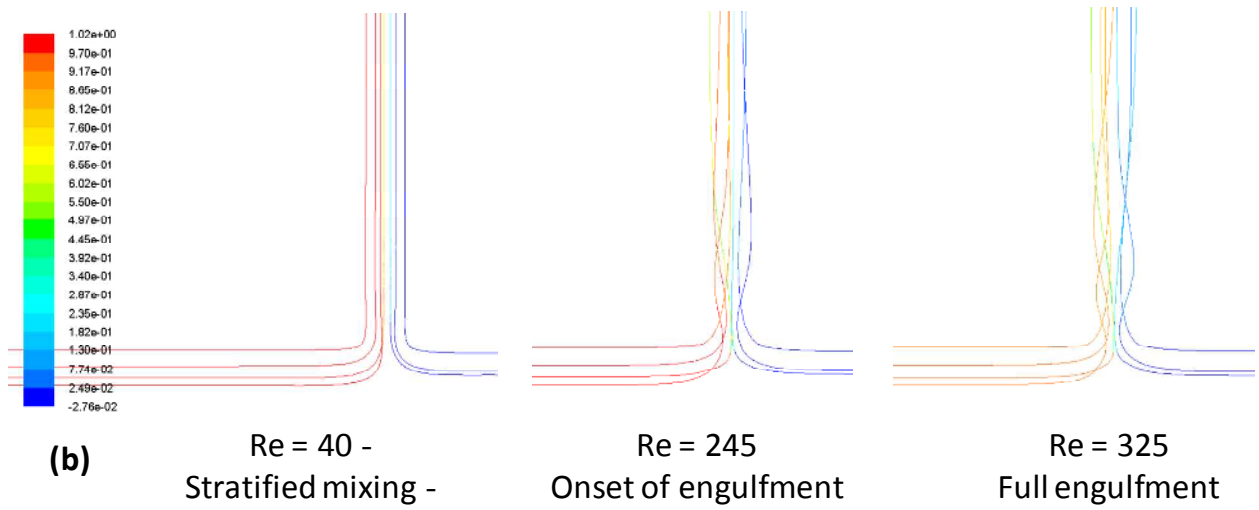


Figure 2. Flow transition in static T-mixer observed in CFD numerical simulation
(a) Contour map of species mass fraction near outlet – cross section/top view (b)
Streamlines colored by species mass fraction – front view

While engulfment flow in T-shaped microchannel mixers has been shown to provide better mixing characteristics [27-30], very little work has been reported to date on exploiting these findings for nanoparticle synthesis [31, 32]. Further, prior research with static T-mixers studying the effect of engulfment flow on particle size did not investigate the effects of engulfment on agglomeration or crystallinity [31]. Other researchers have evaluated the effect of mixing conditions beyond engulfment at Re up to 8000 in the outlet of microchannel T-mixers [33-36]. While researchers have shown that increasing Re over 1000 can reduce the average particle size and the size dispersion, this has been achieved at very high fluid velocities [33, 34]. For instance, 60 nm BaSO₄ NPs were produced at a very high throughput of 300 ml/min with an average velocity of 6.4 m/s based on calculations [36]. At these high fluid velocities, slurry erosion of the channel walls becomes a concern especially during the synthesis of oxide nanoparticles which are generally very hard. Liu et al showed that significant erosion can arise in an oxide-

reinforced metal (Ni) matrix composite at fluid velocities as low as 3 m/s [37]. In this study, the three flow conditions shown in Figure 1 were used to evaluate the effect of engulfment on ceria NP size, size distribution, crystallinity and agglomeration.

2.2. Flow Chemistry

Within precipitation reactions, particle size is affected by the nucleus size at nucleation which is in turn controlled by the supersaturation of reactants. For a precipitation reaction, particle nucleation occurs when the concentration of reactants become supersaturated. The effect of supersaturation on critical nuclei size has been explained by Mullin [38] for precipitation reactions and can be summarized in the following equation:

$$S = \frac{[Ce^{3+}][OH^{-}]^3}{K_{sp}} \quad (1)$$

where S is the supersaturation and K_{sp} is the solubility product and

$$r^* = \frac{2v\gamma}{kT \ln(S)} \quad (2)$$

where r^* is the critical nuclei size, k is the Boltzmann constant, γ is the interfacial energy and v is the molecular volume for the compound. Based on Equation 2, it can be observed that higher supersaturation values can result in smaller nuclei and, therefore, smaller particles. In this paper, reactant concentrations of 0.09M were calculated to yield a nucleus diameter of 5 nm.

Prior batch precipitation chemistries have involved the reaction of cerium nitrate and ammonium hydroxide dissolved in a water-alcohol solvent. The pH of this reaction was

not allowed to go beyond 8 and progressed at room temperature. Following synthesis, the particles were calcined at temperatures 500, 600, 700 and 800 °C and an associated improvement in crystallinity was observed [39]. The room temperature reaction of cerium nitrate and triethanolamine (TEA) in ethanol over 40 minutes has yielded ceria nanoparticles with nearly spherical morphology and a size distribution of 5.9 ± 0.5 nm. An intermediate Ce (IV)-TEA complex was found to promote the oxidation of Ce^{3+} to Ce^{4+} [40].

As a result, the flow chemistry proposed below was chosen to increase the rate of nucleation by increasing the rate of pH change. NaOH is proposed here as a stronger base for precipitation. Also, TEA is used to aid the conversion of cerium salt to its oxide and it has also been reported to act as a surfactant for deagglomeration [41].

3. Experimental procedure

In this research, computational fluid dynamics (CFD) simulations were performed to identify the best mixing conditions and also to understand the fluid flow transitions occurring in flow in a microchannel T-mixer with a circular cross-section. Three flow rates (2.3, 15, 20 ml/min) were chosen representing the flow conditions shown in Figure 2. A Tygon® tube of inner diameter 1.22 mm and length 50 mm was added to the outlet of the T-mixer. Overall, based on flow rates and the mixer setup, average residence times for the three mixing conditions were calculated to be 1.6, 0.25 and 0.18 sec, respectively. A 500 µm diameter static T-mixer (Idex Corp, USA) was used for the nanoparticle synthesis. Reagent solutions of 0.09M $\text{Ce}(\text{NO}_3)_3 \cdot 6\text{H}_2\text{O}$ and 0.09M NaOH were prepared

using 2-propanol as a solvent. To further aid in the reaction and to act as a surfactant, 0.5M of TEA was added to the mixed solution. The reaction was quenched and the as-synthesized nanoparticles were collected after centrifuging at 12000 rpm and washed repeatedly before examination. A Harvard Apparatus PHD2000 Syringe pump (Holliston, MA, USA) was used to pump the reagents through the T-mixer at varying flow rates. All the experiments were performed within a controlled environment at 22°C.

A Phillips CM-12 TEM operating at 120 kV and a FEI TITAN TEM (Portland, OR, USA) operating at 300 kV were used to image the nanoparticles. A Bruker-AXS D8 Discover X-ray diffraction unit (Madison, WI, USA) was used for phase analysis using XRD patterns. A SX-100 CAMECA Electron microprobe analyzer (Gennevillier, France) was used to evaluate the composition of nanoparticles using wave dispersive spectroscopy. Simultaneous thermogravimetric analysis and differential scanning calorimetry were performed using a TA Instruments Q600 (New Castle, DE, USA) to study the thermally induced phase changes.

4. Results and discussion

Experiments were carried out by fixing the concentrations of the reactant while the flow rates were varied to realize the three different Reynolds numbers.

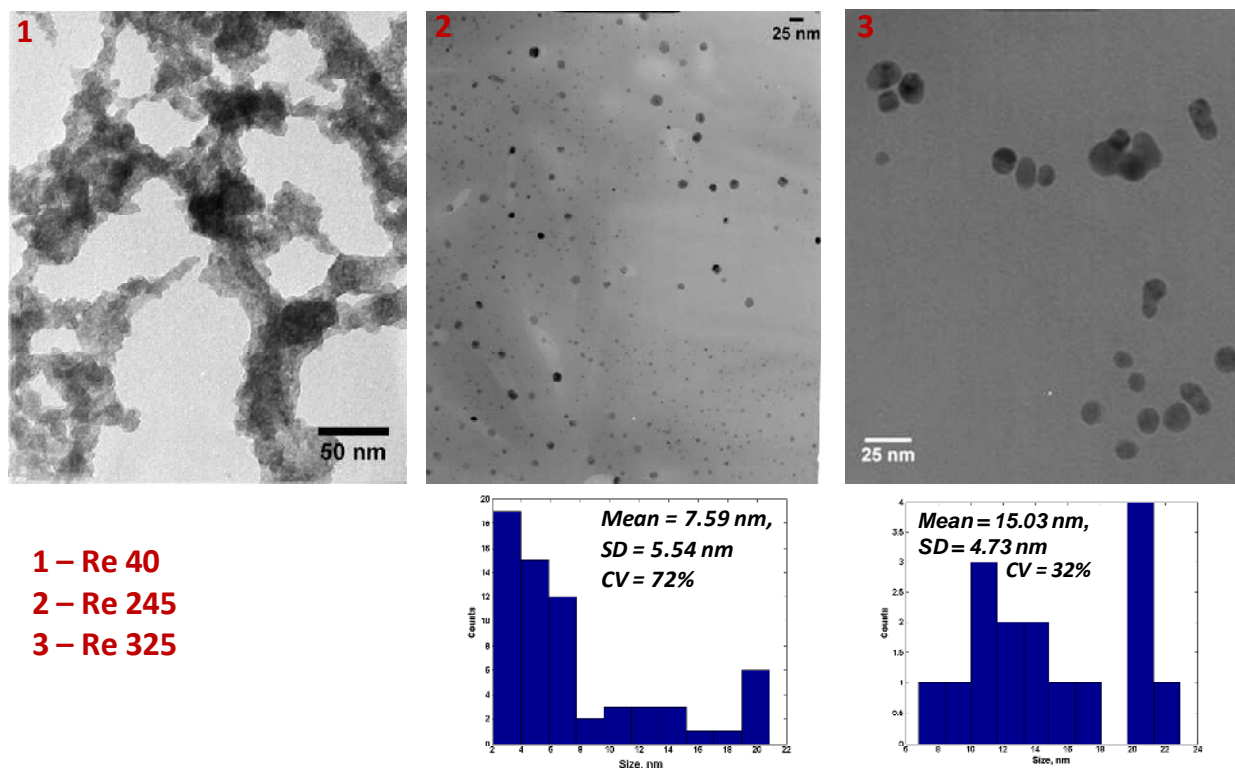


Figure 3. Nanoparticle size from TEM for a) Re = 40 b) Re = 245 c) Re = 325 and size distribution d) for image b and e) for image c

Figure 3 shows the corresponding experimental results after ceria nanoparticle synthesis. At a Re of 40, it can be observed that there is extensive agglomeration yielding structures with features approaching a micrometer in scale. At a Re of 245 at the onset of engulfment, interestingly the nanoparticles no longer appear agglomerated. The shape was found to be spherical with a wide coefficient of variance for particle size. At a Re of 325, it was observed that the particle size distribution is narrower and the shape remains unchanged with increasing Re. In addition, the average particle size was found to be larger owing to better mixing leading to higher supersaturation and higher growth rates in

a diffusion controlled regime. This would also explain the marked absence of a population of smaller particles i.e. the distribution is skewed to the right unlike the case where $Re = 245$

X-ray diffraction patterns for the nanoparticles are shown in Figure 4. In Figure 4a, the presence of cerium hydroxide peaks in the diffraction pattern suggests that the reaction is incomplete. With increasing Re , the occurrence of these peaks is reduced. Based on integral area under the peaks for $Ce(OH)_3$ which is indirectly affected by the wt% of this phase, a 40% reduction in occurrence of $Ce(OH)_3$ for $Re = 245$ (3b) and a 75% reduction for $Re = 325$ (3c) is observed. This indicates completion of the reaction at higher Re even though the residence time for condition (b) is $1/6^{th}$ that for condition (a) and the residence time for condition (c) is $1/8^{th}$ that for condition (a). This further supports the notion of enhanced mixing at higher Re . As Re increases, the additional peaks of ceria (311) and (400) appear due to the additional conversion of reactants and $Ce(OH)_3$ to CeO_2 . This higher conversion is apparent by simply measuring the dry weight of obtained precipitates. The weights of the obtained precipitate for Re values of 40, 245 and 325 were 0.7 mg, 5.5 mg and 6.3 mg respectively. The XRD data was deconvoluted to separate the crystalline and amorphous phase contributions. Based on the intensities of the peaks the following formula was used to calculate the percentage crystallinity as outlined by He [42].

$$\text{Percentage crystallinity } X_C = \frac{I_c}{I_c + I_A} \times 100 \quad (3)$$

Where I_C is intensity of the crystalline phase and I_A is the intensity of the amorphous phase. Based on this equation the values of X_C for Re 40, 245, 325 were found to be 26.5%, 27.3% and 37.7% respectively.

This suggests improved stoichiometry and crystallinity with increasing Re due to better mixing conditions. It is expected that the better mixing conditions led to a better stoichiometric distribution of reactants and hence higher crystallinity. In all cases, cerium hydroxide peaks were observed as an intermediate compound. It is well known that subsequent exposure to oxygen can convert the remaining hydroxide into oxide. Also observed were some unidentified peaks which were prominent in lower Re. These peaks could be possibly attributed to $[\text{Ce}(\text{TEA})_2(\text{NO}_3)](\text{NO}_3)_2$ complex as mentioned by Pati et al during synthesis of ceria using TEA [41].

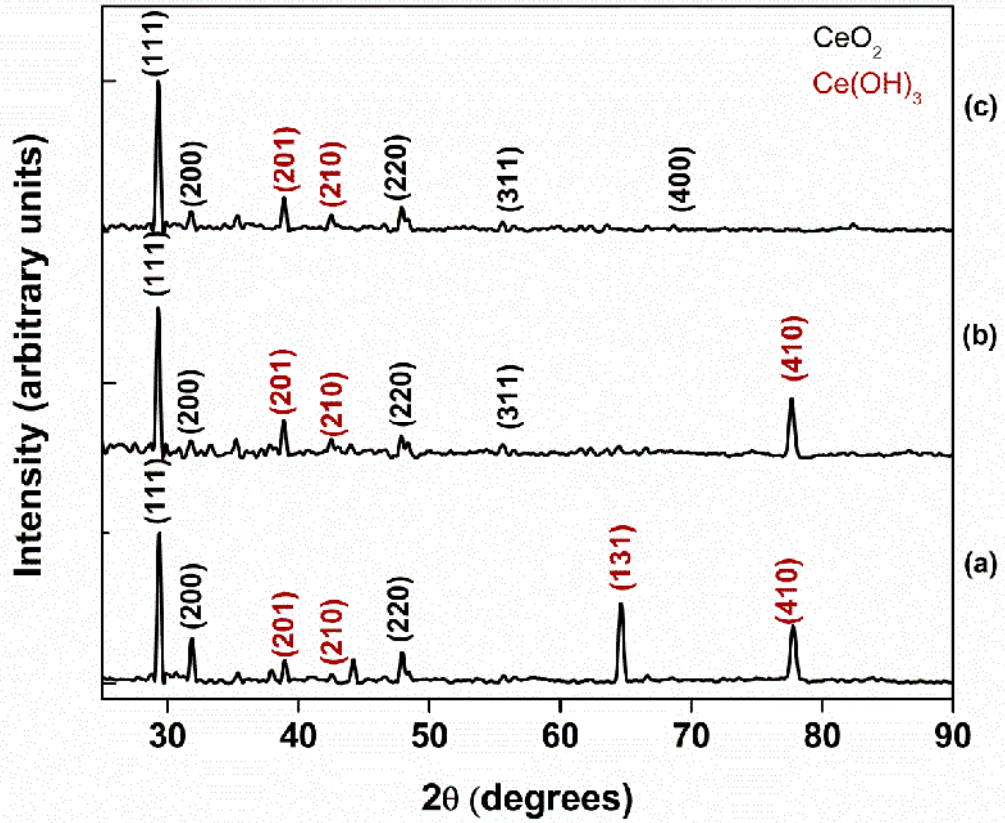


Figure 4. X-ray diffraction patterns of ceria nanoparticles at various synthesis conditions (a) $Re = 40$ (b) $Re = 245$ and (c) $Re = 325$

High resolution TEM micrographs of the synthesized nanoparticles corresponding to the various flow conditions are shown in Figure 5. Planar spacings are detectable in these images and some representative regions are highlighted in the images. Planar spacings were also determined using XRD results in conjunction with the ICDD PDF-2 database. The lattice parameter was calculated using the formula:

$$a_0 = d \sqrt{h^2 + k^2 + l^2} \quad (4)$$

where d is the interplanar spacing and (hkl) are the Miller indices from the identified planes. The measured planar spacings based on the micrographs were compared with XRD results and the comparison is shown in Table 1.

Table 1. Comparison of lattice parameters for fluorite structured ceria

Re	Identified planes	D-spacing		Lattice parameter	
		from XRD	from HRTEM	from XRD	from HRTEM
40	(111)	0.312	0.315	0.540	0.546
	(200)	0.271	0.270	0.542	0.540
240	(111)	0.312	0.310	0.540	0.537
	(200)	0.271	0.280	0.542	0.560
325	(111)	0.312	0.315	0.540	0.546
	(200)	0.271	0.270	0.542	0.540

¹Data compared from XRD standard reference data from ICDD PDF-2 database

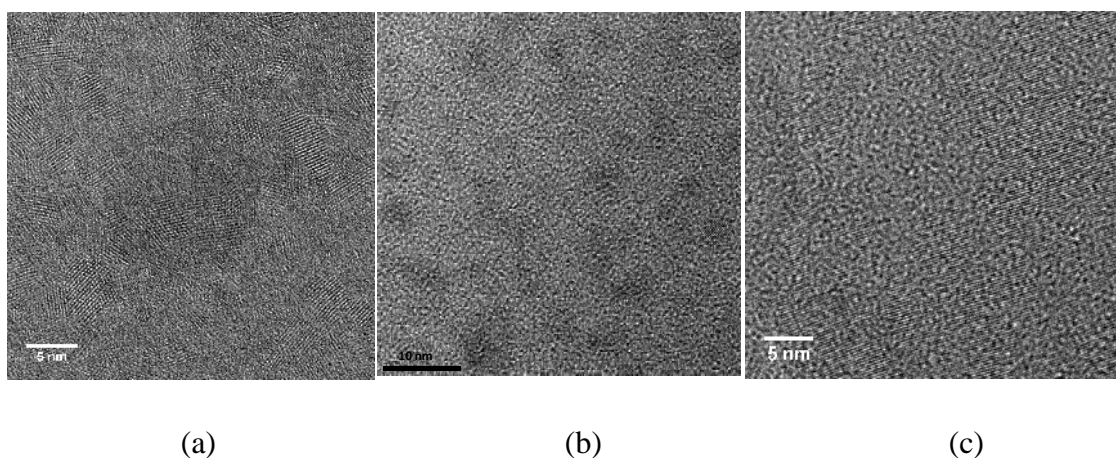


Figure 5. High resolution TEM images of ceria nanoparticles synthesized at (a) Re = 40 (b) Re = 245 and (c) Re = 325

It can be observed that the lattice parameters values are consistent between XRD and TEM for both the lowest and highest Re. At a Re of 245, the lattice parameter is found to

be slightly higher compared to the equilibrium value of 0.541 nm for (200) plane. This difference can be attributed to a change in valency of cerium ion from +4 to +3 and to the small particle size. This behavior of size related change in valency has been first reported by Tsunekawa et al [43]. This finding would be confirmed in subsequent work.

The mean particle sizes were calculated based on TEM and XRD data and is summarized in Table 2. Since the high resolution TEM images indicate that the particles are single crystalline, crystallite size calculated from the full width and half maxima (FWHM) of the ceria peaks would give the particle size. Also it is assumed that the contribution to peak broadening from strain in the nanoparticles is negligible. The Debye-Scherrer equation [44] is used to calculate the particle size sing FWHM and is given by

$$B(2\theta) = \frac{K\lambda}{L\cos\theta} \quad (5)$$

Where B is the peak broadening from crystallites of size < 100 nm, K is the scherrer constant and is taken as 0.9 [45], λ is the wavelength of the x-ray beam and 2θ is the scattering angle.

Table 2. Nanoparticle size comparison

Re	Particle size (Mean \pm SD) nm	
	from XRD	from TEM
40	20.7 ± 3.5	-
240	9.6 ± 1.5	7.59 ± 5.54
325	14.7 ± 6.4	15.03 ± 4.73

Electron microprobe analysis using WDS was carried out to identify the composition of the precipitated nanoparticles and thereby confirm their stoichiometry. This was carried out for nanoparticles synthesized at Re of 245 and 325. The sample pertaining to Re 40 could not be satisfactorily characterized in WDS owing to the presence of the TEA complex leading to an increase in complexity of measurement. Several milligrams of the nanoparticles were synthesized and used to form a loosely bound film on glass substrate. The thickness, and hence the amount of nanoparticles, were adjusted to remove substrate effects during WDS probing. This is based on the interaction volume of the incident electron beam on the sample [46]. As shown in Figure 6, the interaction volume for the ceria sample was estimated using CASINO Monte Carlo simulation developed by Drouin et al [47]. It can be seen there is an interaction volume of approximately $1 \mu\text{m}^3$ at 20 keV incident energy. Hence it is expected that the composition information is collected from thousands of nanoparticles for each data point. The corresponding results for the compositional analysis are summarized in Table 3 and Table 4 respectively.

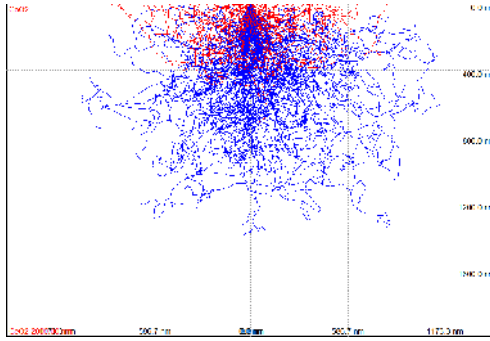


Figure 6. Monte-Carlo simulation of electron interaction volume in ceria sample

Table 3. Measured atomic percentage of ceria nanoparticles for case Re = 245

Point	Ce	O	O:Ce
1	29.98	70.02	2.34
2	29.37	70.63	2.41
3	31.67	68.33	2.16
4	35.34	64.66	1.83
5	33.13	66.87	2.02
		Average	2.15

Table 4. Measured atomic percentage of ceria nanoparticles for case Re = 325

Point	Ce	O	O:Ce
1	31.66	68.34	2.16
2	38.19	61.81	1.62
3	28.87	71.13	2.46
4	38.22	61.78	1.62
5	32.34	67.66	2.09
		Average	1.99

On observing the stoichiometric ratio of oxygen to cerium, the higher flow rate shows an average stoichiometric ratio closer to the theoretical ratio of 2. This supplements earlier findings suggesting that better mixing leads to better nanoparticle stoichiometry. Also since the ratio is very close to 2, the contribution of cerium hydroxide to the stoichiometric ratio seems to be low suggesting that the volumetric percentage of cerium hydroxide in the sample is low. This is also consistent with the XRD results.

Simultaneous thermo gravimetric analysis and differential scanning calorimetry were performed on the samples to carry out extensive thermal analysis. The results are shown in Figure 7. Comparing all the DSC results it can be observed that there is an exothermic peak in the 290°C – 320°C range. This can be attributed to conversion of $\text{Ce}(\text{OH})_3$ to Ce_2O_3 . This reaction is exothermic since it takes 1392 KJ/mol to break the three O-H bonds to form one Ce-O bond requiring 795 KJ/mol [48]. The weight loss is significant in all three samples around the same temperature consistent with loss of 3 moles of water formed for every 2 moles of cerium hydroxide. The possible reaction is



The start of amorphous to crystalline transformation can be observed for all samples around 600°C based on the DSC results. The heat flow required decreases with increasing Re again reinforcing the findings from XRD where higher Re implies higher crystallinity. An endothermic dip is also observed for these samples centered around 1000°C for (b) and 930°C for (c). This could be possibly be attributed to sintering of the nanoparticles. The peak at 900°C for (a) could result from the loss of carbon from the

cerium-TEA complex. Again at 1185°C an endothermic peak suggests possible transition of CeO_2 to Ce_2O_3 under inert atmosphere through loss of oxygen for (a) and (c). A similar transition has been reported by Zhou et al at 1200°C [49]. The corresponding weight loss is observed to initiate at 1100°C for both (a) and (c). This transition is not clearly observed for (b) and it is possible that the transition overlaps with the huge endothermic dip associated with sintering.

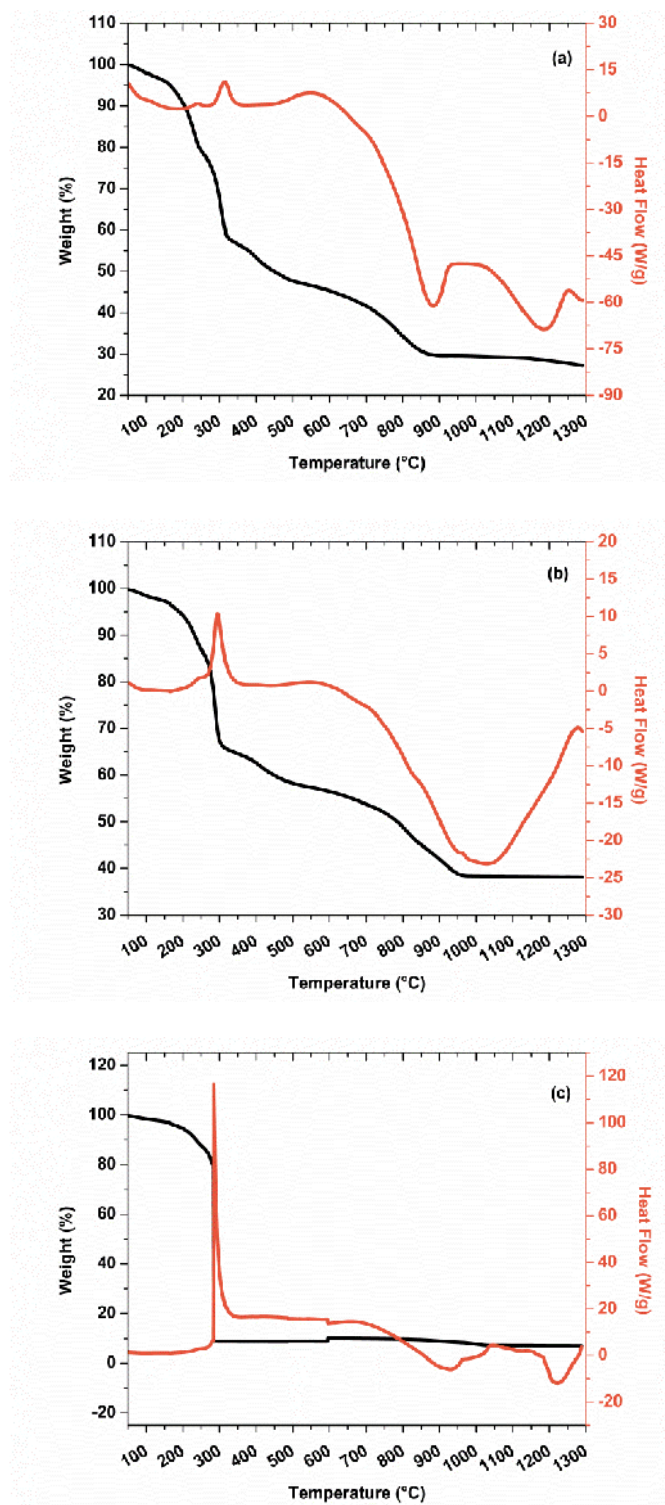


Figure 7. Simultaneous TGA/DSC results for a) $Re = 40$, b) $Re = 245$ and c) $Re = 325$

A summary of the particle sizes and shapes used for various applications of ceria NPs is shown in Table 5. This table suggests that nanoparticles synthesized in this paper could be useful as a sintering aid or in chemical mechanical planarization.

Table 5. Ceria nanoparticle characteristics based on application

Ref	Application	Typical size (nm)	Desired shape
[3, 50, 51]	Chemical Mechanical Planarization	5 - 100	Rounded, spherical
[4, 52]	Radical Scavenger	3 - 5	Faceted
[8, 12]	Fuel Cell	5 - 40	Cubical
[53, 54]	Catalyst	10 - 30	Octahedral
[55, 56]	Sintering aid	10 - 50	Spherical

5. Conclusions

In this research, a new synthesis route for ceria nanoparticle precipitation was demonstrated using engulfment flow conditions within a microchannel static T-mixer. NaOH was used to increase the rate of pH change, TEA was used to assist in the conversion of Ce^{+3} to Ce^{+4} and to help control agglomeration and IPA was used to provide better control over agglomeration. Several conclusions were drawn as a result of this research. First, using the chemistry and setup outlined in this paper, the flow regime used for nanoparticle synthesis, as dictated by the Re, was found to affect the attributes of the nanoparticles synthesized. Specifically, results show that the better mixing conditions due to flow engulfment with the static T-mixer lead to better stoichiometry and better crystallinity as well as better utilization of the reactants. Further, the average particle size

was found to be larger under full engulfment flow (15.0 ± 4.7 nm) suggesting that better mixing may also lead to faster nucleation and growth in cerium oxide. Also, the ceria nanoparticle shape was found to be spherical and rounded under engulfment flow which is well-suited for applications in sintering and chemical mechanical planarization. Finally, despite the possibility that the enhanced advection under engulfment flow conditions could lead to greater agglomeration, nanoparticles produced under engulfment flow were found to be well dispersed with no agglomeration.

6. Acknowledgements

This material is based upon work supported by the National Science Foundation under Grant No. 0654434. The authors would like to acknowledge the support of instrumentation equipment within the Microproducts Breakthrough Institute, Corvallis, USA by the Murdock Charitable Trust (2010004). The authors would also like to thank Dr. Tom Tseng, alumni of our research group, for his prior work which provided insight into the direction of the current research. The authors would also like to thank Daniel Peterson, PhD student and Anna Garrison, Faculty Research Associate both at Oregon State University for their guidance and insightful discussions on the CFD results.

7. References

- [1] Izu, N., Shin, W., Murayama, N., and Kanzaki, S., 2002, "Resistive oxygen gas sensors based on CeO₂ fine powder prepared using mist pyrolysis," *Sens. Actuators, B*, 87(1), pp. 95-98.
- [2] Chen, P.-L., and Chen, I. W., 1993, "Reactive Cerium(IV) Oxide Powders by the Homogeneous Precipitation Method," *J. Am. Ceram. Soc.*, 76(6), pp. 1577-1583.
- [3] Yang, J. C., Kim, H.-j., and Kim, T., 2010, "Study of Polishing Characteristics of Monodisperse Ceria Abrasive in Chemical Mechanical Planarization," *J. Electrochem. Soc.*, 157(3), p. H235.
- [4] Karakoti, A. S., Singh, S., Kumar, A., Malinska, M., Kuchibhatla, S. V. N. T., Wozniak, K., Self, W. T., and Seal, S., 2009, "PEGylated Nanoceria as Radical Scavenger with Tunable Redox Chemistry," *J. Am. Chem. Soc.*, 131(40), pp. 14144-14145.
- [5] Yan, B., and Zhu, H., 2008, "Controlled synthesis of CeO₂ nanoparticles using novel amphiphilic cerium complex precursors," *J. Nanopart. Res.*, 10(8), pp. 1279-1285.
- [6] Quinelato, A., 2000, "Effect of ceria content on the sintering of ZrO₂ based ceramics synthesized from a polymeric precursor," *J. Eur. Ceram. Soc.*, 20(8), pp. 1077-1084.
- [7] Kumar, A., Babu, S., Karakoti, A. S., Schulte, A., and Seal, S., 2009, "Luminescence Properties of Europium-Doped Cerium Oxide Nanoparticles: Role of Vacancy and Oxidation States," *Langmuir*, 25(18), pp. 10998-11007.
- [8] Rebellato, J., Natile, M. M., and Glisenti, A., 2008, "Influence of the synthesis procedure on the properties and reactivity of nanostructured ceria powders," *Appl. Catal., A*, 339(2), pp. 108-120.
- [9] Yabe, S., and Sato, T., 2003, "Cerium oxide for sunscreen cosmetics," *J. Solid State Chem.*, 171(1-2), pp. 7-11.
- [10] Chen, J.-C., Chen, W.-C., Tien, Y.-C., and Shih, C.-J., 2010, "Effect of calcination temperature on the crystallite growth of cerium oxide nano-powders prepared by the co-precipitation process," *J. Alloys Compd.*, 496(1-2), pp. 364-369.

- [11] Phoka, S., Laokul, P., Swatsitang, E., Promarak, V., Seraphin, S., and Maensiri, S., 2009, "Synthesis, structural and optical properties of CeO₂ nanoparticles synthesized by a simple polyvinyl pyrrolidone (PVP) solution route," *Mater. Chem. Phys.*, 115(1), pp. 423-428.
- [12] Mai, H.-X., Sun, L.-D., Zhang, Y.-W., Si, R., Feng, W., Zhang, H.-P., Liu, H.-C., and Yan, C.-H., 2005, "Shape-Selective Synthesis and Oxygen Storage Behavior of Ceria Nanopolyhedra, Nanorods, and Nanocubes," *J. Phys. Chem. B*, 109(51), pp. 24380-24385.
- [13] Wang, T., and Sun, D., 2008, "Preparation and characterization of nanometer-scale powders ceria by electrochemical deposition method," *Mater. Res. Bull.*, 43(7), pp. 1754-1760.
- [14] Yin, L., Wang, Y., Pang, G., Koltypin, Y., and Gedanken, A., 2002, "Sonochemical Synthesis of Cerium Oxide Nanoparticles--Effect of Additives and Quantum Size Effect," *J. Colloid Interface Sci.*, 246(1), pp. 78-84.
- [15] Drobot, D., Chub, A., Voronov, V., Fedorov, P., Ivanov, V., and Polezhaeva, O., 2008, "Preparation of ceria nanoparticles," *Inorg. Mater.*, 44(8), pp. 853-855.
- [16] Zhou, X. D., Huebner, W., and Anderson, H. U., 2002, "Room-temperature homogeneous nucleation synthesis and thermal stability of nanometer single crystal CeO₂," *Appl. Phys. Lett.*, 80(20), p. 3814.
- [17] Schwarzer, H. C., and Peukert, W., 2004, "Tailoring particle size through nanoparticle precipitation," *Chem. Eng. Commun.*, 191(4), pp. 580-606.
- [18] Edel, J. B., Fortt, R., deMello, J. C., and deMello, A. J., 2002, "Microfluidic routes to the controlled production of nanoparticles," *Chem. Commun. (Cambridge, U. K.)*(10), pp. 1136-1137.
- [19] Chang, C. H., Paul, B. K., Remcho, V. T., Atre, S., and Hutchison, J. E., 2008, "Synthesis and post-processing of nanomaterials using microreaction technology," *J. Nanopart. Res.*, 10(6), pp. 965-980.
- [20] Joanicot, M., and Ajdari, A., 2005, "Droplet control for microfluidics," *Science*, 309(5736), p. 887.

- [21] Chang, C. H., Liu, S. H., Tennico, Y., Rundel, J. T., Remcho, V. T., Blackwell, E., Tseng, C. H., and Paul, B. K., "Progress Towards Chip-Based High-Throughput Dendrimer Synthesis," Proc. International Conference on Microreaction Technology, pp. 3011-3018.
- [22] Nakamura, H., Yamaguchi, Y., Miyazaki, M., Maeda, H., Uehara, M., and Mulvaney, P., 2002, "Preparation of CdSe nanocrystals in a micro-flow-reactor," Chem. Commun.(23), pp. 2844-2845.
- [23] Chan, E. M., Mathies, R. A., and Alivisatos, A. P., 2003, "Size-controlled growth of CdSe nanocrystals in microfluidic reactors," Nano Lett., 3(2), pp. 199-201.
- [24] Yen, B. K. H., Stott, N. E., Jensen, K. F., and Bawendi, M. G., 2003, "A continuous-flow microcapillary reactor for the preparation of a size series of CdSe nanocrystals," Adv. Mater. (Weinheim, Ger.), 15(21), pp. 1858-1862.
- [25] Krishnadasan, S., Tovilla, J., and Vilar, R., 2004, "On-line analysis of CdSe nanoparticle formation in a continuous flow chip-based microreactor," J. Mater. Chem., 14(17), pp. 2655-2660.
- [26] Tseng, C., and Paul, B., 2007, "Comparison of batch mixing and micromixing approaches in the synthesis and deposition of ceria nanoparticles," Transactions of NAMRI, 35.
- [27] Engler, M., Kockmann, N., Kiefer, T., and Woias, P., 2004, "Numerical and experimental investigations on liquid mixing in static micromixers," Chem. Eng. J., 101(1-3), pp. 315-322.
- [28] Kockmann, N., 2007, Transport phenomena in micro process engineering, Springer Verlag.
- [29] Wong, S., Ward, M., and Wharton, C., 2004, "Micro T-mixer as a rapid mixing micromixer," Sens. Actuators, B, 100(3), pp. 359-379.
- [30] Soleymani, A., Yousefi, H., Ratchananusorn, W., and Turunen, I., 2010, "Pressure drop in micro T-mixers," J. Micromech. Microeng., 20(1), p. 015029.
- [31] Kockmann, N., Kastner, J., and Woias, P., 2008, "Reactive particle precipitation in liquid microchannel flow," Chem. Eng. J., 135, pp. S110-S116.

- [32] Grundemann, L., Fischer, N., and Scholl, S., 2009, "From Macro Batch to Micro conti Manufacturing: A New Eco Friendly Production Process for Writing Ink Employing Micro process Engineering," *Chem. Eng. Technol.*, 32(11), pp. 1748-1756.
- [33] Schwarzer, H. C., and Peukert, W., 2004, "Combined experimental/numerical study on the precipitation of nanoparticles," *AIChE J.*, 50(12), pp. 3234-3247.
- [34] Azouani, R., Michau, A., Hassouni, K., Chhor, K., Bocquet, J. F., Vignes, J. L., and Kanaev, A., 2010, "Elaboration of pure and doped TiO₂ nanoparticles in sol-gel reactor with turbulent micromixing: Application to nanocoatings and photocatalysis," *Chem. Eng. Res. Des.*, 88(9), pp. 1123-1130.
- [35] Telib, H., Manhart, M., and Iollo, A., 2004, "Analysis and low-order modeling of the inhomogeneous transitional flow inside a T-mixer," *Phys. Fluids*, 16, p. 2717.
- [36] Schwarzer, H. C., and Peukert, W., 2002, "Experimental investigation into the influence of mixing on nanoparticle precipitation," *Chem. Eng. Technol.*, 25(6), pp. 657-661.
- [37] Liu, L., and Xu, J., 2011, "A study of the erosion–corrosion behavior of nano-Cr₂O₃ particles reinforced Ni-based composite alloying layer in aqueous slurry environment," *Vacuum*, 85(6), pp. 687-700.
- [38] Mullin, J. W., 2001, *Crystallization*, Butterworth-Heinemann.
- [39] Li, M., Zhang, R., Zhang, H., Feng, W., and Liu, X., 2010, "Synthesis, structural and magnetic properties of CeO₂ nanoparticles," *Micro & Nano Letters*, 5(2), p. 95.
- [40] Liu, K., and Zhong, M., 2010, "Synthesis of monodispersed nanosized CeO₂ by hydrolysis of the cerium complex precursor," *J. Rare Earth.*, 28(5), pp. 680-683.
- [41] Pati, R. K., Lee, I. C., Gaskell, K. J., and Ehrman, S. H., 2008, "Precipitation of Nanocrystalline CeO₂ Using Triethanolamine," *Langmuir*, 25(1), pp. 67-70.
- [42] He, B. B., 2011, *Two-dimensional X-Ray Diffraction*, John Wiley & Sons.
- [43] Tsunekawa, S., Ishikawa, K., Li, Z. Q., Kawazoe, Y., and Kasuya, A., 2000, "Origin of Anomalous Lattice Expansion in Oxide Nanoparticles," *Phys. Rev. Lett.*, 85(16), p. 3440.

- [44] Scherrer, P., 1918, "Bestimmung der Grösse und der inneren Struktur von Kolloidteilchen mittels Röntgenstrahlen," *Nachr. Ges. Wiss. Göttingen*, 26, pp. 98-100.
- [45] Langford, J. I., and Wilson, A., 1978, "Scherrer after sixty years: a survey and some new results in the determination of crystallite size," *J. Appl. Crystallogr.*, 11(2), pp. 102-113.
- [46] Williams, D. B., and Carter, C. B., 2009, "The Transmission Electron Microscope," *Transmission Electron Microscopy*, pp. 3-22.
- [47] Drouin, D., Couture, A. R., Joly, D., Tastet, X., Aimez, V., and Gauvin, R., 2007, "CASINO V2. 42—A Fast and Easy-to-use Modeling Tool for Scanning Electron Microscopy and Microanalysis Users," *Scanning*, 29(3), pp. 92-101.
- [48] Wilcox, D., and Bromley, L., 1963, "Computer estimation of heat and free energy of formation for simple inorganic compounds," *Industrial & Engineering Chemistry*, 55(7), pp. 32-39.
- [49] Zhou, Y., and Rahaman, M., 1993, "Hydrothermal synthesis and sintering of ultrafine CeO₂ powders," *J. Mater. Res.*, 8(07), pp. 1680-1686.
- [50] Zhang, Z., Liu, W., Zhu, J., and Song, Z., 2010, "Synthesis, characterization of ceria-coated silica particles and their chemical mechanical polishing performance on glass substrate," *Appl. Surf. Sci.*, 257(5), pp. 1750-1755.
- [51] Armini, S., Burtovyy, R., Moinpour, M., Luzinov, I., Messemacker, J. D., Whelan, C. M., and Maex, K., 2008, "Interaction Forces Between a Glass Surface and Ceria-Modified PMMA-Based Abrasives for CMP Measured by Colloidal Probe AFM," *J. Electrochem. Soc.*, 155(4), pp. H218-H223.
- [52] Kar, S., Patel, C., and Santra, S., 2009, "Direct Room Temperature Synthesis of Valence State Engineered Ultra-Small Ceria Nanoparticles: Investigation on the Role of Ethylenediamine as a Capping Agent," *The Journal of Physical Chemistry C*, 113(12), pp. 4862-4867.
- [53] Tan, J. P. Y., Tan, H. R., Boothroyd, C., Foo, Y. L., He, C. B., and Lin, M., 2011, "Three-Dimensional Structure of CeO₂ Nanocrystals," *The Journal of Physical Chemistry C*, 115(9), pp. 3544-3551.

- [54] Laosiripojana, N., and Assabumrungrat, S., 2011, "Conversion of poisonous methanethiol to hydrogen-rich gas by chemisorption/reforming over nano-scale CeO_2 : The use of CeO_2 as catalyst coating material," *Applied Catalysis B: Environmental*, 102(1-2), pp. 267-275.
- [55] Yang, Y., Wang, Y., Wang, Z., Liu, G., and Tian, W., 2008, "Preparation and sintering behaviour of nanostructured alumina/titania composite powders modified with nano-dopants," *Materials Science and Engineering: A*, 490(1-2), pp. 457-464.
- [56] Muroi, M., Trotter, G., McCormick, P. G., Kawahara, M., and Tokita, M., 2008, "Preparation of nano-grained zirconia ceramics by low-temperature, low-pressure spark plasma sintering," *J. Mater. Sci.*, 43(19), pp. 6376-6384.

**CONTINUOUS SONOCHEMICAL SYNTHESIS OF CADMIUM
SULFIDE NANOPATELETS USING AN AZEOTROPIC SOLVENT**

B. Palanisamy, C. Chang and B. Paul,

Ultrasonics and Sonochemistry

Submitted

Chapter 3

CONTINUOUS SONOCHEMICAL SYNTHESIS OF CADMIUM SULFIDE NANOPATELETS USING AN AZEOTROPIC SOLVENT

Abstract

Cadmium sulfide (CdS) nanoparticles (NPs) exhibit quantum confinement effects as they approach the Bohr exciton radius below 10 nm. CdS is widely used as a buffer material in thin film solar cells owing to its broad band transmission of solar light. Sonochemical synthesis permits the rapid heating of reactant baths by acoustic cavitation leading to high local temperatures. In this research, three heating modes are used for the synthesis of CdS NPs ranging from batch conventional heating to batch ultrasound-induced (USI) heating and continuous USI heating. Continuous sonochemical synthesis was found to result in high aspect ratio hexagonal platelets of CdS possessing cubic crystal structures with thicknesses substantially below 10 nm. The unique shape and crystal structure of the NPs are suggestive of a high temperature phase produced using liquid-phase chemistry. NP size uniformity, compositional uniformity, material utilization and product throughput are equivalent or significantly better for the continuous sonochemical process in comparison to the other processes.

1. Introduction

Ultrasound energy is used by industry in a variety of ways including among others for cleaning, non-destructive materials testing, the welding of plastics and metals, and more recently sonochemistry [1]. Useful ultrasound frequencies extend from the high

frequencies in the range of 2-10 MHz used in diagnostics to the low frequencies in the range of 20 – 100 kHz used in sonochemical applications [2]. In sonochemical synthesis, low-frequency sound waves are emitted from a horn and propagated through the solution in which the horn is submerged. The low-frequency ultrasound energy couples with the solvent producing fluid dynamic, thermal and chemical effects [3].

Ultrasonic energy is coupled with solvents via cavitation involving bubble nucleation, growth and collapse [4]. During the rarefaction half cycle the bubble grows and reaches a critical size before it implodes in a compression half cycle [3, 5]. This implosion has been estimated to increase the local temperature of the surrounding liquid to over 5000°C and increase the local pressure to nearly 1000 atm [6, 7]. Such effects have been observed experimentally [8]. The bubble collapse event lasts for less than a nanosecond and causes extremely high cooling rates in the order of 10^{11} K/s. These high cooling rates provide a means to rapidly quench reactions.

The instantaneous temperature rise upon collapse of a bubble due to adiabatic implosion is given by

$$T_{\max} = T_0 \left[\frac{P_{ex}(\gamma - 1)}{P_{bub}} \right] \quad (6)$$

where T_{\max} is the temperature reached after the collapse of the bubble, T_0 is the temperature of the bath, gamma is the adiabatic index, P_{ex} is the external pressure = hydrostatic + acoustic pressure and P_{bub} is the pressure of the gas inside the cavity at the

point of collapse. In turn, the maximum pressure inside the bubble at the moment of implosion is given by [9]

$$P_{\max} = P_{\text{bub}} \left[\frac{P_{\text{ex}} (\gamma - 1)}{P_{\text{bub}}} \right]^{\frac{\gamma}{\gamma - 1}} \quad (7)$$

The occurrence of cavitation is dictated by the Blake threshold which is defined as the minimum acoustic power required to cause cavitation in a liquid [10]. The onset of cavitation can be influenced by changing the temperature of the fluid or the amount of dissolved gas within the fluid both which change the Blake threshold. Some of the extrinsic variables that affect the sonochemical reactivity are discussed below [2].

In sonochemistry, as bubbles are formed, the reaction proceeds from the bubble interior to the bubble wall, comprising a vapor-liquid interface, to the surrounding liquid. These regions are shown in the schematic in Figure 8 below. For a reactant mixture, the bubble interior consists of solvent and solute vapors. If a non-volatile solvent is used, the presence of solute vapors can be achieved inside the bubble thus maintaining the reaction within the bubble [11]. Vapors continue to diffuse into the bubble during the growth phase of the bubble from the adjacent liquid.

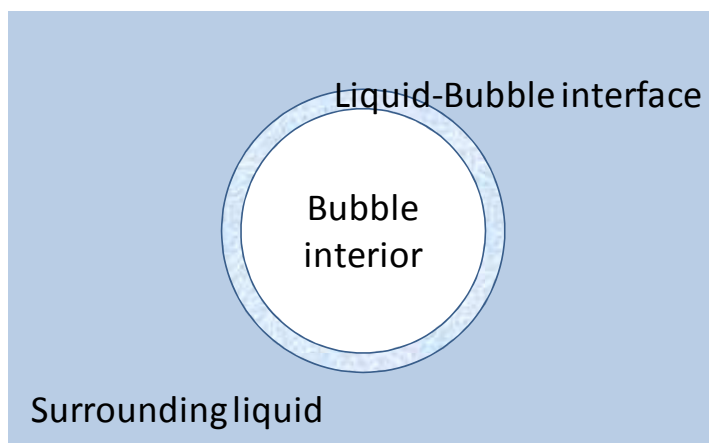


Figure 8. Sonochemistry in a bubble based on concept discussed by Mason et al [1]

Frequency [12]

It has been observed that changing frequency between 10 Hz to 10 MHz does not cause significant effect on cavitation since this only alters the resonant size of the cavitation bubble and is negligible over this range. It is important to note that 10X more power is required to cavitate water at 400 kHz than at 10 kHz. This is primarily because power losses increase due to the increased rate of molecular motion at higher frequencies. This is an important reason for the use of a 20 kHz frequency for many sonochemical applications.

Power [13]

Power input to the horn can change the amount of liquid undergoing cavitation and hence can affect reaction rate. There is a limit to the power input to the liquid as increasing bubble nucleation can eventually prevent the liquid from contacting the horn, disrupting power transfer.

Bulk temperature [13-15]

Since bulk temperature affects the vapor pressure of the solvent, the nucleation rate of bubbles can be increased with increasing temperature until the increase in vapor pressure begins to influence the reactivity of the system.

For nanoparticle chemistries, particles have been found to nucleate within bubbles [16] in a process called sonocrystallization [17]. It has been found that the particle size distribution for nanoparticles is narrower for sonocrystallization than for other comparable synthesis methods such as microfluidic-based routes. Table 6 shows a corresponding comparison of coefficient of variation (COV) based on data reported for these nanoparticle synthesis routes.

Table 6. Nanoparticle size distributions reported in the literature

Material	Avg Size (nm)	SD (nm)	COV (%)	Synthesis Approach	Author
Pd	3.6	0.7	19.4	Sonochem	Fujimoto et al [18]
Au/Pd	8.0	1.1	13.8	Sonochem	Mizukoshi et al [19]
CdSe	8.0	0.6	8.0	Sonochem	Mastai et al [11]
CdSe	3.0	0.6	19.7	Sonochem	Mastai et al [11]
CdSe	4.0	0.7	17.0	Sonochem	Mastai et al [11]
CdSe	5.5	0.6	10.2	Sonochem	Mastai et al [11]
Fe ₃ O ₄	9.8	3.5	35.9	Ultrasound assisted	Siddiqui et al [20]
Fe ₃ O ₄	12.4	5.3	42.7	Ultrasound assisted	Siddiqui et al [20]
Au	2.9	0.6	20.7	Microfluidic reactor	Shalom et al [21]
Au	34.0	7.8	23.0	Microfluidic reactor	Sugano et al [22]
CdS	4.5	1.0	22.2	Microfluidic reactor	Peterson et al [23]

Fe_3O_4	5.2	2.0	38.5	Microfluidic reactor	Salazar-Alvarez et al [24]
Zeolite	140.0	46.5	33.2	Microfluidic reactor	Pan et al [25]

In the sonochemical synthesis route, heating by cavitation and bubble implosion provides a potential route to high temperature reactions from a liquid phase. Sonochemistry has been used for the synthesis of nanoparticles of various semiconductor materials like CdS [26, 27] and PbS [28, 29] in batch modes. It has been demonstrated that a surfactant free approach using sonochemistry can be used to generate well dispersed CdS NPs [26]. However in batch mode, long residence times measured in hours can make process control more difficult due to the chemistry being exposed to the US energy multiple times. Further, batch US chemistries are difficult to scale-up. In continuous sonochemical synthesis, residence times can be reduced from several hours to less than a minute making it easier to control reaction conditions. Also, conventional solution processing does not yield high aspect ratio particles or high temperature phases. In general, very little research has been performed on continuous sonochemical synthesis [30, 31].

In this paper, the high local temperatures of acoustic cavitation are used to continuously produce a metastable crystal structure in the form of high aspect ratio platelets of CdS. The sub 10 nm thick platelets exhibit good particle size control without the use of surfactants. The method is compared with batch sonochemistry and conventional heating to delineate the advantages.

2. Development of a continuous flow sonochemical reactor

A flow cell reactor was developed to couple an ultrasonic (US) horn with the nanoparticle chemistry of interest. Ultrasound attenuates as a function of distance in front of the horn. Attenuation is an exponential function, strongly dependent on the attenuation coefficient (α) as given by [1]

$$I = I_0 \exp(-2\alpha d) \quad (8)$$

where I is intensity at distance d from the source, I_0 being initial intensity. The acoustic pressure amplitude as a function of distance from the horn has been modeled using the equation [32]

$$P(d) = \rho c v \left| 2 \sin \left(\frac{\pi}{\lambda} \left(\sqrt{d^2 + a^2} - d \right) \right) \right| \quad (9)$$

where $P(d)$ is the acoustic pressure amplitude as a function of distance d , ρ is the density of the liquid, c is velocity of sound in the liquid, v is the velocity amplitude of the horn, λ is the wavelength of the sound and a is the radius of the horn tip.

A key factor in the design of the flow cell was to reduce the residence time of the flow chemistry within the reactor. Shorter residence times would lead to the potential for higher, more uniform power densities adjacent to the horn and less exposure to bulk temperatures. A horn with a maximum power inverter rating of 750 W (model VCX 750) and an interfacing flow cell (630-0495) were acquired from Sonics and Materials, Inc. To reduce fluid residence time within the flow cell, the internal volume of flow cell was

modified through the use of an insert (Figure 9). The flow cell insert reduced the flow cell volume from 65 ml to 8 ml.

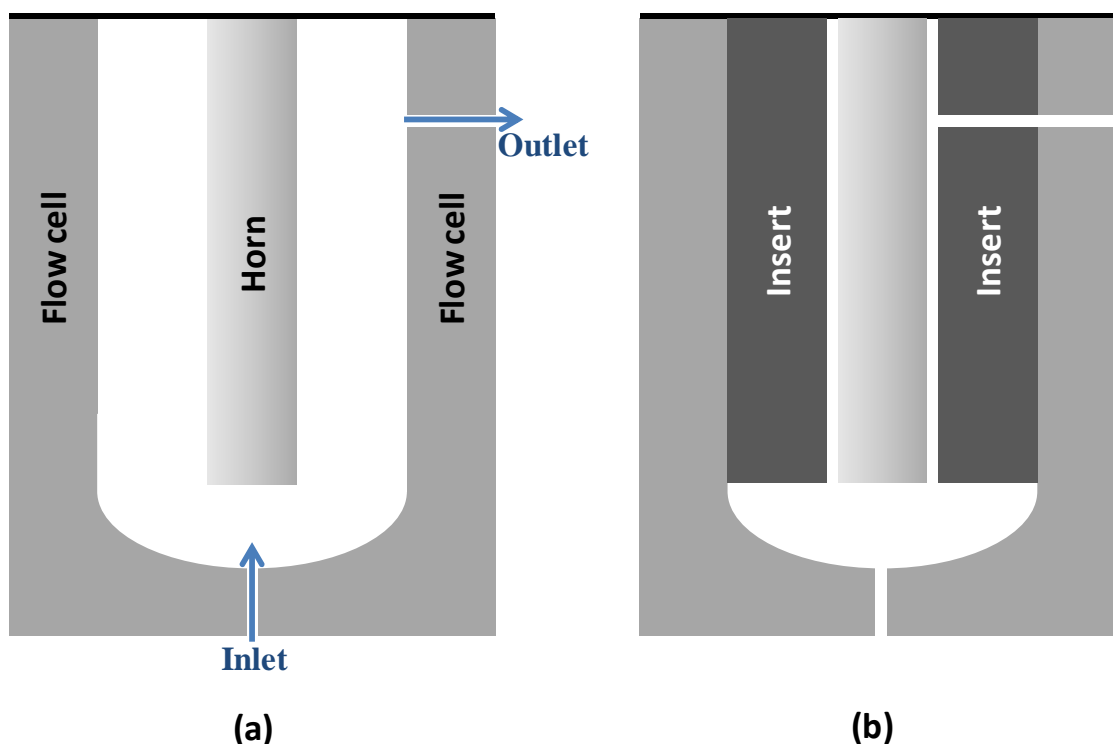


Figure 9. Cross-section of continuous flow reactor a) without insert and b) with insert

Figure 9 shows a schematic of the internal volume of the reactor with and without the flow insert. The critical dimension in the insert was the clearance between the horn outer diameter and the inner diameter of the insert itself. This had to be sufficiently larger than the critical bubble size in order to prevent vapor lock restricting the outflow of processed reactants. The flow insert was made of UHMWPE due to its low density, high elasticity, high softening point and low cost.

The use of the insert was found to provide several benefits. First, Figure 10 shows the effect of the flow cell insert on the time needed for the bulk temperature to reach steady state in pure water. It can be clearly observed that it takes approximately one-third the amount of time to reach 70°C for pure water. Second, the curve collected without the insert shows several points at which the temperature suddenly drops off. This is due to temperature accumulation adjacent to the horn leading to bubble accumulation and disruption of power transfer. This suggests that the use of the flow cell insert led to better temperature uniformity within the flow cell as originally intended. A schematic of the final continuous flow setup is shown in Figure 11.

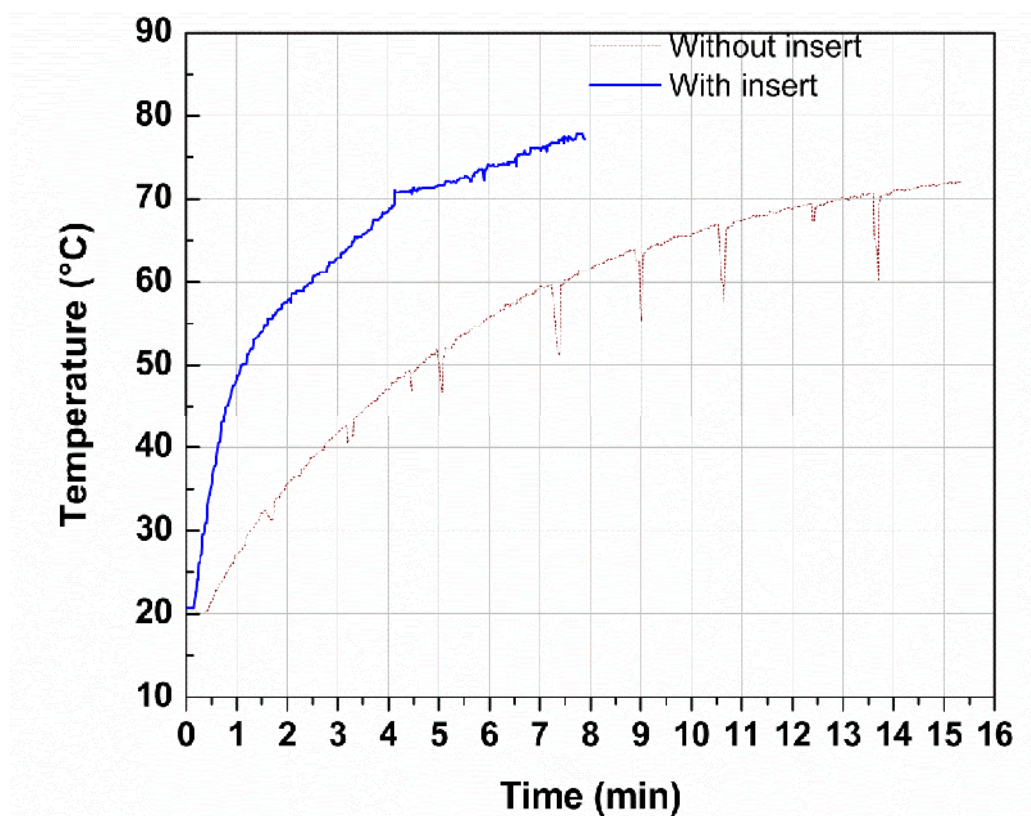


Figure 10. Effect of volume reduction on heating rate

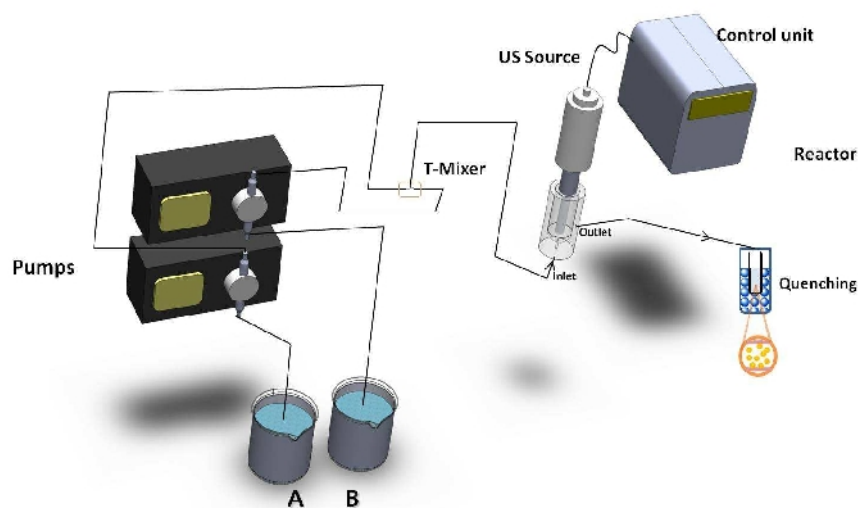


Figure 11. Schematic of continuous sonochemical reactor setup

3. Experimental methods

Based on prior literature [33], a cadmium chloride and thiourea reactant chemistry was chosen for sonochemical synthesis of cadmium sulfide nanoparticles. This chemistry involves processing at 85°C [34, 35]. The reaction mechanism involves forming a cadmium-thiourea complex – $\text{Cd}[\text{SC}(\text{NH}_2)_2](\text{OH})_2$ which is aided by ammonia released from ammonium chloride-ammonium hydroxide buffer. This controls the release of Cd ions for precipitation into CdS and hence affects the kinetics of the reaction, aimed at controlling the particle size. Table 7 shows the conditions chosen for the reaction in batch and continuous modes. The chemistry was first evaluated in batch mode to check feasibility.

Table 7. Experimental conditions for sonochemical synthesis of CdS

Parameters	Batch	Continuous
Chemistry	$\text{CdCl}_2 + \text{CS}(\text{NH}_2)_2 + \text{NH}_4\text{Cl} + \text{NH}_4\text{OH}$	$\text{CdCl}_2 + \text{CS}(\text{NH}_2)_2 + \text{NH}_4\text{Cl} + \text{NH}_4\text{OH}$
Processing time	120 min	48 sec
Reynolds no	-	410
Ultrasound Power (Avg)	20 W	100 W

Since the boiling point of pure water is very close to the reaction temperature of 85°C, and also it is known that highly localized hot spots result in vapor phase formation which caused flow disruption due to vapor locks. Hence an azeotropic mix consisting of water and ethylene glycol in a 1:1 volume was used which elevated the boiling point to 107°C [36]. The nanoparticles were quenched at the outlet, washed, dried and used for observation. A FEI TITAN Chemi-STEM (Portland, OR, USA) operating at 200 kV was used to image the nanoparticles. A Bruker-AXS D8 Discover X-ray diffraction unit (Madison, WI, USA) was used for phase analysis using XRD patterns. A SX-100 CAMECA Electron microprobe analyzer (Gennevillier, France) was used to evaluate the composition of nanoparticles using wave dispersive spectroscopy.

3.1. Bubble dynamics

Bubble nucleation, growth and cavitation are the primary phenomena occurring within the continuous reactor. In order to reduce the internal volume of the reactor the critical dimension has to be significantly larger than the critical bubble size at cavitation. This

ensures constant outflow without pressure buildup within the reactor. To evaluate this, a high speed camera (Phantom Miro, Wayne, NJ, USA) was used to capture the stages in bubble cavitation directly below the high intensity ultrasound horn. The images were captured at 60,000 frames per second to capture a phenomenon occurring based on the input of 20 kHz ultrasonic energy. Figure 12 shows the high speed images and the various stages can be observed. The bubble diameter during the growth phase was found to be less than 150 μm .

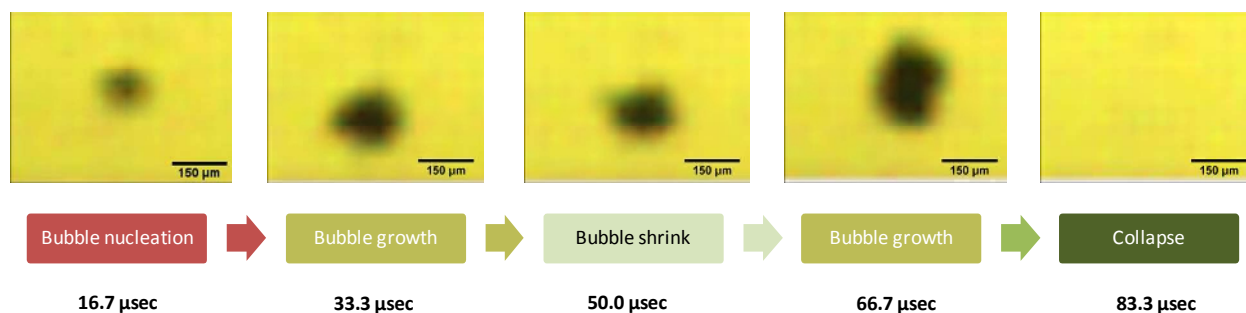


Figure 12. Bubble growth dynamics in various stages during acoustic cavitation

3. Results and discussion

Experiments were carried out by fixing the concentrations of the reactant in batch mode with constant amplitude while in continuous mode flow rate was fixed at 10 ml/min net flow rate. Figure 13 summarizes the TEM results obtained on the nanoparticles during batch synthesis at a) 1 hr and b) 2 hr. At 1 hr a mixture of very small amorphous particles ordering less than 10 nm along with large chunks of nanoparticles ordering 250 nm are also observed. The small particles correspond to freshly formed nuclei which is apparent from their amorphous nature as observed from the weak contrast from the TEM images. At 2 hrs, we can see a wide distribution of irregular shaped particles. This shows higher

conversion of the reactants owing to the presence of higher fraction of particles. It is also apparent that the particle size distribution is wide ranging from 50 nm to 200 nm suggesting poor process control.

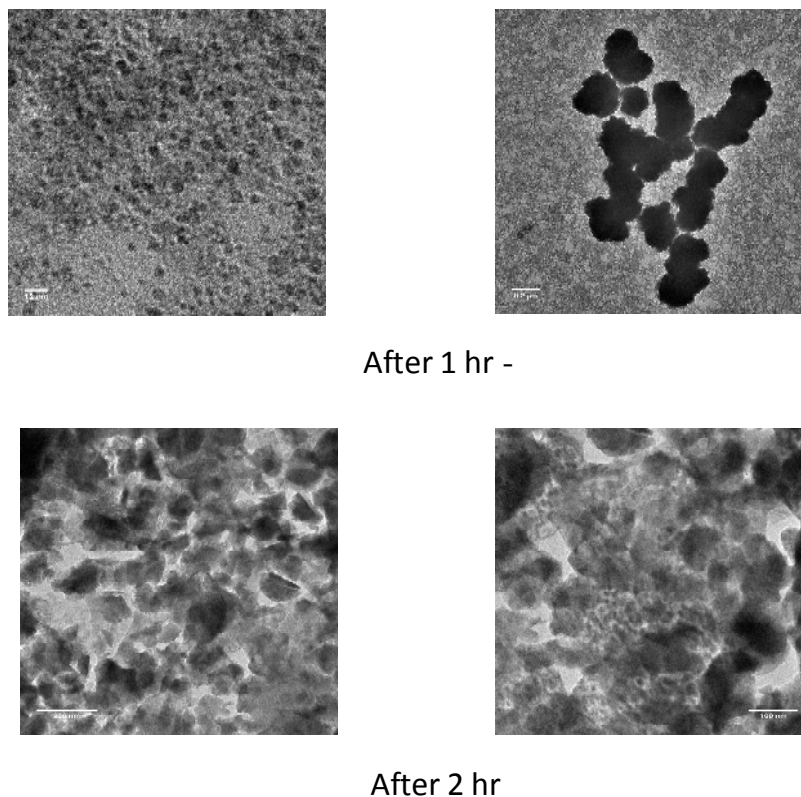
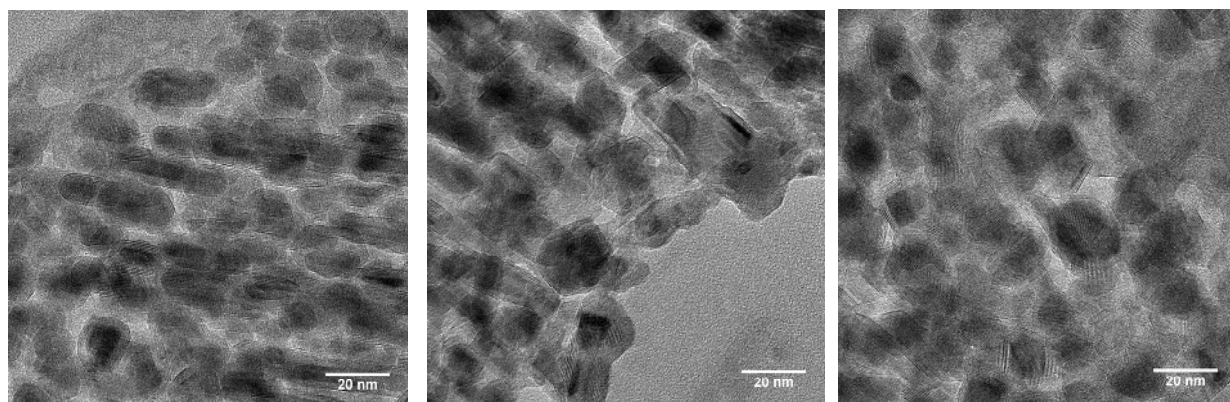


Figure 13. Particle morphology of CdS in batch sonochemical synthesis. It can be seen from comparison between left and right images there exists at least a bimodal distribution in particle size

Within the flow cell, the mixed reactants are subjected to ultrasound exposure. At a fluid residence time of 48 seconds, with exposure to ultrasound at an average power of 100 W, the same chemistry was run through the flow cell. The fluid temperature inside the flow cell rose at a rate of $\sim 50^{\circ}\text{C}/\text{min}$. When the fluid reached a reaction temperature of 85°C ,

the outflow was found to be pale yellow in color which is characteristic of a suspension containing cadmium sulfide. The cadmium sulfide nanoparticles were collected and quenched in a vial to stop the reaction and then imaged using the TEM. The corresponding images are shown in Figure 14a. It is apparent the predominant morphology of samples collected at various points in steady state (SS) – after onset, 3 minutes into SS and 6 minutes into SS is hexagonal platelets. Since the particles are electron thin and contrast from overlying particles are observed in the micrographs, the particles are expected to be thin platelets. Figure 14b shows the particle size distribution of the corresponding images. The distributions are nearly normal with a predominant skewing to the left that shifts the mean. The corresponding mean particle sizes are listed in Table 8. As shown, the average sizes of the particles are very close with similar standard deviations. A Tukey multiple comparison test shows there is no significant difference between the particle size distribution at 3 and 6 minutes. The coefficient of variation (COV) at 3 and 6 minute shows good process control with COVs similar to those previously reported.

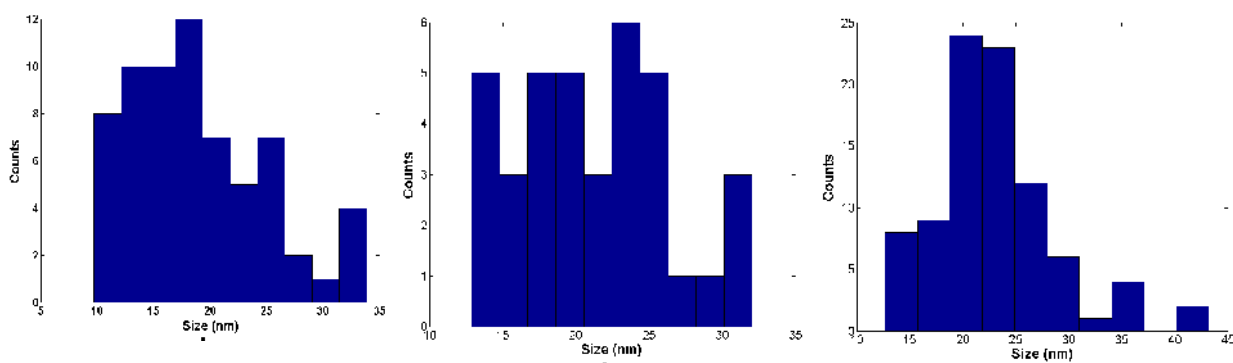


Onset of Steady state (SS)

SS + 3 min

SS + 6 min

(a)



Onset of Steady state (SS)

SS + 3 min

SS + 6 min

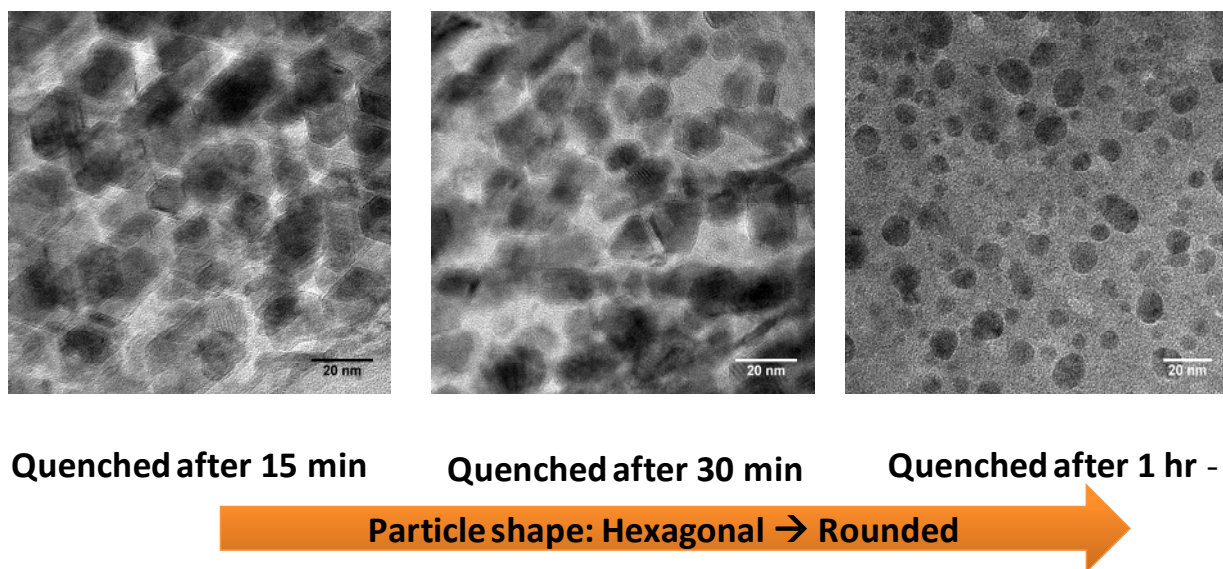
(b)

Figure 14. Particle morphology of CdS in continuous synthesis a) Transmission electron micrographs b) corresponding particle size distributions

Table 8. Particle size statistics for CdS NPs synthesized via continuous sonochemistry

	SS	SS + 3 min	SS + 6 min
Avg size (nm)	19.3	21.3	22.9
SD (nm)	6.2	5.2	5.8
COV %	32.6%	24.3%	25.2%

In another experiment, samples collected at steady state were quenched at various delays to check the progress of the reaction with time after the particles leave the sonochemical reactor. Figure 15 shows the particle morphology and distribution as a function of quench delay time.



(a)

Figure 15

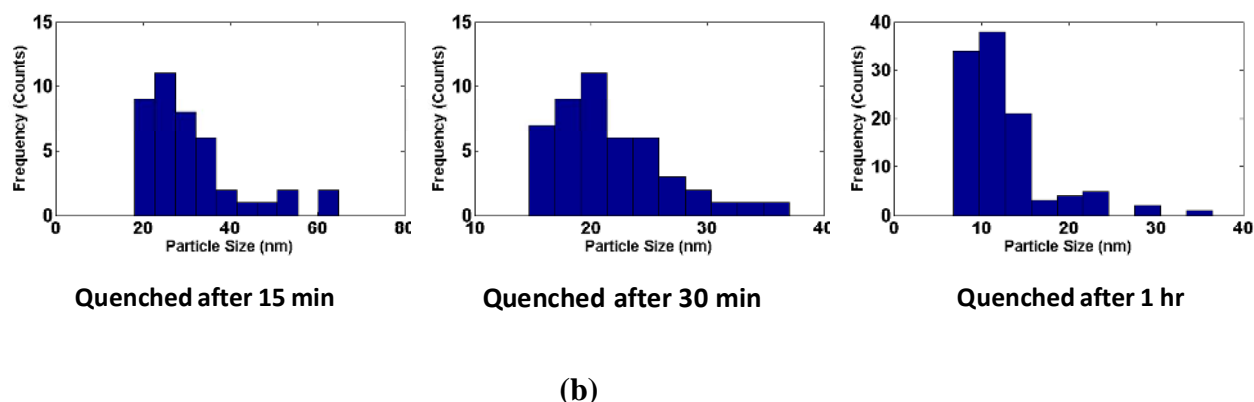


Figure 15. a) Change in CdS NP morphology as a function of quench delay and b) corresponding particle size distribution

An interesting morphological evolution occurs upon observing the TEM images. NPs quenched after 15 minutes from collection still retain hexagonal platelet shape while at 30 minutes the particle edges appear to get rounded or smooth. The faceted appearance starts to disappear and is completely absent when quenching is delayed by 1 hour where the particles appear to be well rounded or nearly spherical. It is also interesting to note that the shape of the particle size distribution in figure 7b does not change with quench delay suggesting that the distribution follows the same trend with time. The corresponding mean sizes are listed in Table 9.

Table 9. Effect of quench delay on mean particle size

Quench delay	15 min	30 min	60 min
Avg size (nm)	31.7	21.7	12.5
SD (nm)	11.1	4.9	5.1
COV %	35.2	22.7	40.8

From Table 9, it is apparent that the NP average size is decreasing with quench delay time. This suggests that another particle growth mechanism is active instead of the classical Ostwald ripening. One reason that the average size is decreasing is because the particle morphology changes from a high aspect ratio platelet to a spherical particle. Since volume has to be conserved, the average particle size decreases. This rearrangement of particle shape and size could occur by surface diffusion of Cd and S ions around the particles. To evaluate the thickness of the nanoparticle platelets the product sampled after 6 minutes from steady state were used to form a thin film on a silicon substrate. On the as coated sample a carbon coating is deposited for contrast and a chromium layer is deposited for protecting the top surface of the film from the focused ion beam used to section the sample. A thin section of approximately 15 μm x 5 μm x 0.25 μm sampling a cross section of the nanoparticle film and the silicon substrate was cut. Subsequently this section was further polished in the ion beam and observed under the TEM for finding the dimension of the nanoparticles in the thickness direction and is shown in Figure 16.

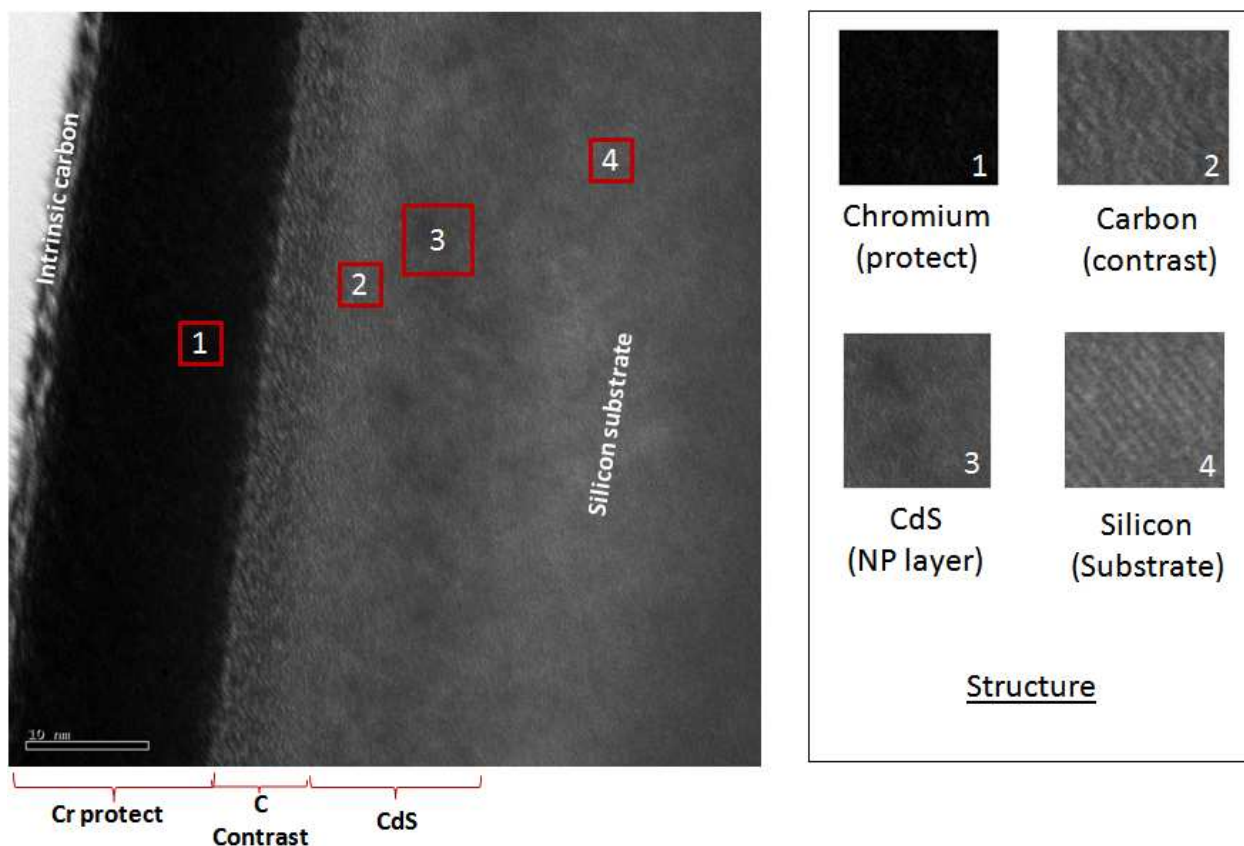


Figure 16. Cross sectional TEM image showing differentiation in contrast from various layers and zoomed areas showing structure

It can be easily observed that the CdS nanoparticle layer is 10 nm thick and within this layer sub 10 nm features could be discerned suggesting that the 22 nm hexagonal platelets have a thickness less than 10 nm. In order to validate whether the hexagonal platelets could be formed only in the sonochemical route a study using conventional heating using a hot plate for the same chemistry was performed. Yellow precipitates were formed and were prepared for subsequent TEM examination. The results are shown in Figure 17 below.

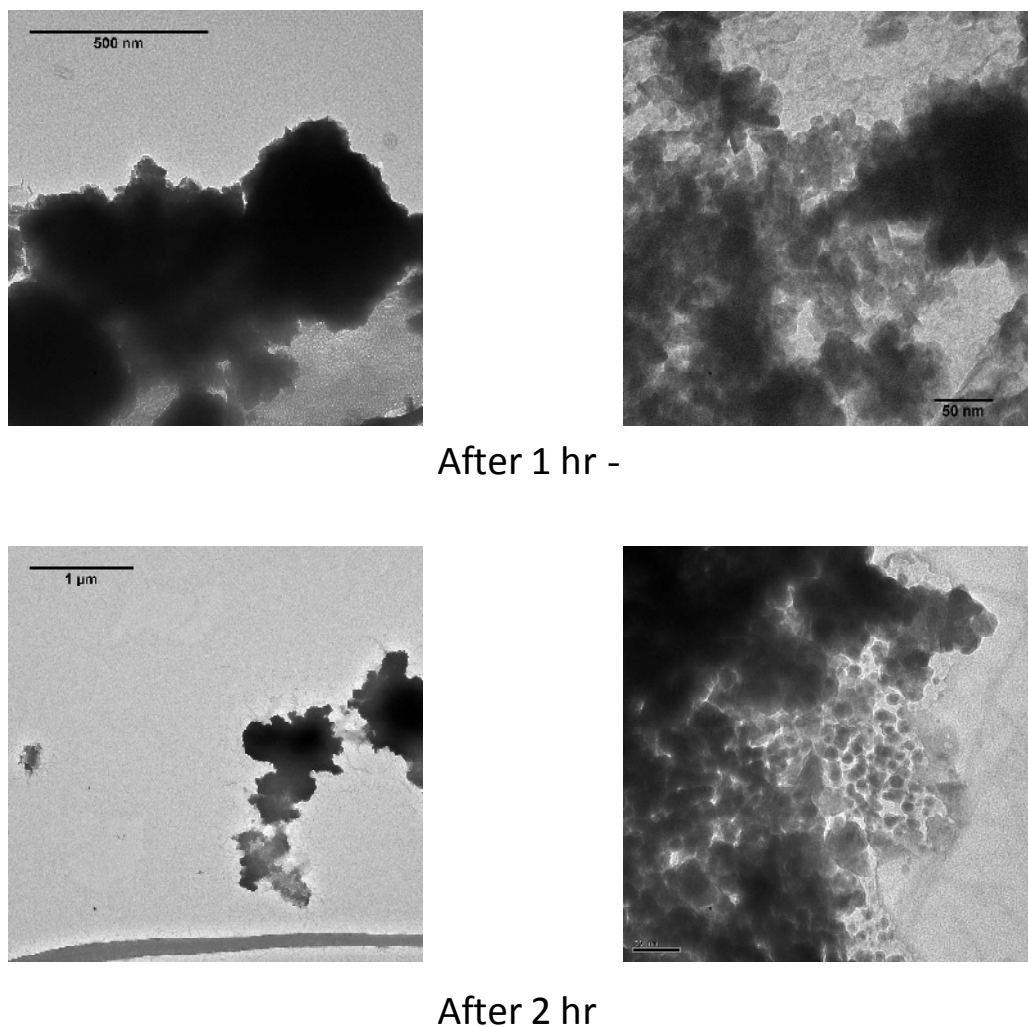


Figure 17. Particle morphology of CdS in batch conventional heating induced synthesis

It can be observed that the particle size varies from about 20 nm to 0.5 μ m after 1 hour synthesis time and varies from about 20 nm to 1 μ m after 2 hours synthesis time. It is obvious that the size dispersion is really poor and it is notable that there are no hexagonal shaped particles. Even after 2 hours of synthesis it can be seen that there are long strands of unreacted thiourea spanning several μ m as seen from bottom left image in Figure 17.

This shows that hexagonal shaped CdS nanoparticles are observed only in the sonochemical route and to a higher degree in the continuous mode.

Further, phase identification was carried out using x-ray diffraction on the CdS chemistry wherein different heating modes are compared as shown in Figure 18 below.

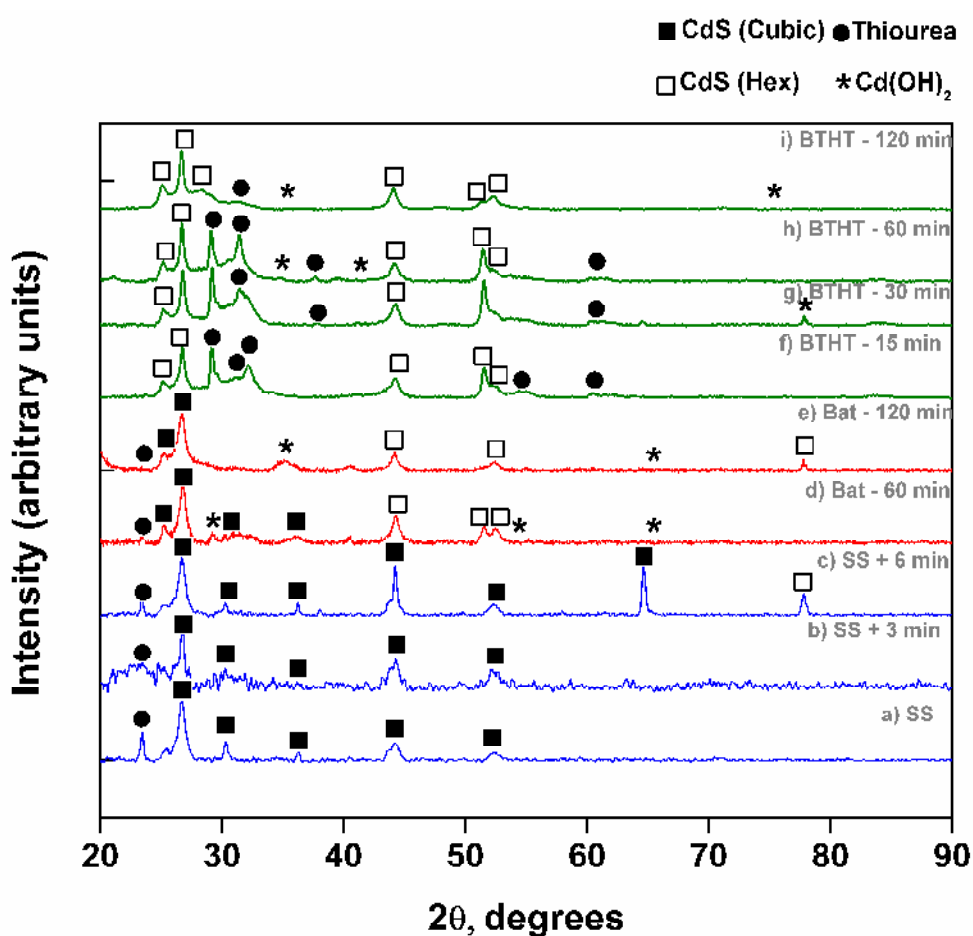


Figure 18. Crystal structure identification of CdS nanoparticles using x-ray diffraction [SS - Onset of steady state in continuous ultrasound heating, Bat – Batch ultrasound induced heating, BTHT – Batch conventional heating]

From the XRD results, it can be observed that there are more cubic CdS peaks in continuous mode when compared to batch synthesis where majority of the peaks belong to hexagonal CdS. The patterns were indexed using standards 80-0006 for hexagonal CdS and 89-0440 for cubic CdS in conjunction with ICDD PDF-2 database. A solitary thiourea peak from (020) plane due to incomplete conversion is observed in the continuous mode. The peak intensity is found to decrease in batch synthesis in 60 minutes of reaction time and almost disappears at 120 minutes suggesting higher conversion of reactants. This is typical in continuous synthesis routes involving higher than room temperature reactions. In conventional heating, it can be observed that all the CdS peaks are of hexagonal crystal structure and there are no cubic CdS peaks. This shows that the metastable hexagonal CdS cannot be achieved in conventional heating for the same chemistry. It can also be noted that there are thiourea peaks present in this synthesis mode and as synthesis time increases the thiourea peaks reduce in number suggesting completion of the reaction and higher utilization of the reactants. There appears to be cadmium hydroxide peaks which is an intermediary phase during the reaction in both batch ultrasound heating and batch conventional heating. This suggests that the sulfur is not being used up completely in the reaction for synthesis of CdS.

Several factors influence the crystal structure of CdS particles vital ones being cadmium source and sulfur source. In general when sodium sulfide is used as a reactant, it entails formation of cubic CdS even with various Cd sources while usage of organic sulfur sources (thio groups) generally result in formation of mixture of cubic and hexagonal phases of CdS [37]. In sonochemical synthesis, the structure is in addition affected by

ultrasound and kind of sonication (dispersed vs. intense). Also solvation of the reagents and interfacial forces for various kinds of Cd salt solutions affect structure [26]. Typical vapor phase methods for production of high aspect ratio particles (belts, tubes and wires) involve temperatures above 800°C [38] and result in formation of hexagonal CdS. Cubic CdS is reported to be a metastable phase [39] as opposed to hexagonal CdS and reverts to this structure upon heating to temperatures above 300°C [40]. Continuous sonochemical synthesis of CdS appears to have stabilized cubic phase in a high aspect ratio nanoparticles (hexagonal platelets) in this case. It is to be noted that typical microwave synthesis i.e. another high energy rapid heating technique yields hexagonal CdS particles [41].

Further, large scale compositional sampling of approx $4\text{ }\mu\text{m}^3$ was performed using wave dispersive spectroscopy to look at compositional homogeneity in the precipitates. The results are summarized in Figure 19.

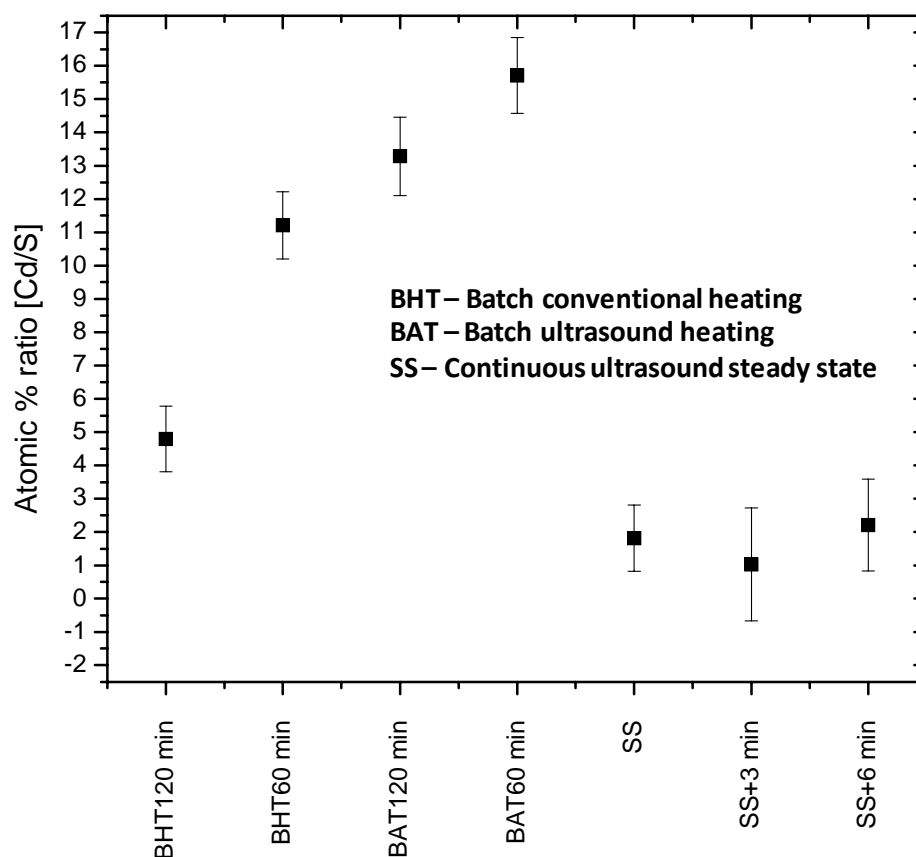


Figure 19. Compositional homogeneity shown as atomic % ratio of Cd to S in various samples (BHT – Batch conventional heating, BAT – Batch ultrasound heating, SS – Continuous ultrasound heating at steady state)

Upon examining the above results, it can be noted that for the steady state continuous synthesis the atomic ratio is very close to the expected 1:1 for Cd:S within the standard error limits. For conventional heating the ratio is much greater than 1 while in batch ultrasound it is worse showing very high cadmium concentration. This is congruent to what was observed in the XRD results showing presence of intermediary $\text{Cd}(\text{OH})_2$ phase along with unreacted thiourea. This suggests that continuous sonochemical synthesis

yields much better purity CdS and also suggests higher utilization of the reactants for synthesis of CdS.

4. Conclusions

Two sets of conclusions can be drawn from this work. First, continuous sonochemical synthesis is capable of producing a meta-stable phase of CdS in the form of high aspect ratio platelets. The phase and shape of the NPs provide evidence of high reaction temperatures. Second, relative to the other processes investigated in this study, continuous sonochemical synthesis provides an 8X reduction in processing time while exhibiting good size and compositional uniformity of the product. At steady state, the size of the hexagonals averaged 21.0 nm in diameter with an average coefficient of variation of 27.4%. The thickness of the nanoplatelets was found to be less than 10 nm opening the possibility of quantum confinement and application as quantum wells.

5. Acknowledgements

The work described herein was funded by the US Department of Energy, Industrial Technologies Program, through award #NT08847, under contract DE-AC-05-RL01830. Additional funds were received from the Oregon Nanoscience and Microtechnologies Institute (ONAMI) under a matching grant to Oregon State University. The facilities and equipment resident at the Microproducts Breakthrough Institute (MBI) and the Oregon Process Innovation Center (OPIC) were crucial in conducting this study. The authors would also like thank Mr Neill Thornton (MBI) for his help in the high speed photography.

6. References

- [1] Mason, T. J., and Phillip, J., 2002, *Applied sonochemistry*, Wiley-VCH Weinheim, Germany.
- [2] Ley, S. V., and Low, C. M. R., 1989, *Ultrasound in synthesis*, Springer-Verlag Berlin, Germany.
- [3] Colussi, A., Weavers, L. K., and Hoffmann, M. R., 1998, "Chemical bubble dynamics and quantitative sonochemistry," *The Journal of Physical Chemistry A*, 102(35), pp. 6927-6934.
- [4] van Eldik, R., and Hubbard, C. D., 1996, *Chemistry under extreme and non-classical conditions*, Wiley.
- [5] Suslick, K. S., and Flannigan, D. J., 2008, "Inside a collapsing bubble: sonoluminescence and the conditions during cavitation," *Annu. Rev. Phys. Chem.*, 59, pp. 659-683.
- [6] Suslick, K. S., and Price, G. J., 1999, "Applications of ultrasound to materials chemistry," *Annual Review of Materials Science*, 29(1), pp. 295-326.
- [7] Suslick, K., Fang, M., Hyeon, T., and Mdeleleni, M., 1999, *Applications of sonochemistry to materials synthesis*, Kluwer Publishers: Dordrecht, Netherlands.
- [8] Ciawi, E., Rae, J., Ashokkumar, M., and Grieser, F., 2006, "Determination of temperatures within acoustically generated bubbles in aqueous solutions at different ultrasound frequencies," *The Journal of Physical Chemistry B*, 110(27), pp. 13656-13660.
- [9] Neppiras, E. A., 1980, "Acoustic cavitation," *Physics reports*, 61(3), pp. 159-251.
- [10] 1949, "Minutes of the 1948 Annual Meeting at New York, January 26-29, 1949," *Physical Review*, 75(8), pp. 1279-1336.
- [11] Mastai, Y., and Gedanken, A., 2006, "Sonochemistry and Other Novel Methods Developed for the Synthesis of Nanoparticles," *ChemInform*, 37(17), pp. no-no.
- [12] Margulis, M. A., and Grundel, L. M., 1982, "Study of physicochemical processes occurring in a liquid in the presence of low-frequency acoustic vibrations. II. Physicochemical effects resulting from gas bubble pulsations at low sonic frequencies," *Zh. Fiz. Khim.*, 56(Copyright (C) 2012 American Chemical Society (ACS). All Rights Reserved.), pp. 1941-1945.
- [13] Luche, J. L., 1987, "Organometallic sonochemistry: successes, problems and by-products," *Ultrasonics*, 25(Copyright (C) 2012 American Chemical Society (ACS). All Rights Reserved.), pp. 40-44.
- [14] Schumb, W. C., Peters, H., and Milligan, L. H., 1937, "A new method for studying cavitation erosion of metals," *Met. Alloys*, 8(Copyright (C) 2012 American Chemical Society (ACS). All Rights Reserved.), pp. 126-132.
- [15] Horton, J. P., 1953, "The effect of intermolecular bond strength on the onset of cavitation," *J. Acoust. Soc. Am.*, 25(Copyright (C) 2012 American Chemical Society (ACS). All Rights Reserved.), pp. 480-484.
- [16] Chow, R., Blindt, R., Chivers, R., and Povey, M., 2005, "A study on the primary and secondary nucleation of ice by power ultrasound," *Ultrasonics*, 43(4), pp. 227-230.

- [17] Luque de Castro, M., and Priego-Capote, F., 2007, "Ultrasound-assisted crystallization (sonocrystallization)," *Ultrasonics Sonochemistry*, 14(6), pp. 717-724.
- [18] Fujimoto, T., Terauchi, S.-y., Umehara, H., Kojima, I., and Henderson, W., 2001, "Sonochemical Preparation of Single-Dispersion Metal Nanoparticles from Metal Salts," *Chemistry of materials*, 13(3), pp. 1057-1060.
- [19] Mizukoshi, Y., Okitsu, K., Maeda, Y., Yamamoto, T. A., Oshima, R., and Nagata, Y., 1997, "Sonochemical Preparation of Bimetallic Nanoparticles of Gold/Palladium in Aqueous Solution," *The Journal of Physical Chemistry B*, 101(36), pp. 7033-7037.
- [20] Siddiqui, S. W., Unwin, P. J., Xu, Z., and Kresta, S. M., 2009, "The effect of stabilizer addition and sonication on nanoparticle agglomeration in a confined impinging jet reactor," *Colloids and Surfaces A: Physicochemical and Engineering Aspects*, 350(1), pp. 38-50.
- [21] Shalom, D., Wootton, R. C. R., Winkle, R. F., Cottam, B. F., Vilar, R., deMello, A. J., and Wilde, C. P., 2007, "Synthesis of thiol functionalized gold nanoparticles using a continuous flow microfluidic reactor," *Materials Letters*, 61(4-5), pp. 1146-1150.
- [22] Sugano, K., Uchida, Y., Ichihashi, O., Yamada, H., Tsuchiya, T., and Tabata, O., 2010, "Mixing speed-controlled gold nanoparticle synthesis with pulsed mixing microfluidic system," *Microfluidics and Nanofluidics*, pp. 1-10.
- [23] Peterson, D. A., Chandran, P., and Paul, B. K., "A Reverse Oscillatory Flow microreactor system for the synthesis of uniformly-size CdS nanoparticles," *Proc. Nanotechnology (IEEE-NANO)*, 2011 11th IEEE Conference on, IEEE, pp. 666-670.
- [24] Salazar-Alvarez, G., Muhammed, M., and Zagorodni, A., 2006, "Novel flow injection synthesis of iron oxide nanoparticles with narrow size distribution," *Chemical Engineering Science*, 61(14), pp. 4625-4633.
- [25] Pan, Y., Ju, M., Yao, J., Zhang, L., and Xu, N., 2009, "Preparation of uniform nano-sized zeolite A crystals in microstructured reactors using manipulated organic template-free synthesis solutions," *Chemical Communications*(46), p. 7233.
- [26] Ghows, N., and Entezari, M., 2011, "A novel method for the synthesis of CdS nanoparticles without surfactant," *Ultrasonics Sonochemistry*, 18(1), pp. 269-275.
- [27] Wang, H., Luf, Y., and Zhu, J., "Preparation of Cube-Shaped CdS Nanoparticles by Sonochemical Method," *World Scientific Pub Co Inc*, p. 63.
- [28] Wang, S. F., Gu, F., and Lü, M. K., 2006, "Sonochemical synthesis of hollow PbS nanospheres," *Langmuir*, 22(1), pp. 398-401.
- [29] Xie, R., Li, D., Yang, D., and Jiang, M., 2006, "Surface synthesis of PbS nanoparticles on silica spheres by a sonochemical approach," *Journal of Materials Science*, 42(4), pp. 1376-1380.
- [30] Banert, T., Horst, C., Kunz, U., and Peuker, U., 2004, "Continuous precipitation in an ultrasonic flow reactor as illustrated by iron(II, III) oxide," *Chem. Ing. Tech.*, 76(Copyright (C) 2013 American Chemical Society (ACS). All Rights Reserved.), pp. 1380-1381.
- [31] Banert, T., Brenner, G., and Peuker, U. A., 2006, "Operating parameters of a continuous sono-chemical precipitation reactor," *Proc. 5. WCPT*, Orlando, FL, pp. 23-27.
- [32] Yasui, K., Iida, Y., Tuziuti, T., Kozuka, T., and Towata, A., 2008, "Strongly interacting bubbles under an ultrasonic horn," *Physical Review E*, 77(1), p. 016609.

- [33] Gao, T., Li, Q., and Wang, T., 2005, "Sonochemical synthesis, optical properties, and electrical properties of core/shell-type ZnO nanorod/CdS nanoparticle composites," *Chemistry of materials*, 17(4), pp. 887-892.
- [34] Mugdur, P. H., Chang, Y. J., Han, S. Y., Su, Y. W., Morrone, A. A., Ryu, S. O., Lee, T. J., and Chang, C. H., 2007, "A Comparison of Chemical Bath Deposition of CdS from a Batch Reactor and a Continuous-Flow Microreactor," *J. Electrochem. Soc.*, 154(9), pp. D482-D488.
- [35] Chang, Y. J., Su, Y. W., Lee, D. H., Ryu, S. O., and Chang, C. H., 2009, "Investigate the Reacting Flux of Chemical Bath Deposition by a Continuous Flow Microreactor," *Electrochem. Solid-State Lett.*, 12(7), pp. H244-H247.
- [36] Bettelheim, F. A., Brown, W. H., Campbell, M. K., Farrell, S. O., and Torres, O. J., 2012, *Introduction to organic and biochemistry*, Thomson Brooks/Cole.
- [37] Fu, Z., Zhou, S., Shi, J., and Zhang, S., 2005, "Effects of precursors on the crystal structure and photoluminescence of CdS nanocrystalline," *Mater. Res. Bull.*, 40(9), pp. 1591-1598.
- [38] Zhai, T., Fang, X., Li, L., Bando, Y., and Golberg, D., 2010, "One-dimensional CdS nanostructures: synthesis, properties, and applications," *Nanoscale*, 2(2), pp. 168-187.
- [39] Gorer, S., Kodes, G., Sorek, Y., and Reisfeld, R., 1997, "Crystal phase transformation in sol-gel films of nanocrystalline CdSe and CdS," *Mater. Lett.*, 31(3), pp. 209-214.
- [40] Wan, L., Bai, Z., Hou, Z., Wang, D., Sun, H., and Xiong, L., 2010, "Effect of CdCl₂ annealing treatment on thin CdS films prepared by chemical bath deposition," *Thin Solid Films*, 518(23), pp. 6858-6865.
- [41] Amutha, R., Muruganandham, M., Lee, G., and Wu, J., 2011, "Facile Microwave-Combustion Synthesis of Wurtzite CdS Nanoparticles," *J. Nanosci. Nanotechnol.*, 11(9), pp. 7940-7944.

Chapter 4

THE ABRASION RESISTANCE OF SILICA NANOPARTICLE-BASED MOTHEYE ANTIREFLECTIVE COATINGS ON GLASS

Abstract

Motheye antireflective coatings are based on periodic or stochastic features with dimensions below the wavelength of visible light which can be used to produce a gradient index of refraction between air and the substrate. In this manner, motheye coatings are not strictly dependent upon material properties and, therefore, can be applied to wider range of applications when compared with more traditional quarter-wavelength films. In this work, two silica nanoparticle-based motheye antireflective coatings of equivalent optical performance but different physical structure are deposited on glass and investigated regarding abrasion resistance. Optical and abrasion performance were evaluated in light of the mechanical properties and physical structure of the films using mechanistic and statistical models. Optical performance of the three layer film was found to be 6% higher than the single layer coating. A three layer coating was found to have better abrasion resistance than a simple single layer coating. A simple single layer film showed better crack propagation resistance than a three layer film due to nanoparticles resisting crack growth while the three layer film had higher work of adhesion thus exhibiting better delamination resistance. The three layer film also had a higher crack nucleation resistance, scratch resistance and spallation resistance. These results suggest

that the mechanical performance of gradient coatings can be decoupled from optical performance in the design of these coatings.

1. Introduction

Antireflective coatings (ARCs) can be broadly grouped into quarter wavelength and gradient film structures [1]. Quarter wavelength (QW) structures work on the principle of destructive interference [2]. The thickness of the film must be $n\lambda/4$ where n is an odd number. Theoretically, waves reflected off of the film-substrate interface are 180 degrees out of phase with the incident light causing destructive interference and, thereby, reducing reflection. QW films are wavelength dependent and therefore are less effective for broadband antireflection. Multilayer QW films can improve broadband performance however production becomes more complex and expensive. Further, because the physical principle relies upon the thickness of the film, QW films are less effective as the angle of incidence departs from 90 degrees. Because of the thickness precision required, most QW films use vapor phase deposition techniques which have high capital and operating costs associated with high temperature, vacuum-based processing and slow deposition rates [3, 4]. The performance of QW films improves as the refractive index of the film approaches that halfway between the refractive indices of the substrate and the surrounding media. For air-glass applications, few materials exist with these properties.

Bernhard was a pioneer in understanding the antireflective nature of the cornea in night-flying moths [5, 6]. These moths' eyes were found to consist of rounded pillars about 200 nm high with about 300 nm center to center spacing. It was hypothesized that this

structure, with dimensions below the wavelength of visible light, provided a gradient refractive index from that of air to the receptors in the eye, eliminating a sudden change in the refractive index (RI) and the associated spectral reflection [5]. These gradient structures perform better across a wider spectrum of wavelengths than QW films [7]. RI gradients have been demonstrated using periodic surface structures [8, 9] as well as with stochastic surface structures [1] with the use of etching [10] and stochastic subsurface structures such as with the use of porosity [11, 12].

While the optical properties of gradient films are excellent, often there are other demands from field application of the coatings. The mechanical robustness of optical coatings is important for the scratch resistance of smart phones or the abrasion resistance of solar cell cover glass. Although gradient films are easier to manufacture because of the widely used sol-gel approach [13, 14], the nature of gradient films makes them vulnerable to poor mechanical performance. Air-glass gradient films are essentially a composite of air and glass. By definition, the top of these structures generally lacks mass. While this strategy works great for optical performance, it makes the coating susceptible to mechanical damage [15].

1.1 Thin Film Mechanical Behavior

The focus of this paper is to understand the factors contributing to the abrasion resistance of gradient ARCs. Based on a review of the technical literature, several terms are defined below in Table 10 to help describe the investigative approach taken in this paper [16-19].

Table 10 Descriptive terms for mechanical behavior of ARC thin films

Test Method	Film Performance/ Film Property	Definition	Metric
Abrasion	Abrasion resistance	Resistance to the removal of film mass based on the application of a traversing abrasive media (i.e. multiple tips) under normal load	Mean residual (mean $\Delta\%R$ before/ mean $\Delta\%R$ after abrasion)
Nanoindentation	Crack resistance	Resistance to crack initiation under the application of a normal load.	Critical load for cracking (P), Fracture toughness (K_{IC})
Scratch	Crack propagation	Resistance to the appearance of a visible crack under the application of a single traversing tip with increasing normal load as a function of time.	Lower critical load (L_{CI})
Scratch	Delamination resistance	Resistance to interlaminar crack propagation	Work of adhesion (W_a)
Scratch	Spallation resistance	Resistance of a material to fail under gross material removal when the delamination cracks get arrested at the interface	Strain energy release rate (g)

Current standards exist to evaluate the abrasion resistance of thin films. In this paper, these standards were used to guide the evaluation of the abrasion resistance of gradient films. Scratch and nanoindentation testing methods were used to determine important film properties required of mechanical performance models. These methods were selected to most closely ascertain material and film properties due to the similarity in dynamic loading conditions incurred during abrasion testing. The measured material and film property data was used to inform a well-developed set of energy-based and stress-based models (described below) originally developed to quantify the mechanical behavior of homogeneous films. To date, no attempt has been made to use these models to describe the behavior of non-homogeneous films such as gradient ARCs. The ARCs considered here are inorganic polymer nanocomposites consisting of very fine nanoparticles embedded within a Si-based polymer matrix having a very fine distribution of pores.

1.2 Models of Thin Film Mechanical Behavior

1.2.1. Quantitative Model for Crack Resistance [20-25]

The first line of defense for mechanical failure is to avoid crack nucleation. The critical load (in millinewtons) for cracking under indentation (P) can be described as a function of both the elastic modulus and hardness of the film (H) given by Malzbender's model [24]

$$P = \frac{E_r h^2}{\left[0.2 \sqrt{\frac{E_r}{H}} + 0.75 \sqrt{\frac{\pi}{4}} \sqrt{\frac{H}{E_r}} \right]^2} \quad (10)$$

Where h is the penetration depth and E_r is the reduced elastic modulus of the film accounting for indenter deformation and the actual contact area of the indenter. Since P describes the load at which cracking initiates, this term is used to describe the crack nucleation resistance of the films.

A more normalized evaluator for crack propagation resistance is fracture toughness. This is because fracture toughness indicates the resistance of the material for crack growth. In nanoindentation, the fracture toughness (in $\text{MPa}\sqrt{\text{m}}$) is related to the indentation load using the following equation [22]

$$K_{IC} = 0.016 \left(\frac{E}{H} \right)^{0.5} \frac{P}{c^{1.5}} \quad (11)$$

Where c is the length of radial cracks. Since it is difficult to measure the length of the radial cracks, the crack size was estimated using the model proposed by Bull et al [26] using the relation

$$c = h_m \cot \varphi + \left(Q \frac{E_r}{H} - 1 \right) h_{ex} \cot \varphi \quad (12)$$

Where h_m is the maximum depth of penetration, φ is the face-to-center angle of the indenter, Q is a constant, H is the hardness and h_{ex} is the extra penetration caused when

the indenter tip enters a crack. This “pop-in” phenomenon can be observed in the load versus displacement curve obtained during nanoindentation. In the results obtained in our nanoindentation tests, no such pop-in phenomenon was observed and hence h_{ex} was taken as zero reducing equation 3 to

$$c = h_m \cot \varphi \quad (13)$$

The computed value of c can be plugged into equation 2 above to compute the fracture toughness of the coating.

Thus P and K_{IC} together describe the crack resistance of the films considering both crack nucleation and crack propagation.

1.2.2. Quantitative Model of Scratch and Delamination Resistance [27-29]

Scratch tests involve applying a normal load and a tangential load across a sample surface using a stylus. The load is applied progressively until the point of gross failure of the coated sample [28]. Appearance of cracks is usually marked by a lower critical load (L_{C1}) and delamination occurs at L_{C2} . The lower critical load (L_{C1} ; in Newtons) is a measure of resistance to scratching or crack propagation while L_{C2} (in Newtons) can be used to compute the work of adhesion between the film and the substrate. The work of adhesion is a metric for delamination resistance and preferred over experimentally measured L_{C2} as W_a considers other parameters like elastic modulus, friction coefficient and film thickness and is hence a comprehensive function. The critical load for delamination, L_{C2} , is calculated in general using the model derived by Bull et al [27]:

$$L_{c2} = \frac{A}{v\mu} \left(\frac{2EW_a}{t} \right)^{0.5} \quad (14)$$

where A is the cross-sectional area of the scratch, E is the elastic modulus of the film, v is the Poisson's ratio of the film, t is the thickness of the film, μ_c is the coefficient friction and W_a is the work of adhesion between the film and the substrate. The above equation suggests that delamination resistance increases with a decrease in μ_c and t and an increase in E and W_a .

The above expression was modified by Attar and Johannesson [29] since the tangential force causing coating removal does not act on the total scratch track cross-sectional area but only on the cross-section of the coating. The modified expression is given by,

$$L_{c2} = \frac{d}{v\mu} (2tEW_a)^{0.5} \quad (15)$$

where d is the scratch width. Attar et al also observed that concentrated load causes interface failure and flaking simultaneously. This expression can be rewritten to compute the work of adhesion (in Joules/meter²) based on the experimentally measured L_{C2} from the scratch test as follows:

$$W_a = \frac{L_{c2}^2 v^2 \mu^2}{2d^2 t E} \quad (16)$$

1.2.3. Model for Spallation Resistance [30]

Spallation is the severest failure mechanism and signifies termination of the cracks as they reach the film-substrate interface causing material removal. During buckling failure

of the film, delamination may occur resulting in an energy release rate (in Joules/meter²) during crack growth given by:

$$g = \frac{1}{2\pi a} \left(\frac{d\Delta U}{da} \right) = (1-\nu)(1-\alpha)t(\sigma_0^2 - \sigma_c^2) / E \quad (17)$$

where a is the crack radius, ΔU is the energy difference, ν is the Poisson's ratio, α is a constant, t is the film thickness, σ_c is the critical stress, σ_0 is the compressive yield stress, and E is the elastic modulus. The energy release rate during crack growth is the energy rate input into the coating needed for the cracks to reach the interface leading to spallation of the coating off the substrate. The higher this rate, the better the resistance of the film to spallation. In the above expression, the critical stress (in Pascals) is given by Hutchinson's equation [31]

$$\sigma_c = \left[\frac{\pi^2 E}{12(1-\nu^2)} \right] \left(\frac{t}{a} \right)^2 \quad (18)$$

Based on the work of adhesion given by [32, 33], the stress for delamination (in Pascals) is calculated using:

$$\sigma = \sqrt{\frac{2EW_a}{t}} \quad (19)$$

Assuming that spallation occurs when the compressive yield stress in the film equals the stress for delamination, the above two parameters can be inserted into Equation 8 to compute the spallation resistance of the film.

1.3 Factors Affecting the Mechanical Properties of Nanoparticle Thin Films

Many gradient ARCs consist of morphologies with nanoparticles (NPs). The mechanical properties of thin films composed of NPs have been found to be dependent on several related factors most of which are material related. The important factors are discussed below:

a. *Interface energy* [34]

Considering the interface between the two materials that form the interface, the interface energy is composed of two components with one dependent on the chemical bonding contribution and the other on the structure-strain contribution. Liang et al showed that the structure interface energy component varies logarithmically with particle size and, hence, the larger the particle size, the larger the structure interface energy up to about 20 nm for Ag/MgO and Ni/Al₂O₃. Macroscopic fracture toughness is dependent on the structure related interfacial energy at the nano-scale.

Interfacial adhesion [17, 23]

Interfacial adhesion can be defined as the film-substrate interface resistance to crack growth and is a function of the energy required to cause plastic deformation in the film as the crack propagates to the interface.

Nanoparticle size effects [27, 35]

Fine silica nanoparticles have been found to exhibit both ductile and brittle behavior which has been hitherto unobserved in bulk silica. This leads to interesting effects like

strain hardening and reverse plastic deformation (RPD). The mechanism of RPD is still unclear however it is possibly caused by thermal fluctuations leading to annealing. The localized plastic deformation ahead of the crack tip has been found to be dependent on NP size for non-amorphous NP based coatings.

Viscous flow of binder phase [18]

Most gradient ARCs have a binder phase composed of inorganic or organic polymers which improves the adherence of the NPs to the substrate improving the mechanical properties of the film as a whole. Constant load or near constant load conditions on the film surface can cause viscous flow of the binder phase and can affect the composite behavior of the film.

Measurement errors [36]

It is important to note that measurement errors are as much a critical factor in evaluation of mechanical properties as the material properties themselves. It has been shown that indenter tip deformation during the common nanoindentation test can cause ~7% error when coupled with the non-uniform contact occurring from rough surfaces.

Other factors that have been attributed to affecting the mechanical behavior of nanoparticle coatings include [26]:

1. Elastic modulus
2. Poisson's ratio
3. Hardness
4. Fracture toughness

5. Volume % of hard phases/particles
6. Fractional density
7. Cross-linking density
8. Friction coefficient
9. Pre-existing flaws
10. Residual stress
11. Substrate hardness

It is expected that many of these may be explained by the models developed for homogeneous films described above.

1.4 Objective

Several authors have reported on the scratch or abrasion resistance of nanoparticle-based ARCs produced using sol-gel processes [37-39]. However, these reports provide little insight into the relationship between the structure, properties and processing of the films and the impact of each on mechanical performance. In this paper we attempt to investigate this relationship for two different gradient ARCs with equivalent optical performance. Efforts are first made to identify ARC recipes that are repeatable and robust. Next, different ARC structures with equivalent optical performance are used to explore the attributes of the films that dictate mechanical behavior.

2. Experimental methods

The primary test variable used for optical performance was mean antireflection ($\Delta\%R$) in comparison with the base substrate reflection for spectral reflectance between wavelengths of 400 – 900 nm. As described above, the metric used to assess mechanical

performance was the mean residual AR remaining after abrasion which was equal to the mean $\Delta\%R$ after abrasion divided by $\Delta\%R$ before abrasion.

Preliminary efforts were used to evaluate the optical and mechanical repeatability of various silica-on-glass ARC processing techniques. The results of these experiments can be found in Appendix 2.1.

Two methods for producing films were selected to provide a contrast in the physical structure of the films for analysis. One method chosen was a single layer (1L) film based on the recipe developed by Henning et al [40] and Hæreid et al [41] using Tetra Methyl Ortho Silicate (TMOS) as a principal reactant to synthesize a very fine silica nanoparticle dispersion in suspension termed TMOS-b gel. A second film consisted of a three layer (3L) film in which the middle film used the same procedure as above with the top and bottom layers consisting of a TMOS suspension synthesized in acidic medium using HCl denoted as TMOS-a gel. The as-synthesized nanoparticle suspensions were diluted to 50 vol. % and used to coat the smooth side of textured glass substrates containing 69-74% SiO_2 , 10-16% Na_2O , 5 to 14% CaO , 0 – 6% MgO and 0-3% Al_2O_3 (AGC Solite) [42]. A spin coating technique followed by Han et al [43] was used to deposit the wet films followed by heat treatment to synthesize the final nanoparticle microstructure similar to that observed elsewhere [44]. A schematic of the film structures are shown in the Figure 20 below.

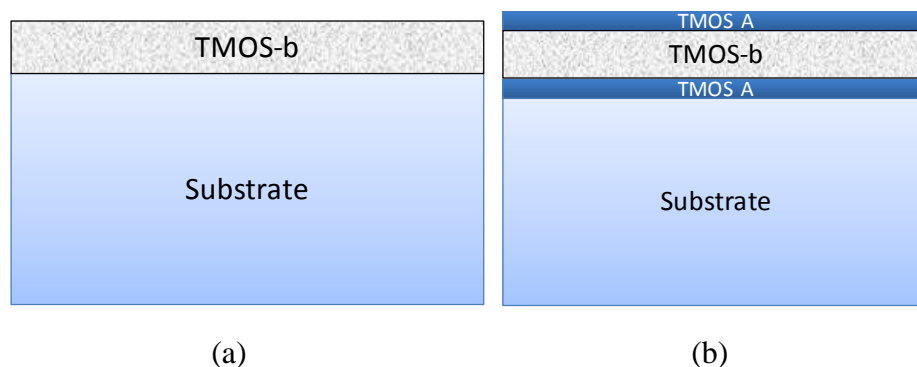


Figure 20. Schematic of the silica based ARC for (a) 1L and (b) 3L

Through experimentation, it was found that the coating spin speed and heat treatment time and temperature were all important for the optical performance of both films. Based on a first experimental design involving spin speed, two equivalent optical films were selected for exploring differences in mechanical performance. The mean and standard deviation for the optical performance of the two films was 3.27 ± 0.24 (1L) and 3.11 ± 0.18 (3L). These conditions were achieved at a spin speed of 1500 RPM for 1L and 1800 RPM for 3L. Specific results are listed in Appendix A2.2.

Based on these results, a final factorial design was proposed to understand the interdependence of annealing conditions on film structure, mechanical properties and performance. The experimental design is shown in Table 11.

Table 11. General factorial design for annealing conditions

Std	Run	Temperature	Time
Order	Order	°C	min
4	1	595	10
8	2	610	30
1	3	580	10
3	4	580	60
6	5	595	60
7	6	610	10
2	7	580	30
9	8	610	60
5	9	595	30

The above design was carried out with two duplicates resulting in 3 samples per condition spread over 9 conditions for a total of 27 test articles. The optical performance before and after abrasion was measured in three different locations for each sample providing a total of 81 measurements before and after abrasion testing. For the processing conditions highlighted in structural analysis, one sample for each processing condition was used for scratch and nanoindentation. A set of three scratches and three indents were performed on each sample for extracting test data.

A UV-VIS spectrophotometer (JASCO V-670) equipped with an integrating sphere was used to measure reflectance of the coated glass samples. The cross-sectional and surface morphologies were characterized by scanning electron microscopy (SEM, FEI Quanta 600 FEG) operating at 20 kV and transmission electron microscopy (FEI TITAN Chemi-

STEM) operating at 200 kV. Cross-sections of size $15\ \mu\text{m} \times 6\ \mu\text{m} \times 0.2\ \mu\text{m}$ were prepared using focused ion beam (FIB) milling cross-sectioning techniques (FEI Quanta 3D Dual Beam SEM/FIB). The sample preparation steps are outlined in the Appendix 1. A CSM Instruments MicroScratch Tester (S/N 01-02526) with a $50\ \mu\text{m}$ radius spheroconical indenter was used to perform scratch testing at a peak load of 700 mN over a track length of 1.4 mm at a loading rate of 500 mN/min. Abrasion testing was evaluated using the test apparatus shown in Figure 21 which is a modified version of the EN1096-2 coated glass testing standard. A high density felt was used as the abrading medium with no circular motion on the boom. Samples were measured for change in reflectance before and after abrasion testing.

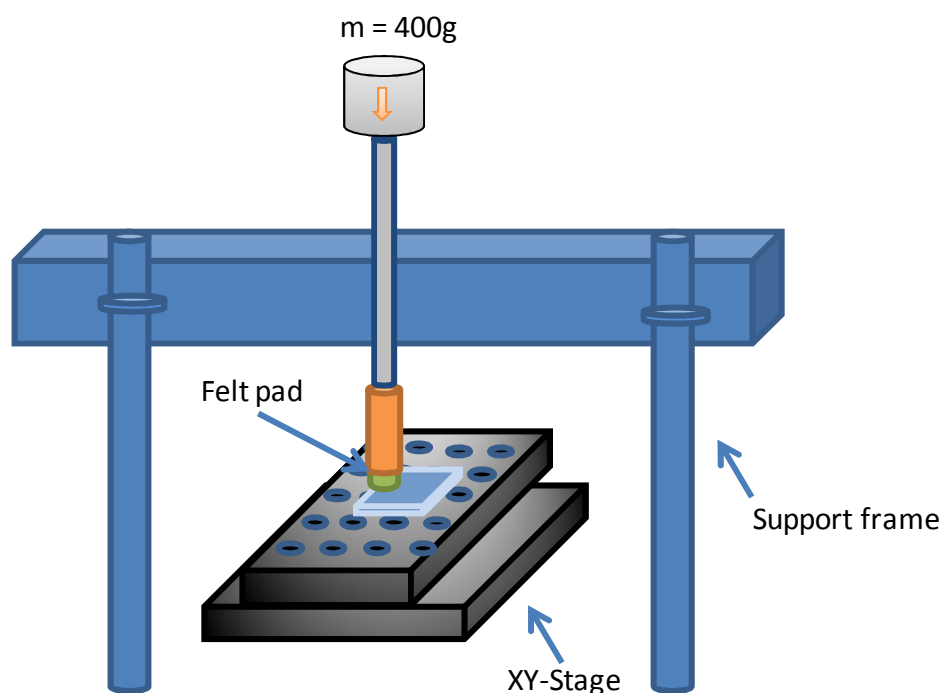


Figure 21. Schematic of abrasion test rig for felt abrasion test

3. Results and discussion

3.3. Understanding mechanical behavior

3.3.1 Structure performance correlation

After completing the experimental runs in Table 11, the optical and mechanical performance of the two films as a function of annealing time and temperature were computed as shown in Figure 22. These plots use standard error bars.

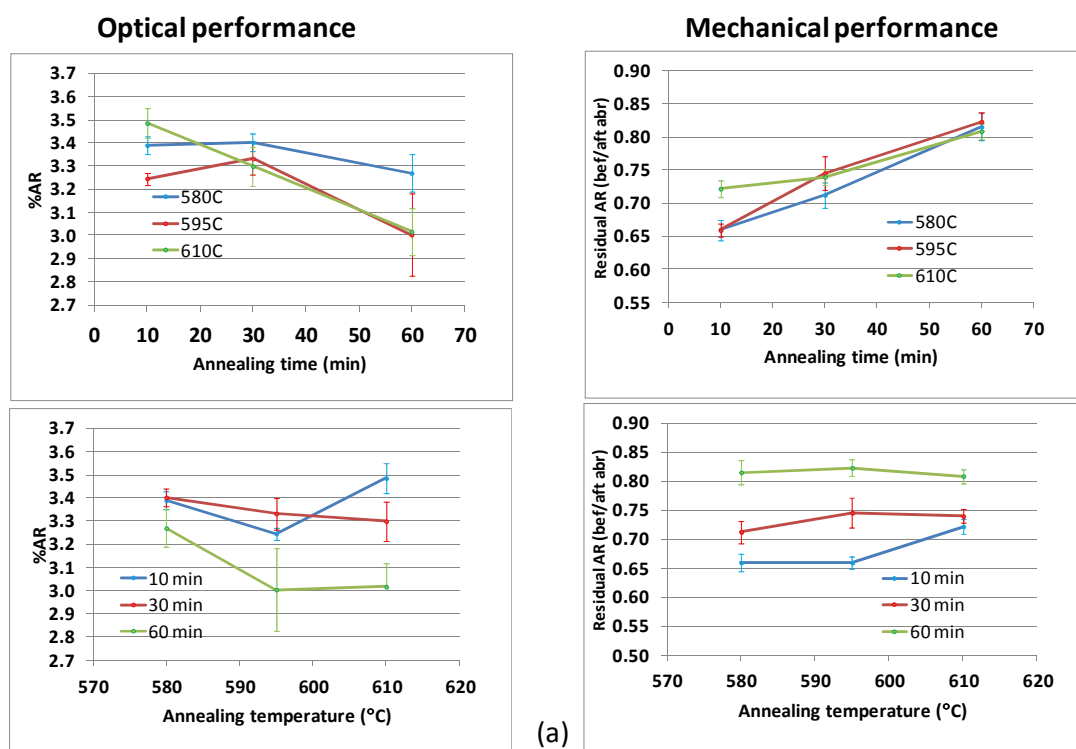


Figure 22

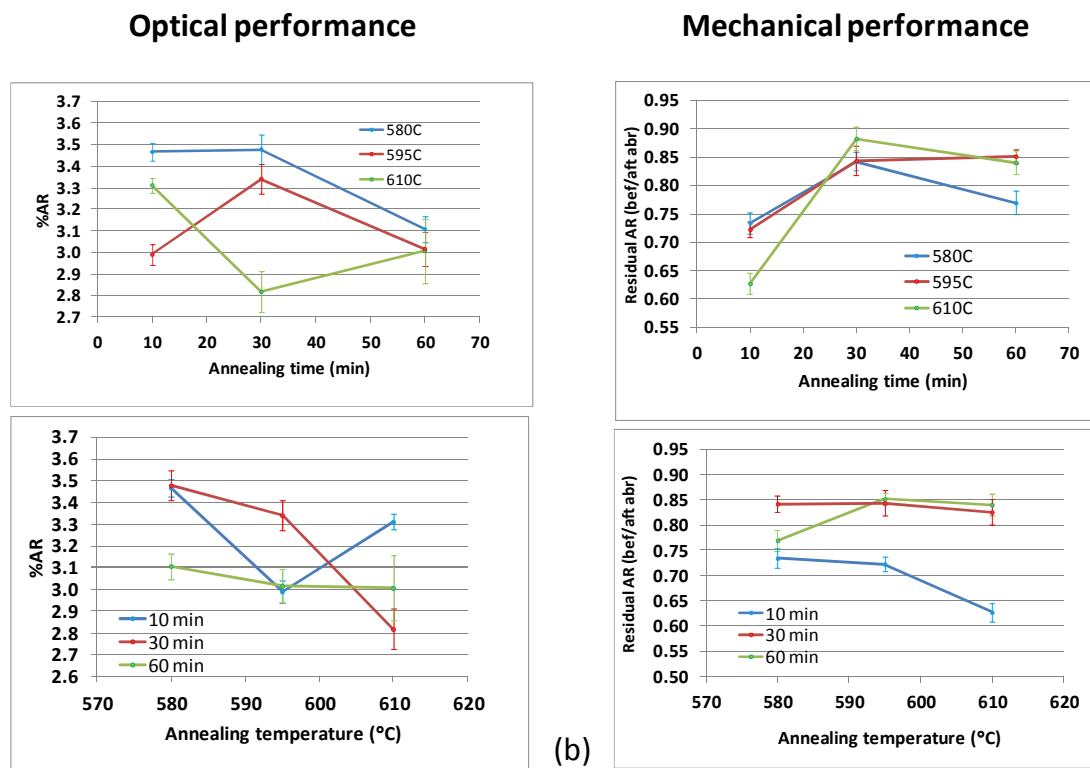


Figure 22. Performance indicators as a function of annealing time and temperature for a) 1L and b) 3L

Overall it can be noted that the best 3L condition (580°C at 30 minutes) had better abrasion resistance at ~85% mean residual AR compared to ~82% for the best 1L condition (580°C at 60 minutes) although according to the standard error, this may not be significant. Also the mean AR for the best 3L was 3.48% (6% higher) while the best 1L had 3.27% which appears to be significant according to the plots. Cummings et al suggested that if there is an overlap between the two standard error bars with the samples sizes being equal, then the difference in the values are statistically not significant [45]. The opposite cannot be said if the error bars do not overlap.

An ANOVA was performed on this data to understand the significance of annealing time and temperature as well as their interaction. These results are summarized in Table 12 below.

Table 12. Analysis of variance on annealing parameters

Analysis of Variance for Mean %AR

Source	DF	F	P
Blocks	8	1.000	0.449
Temperature	2	0.930	0.401
Time	2	3.470	0.038
Temperature*Time	4	3.760	0.009
Error	58		
Outliers	7		
Total	81		

Source	DF	F	P
Blocks	8	2.16	0.043
Temperature	2	16.26	0.000
Time	2	8.74	0.000
Temperature*Time	4	15.83	0.000
Error	61		
Outliers	4		
Total	81		

Analysis of Variance for Residual %AR

Source	DF	F	P
Blocks	8	2.17	0.043
Temperature	2	2.9	0.063
Time	2	53.6	0.000
Temperature*Time	4	2.3	0.069
Error	58		
Outliers	7		
Total	81		

Single layer

Source	DF	F	P
Blocks	8	0.44	0.894
Temperature	2	1.45	0.243
Time	2	60.27	0.000
Temperature*Time	4	7.88	0.000
Error	61		
Outliers	4		
Total	81		

Three layer

Variables that significantly affect the performance indicators are identified in green based on low P-values. Further, non-linear regression models were used to further evaluate the effects of annealing time and temperature on the two film structures. Table 13 gives a summary of the regression models with their corresponding R- squared values suggesting that additional factors are affecting the optical and mechanical properties of the film.

Table 13. Regression models describing performance indicators as function of time and temperature

Structure	Regression type	Fit	R-sq %
1 layer	Quadratic	$\text{Mean AR} = 65.2252 - 0.21175 \cdot \text{Temperature} + 0.103762 \cdot \text{Time} + 0.000181083 \cdot \text{Temperature} \cdot \text{Temperature} - 0.000172746 \cdot \text{Time} \cdot \text{Temperature} - 6.04341 \cdot 10^{-5} \cdot \text{Time} \cdot \text{Time}$	16.1
	Quadratic	$\text{Residual AR} = 9.41051 - 0.0319331 \cdot \text{Temperature} + 0.0313593 \cdot \text{Time} + 2.89203 \cdot 10^{-5} \cdot \text{Temperature} \cdot \text{Temperature} - 4.81531 \cdot 10^{-5} \cdot \text{Time} \cdot \text{Temperature} - 2.32052 \cdot 10^{-6} \cdot \text{Time} \cdot \text{Time}$	59.7
3 layer	Quadratic	$\text{Mean AR} = 177.139 - 0.571977 \cdot \text{Temperature} - 0.0859161 \cdot \text{Time} + 0.000469836 \cdot \text{Temperature} \cdot \text{Temperature} + 0.000152901 \cdot \text{Time} \cdot \text{Temperature} - 0.000122271 \cdot \text{Time} \cdot \text{Time}$	28.1
	Quadratic	$\text{Residual AR} = -34.6398 + 0.122214 \cdot \text{Temperature} - 0.0516549 \cdot \text{Time} - 0.00010592 \cdot \text{Temperature} \cdot \text{Temperature} + 0.000111835 \cdot \text{Time} \cdot \text{Temperature} - 0.000176815 \cdot \text{Time} \cdot \text{Time}$	65.9

Interestingly, according to this data, temperature seems to have little impact on the mechanical performance of the films and may actually decrease mechanical performance at higher temperature. The mechanical properties of the film seem to have more to do with the annealing time. This is corroborated by the ANOVA which shows that only time influences the mechanical performance of the single layer film, while for the three layer film, not only time but also the interaction of time and temperature may be significant. The mechanical response of the single layer film is highly non-linear with time while the three layer film shows a linear response. The optical performance of the films appears to decrease with time. Unfortunately, this suggests that high optical performance generally leads to low mechanical performance and vice versa.

Based on Figure 22, three conditions for each film structure were chosen for further structure-property analysis. As shown in Table 14, the three conditions consisted of the

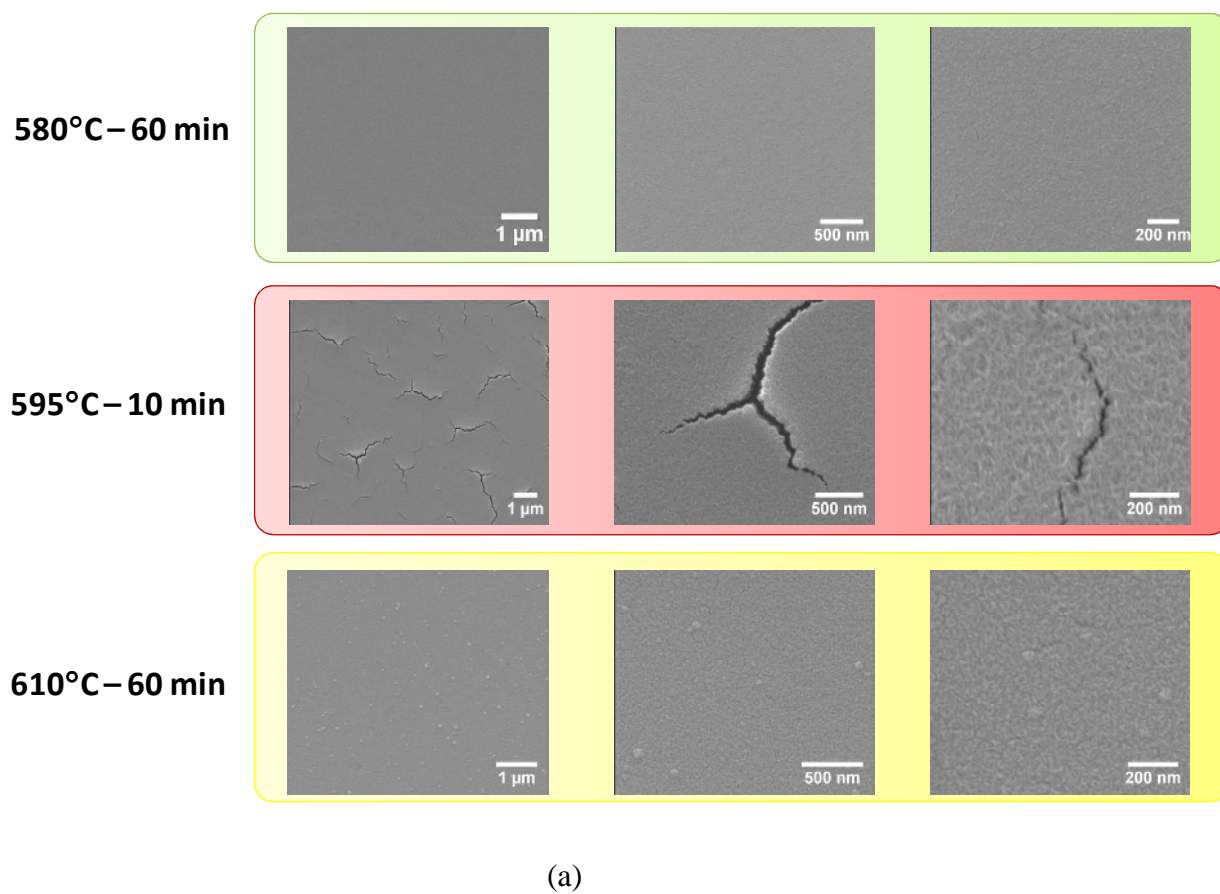
best, worst and in between conditions in terms of optical and mechanical performance. For the in-between level, a film condition having low optical performance but high mechanical performance was selected for further examination.

Table 14. Film conditions selected for structural analysis

Structure	Film condition	Rationale
Single layer (1L)	580°C – 60 min	High optical & High mechanical
	595°C – 10 min	Low optical & Low mechanical
	610°C – 60 min	Low optical & High mechanical
Three layer (3L)	580°C – 30 min	High optical & High mechanical
	595°C – 10 min	Low optical & Low mechanical
	610°C – 30 min	Low optical & High mechanical

3.3.2. Film structure

The structure of the six films was examined by scanning electron microscopy (SEM) and transmission electron microscopy (TEM). SEM images were taken of the top surface of the films. TEM images were taken of film cross sections prepared using the dual beam FIB. Figure 23 and Figure 25 depict the high magnification images thus collected.

**Figure 23**

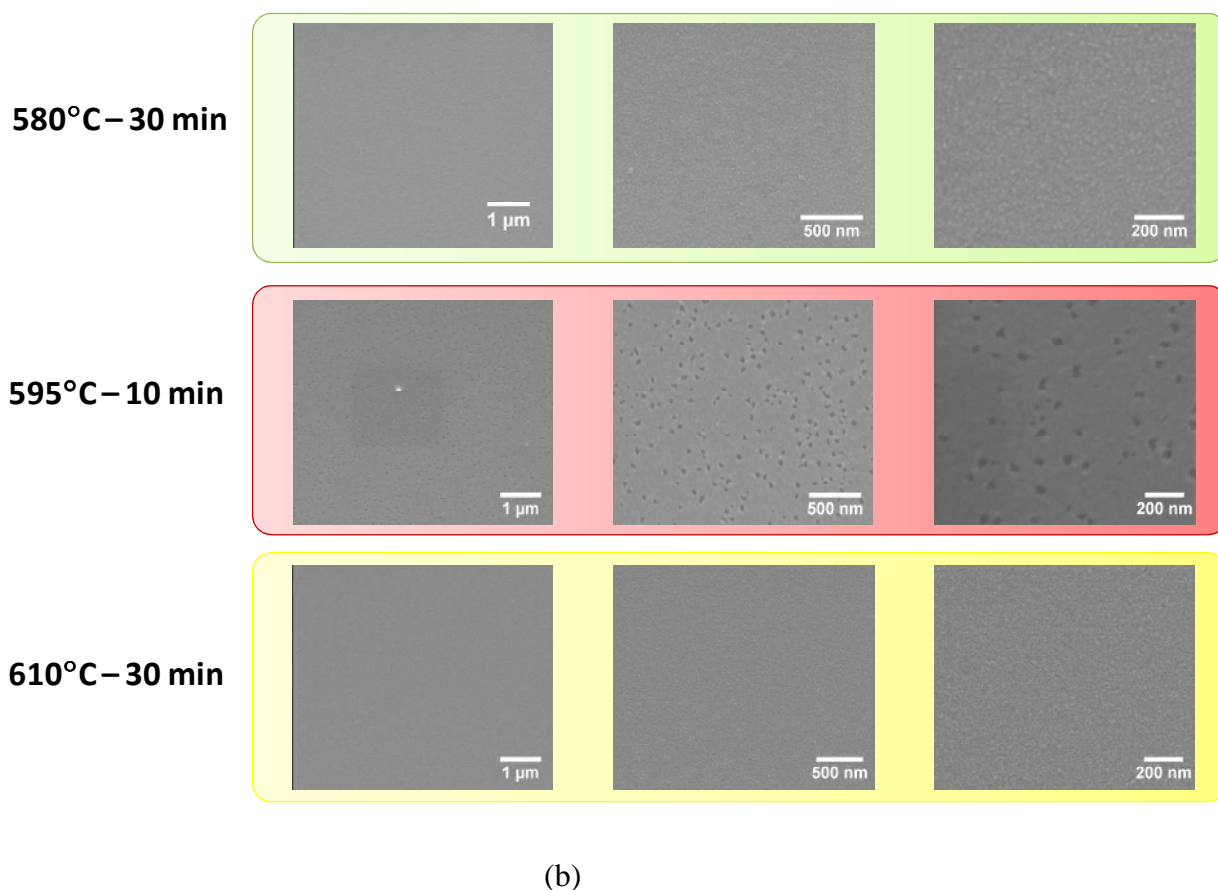


Figure 23. Top surface scanning electron micrographs of the films a) 1L and b) 3L. Green, red, and yellow conditions are shown from top to bottom

In 1L films made at 595C for 10 mins, large tripod-shaped cracks can be seen which appear to follow a bimodal distribution. It is likely that these cracks were caused by the changing density of the film in combination with any thermal stresses caused by a coefficient of thermal expansion mismatch between the substrate and the film. Further, based on the differential scanning calorimetry and mass spectrometry data shown in Figure 24, annealing of the 1L film leads to the release of volatile constituents like organics and water vapor which could have contributed to cracking during volatilization.

In order to evaluate this phenomenon and to study the annealing mechanism, a typical annealing cycle at 580°C for 1 hour was carried out using the furnace in a DSC/TGA unit. The maximum ramp rate for the unit was ten times slower at 50°C/min compared to the rapid thermal annealing unit typically used for annealing coated glass samples. For ease of sample preparation, silicon wafer was used as a substrate.

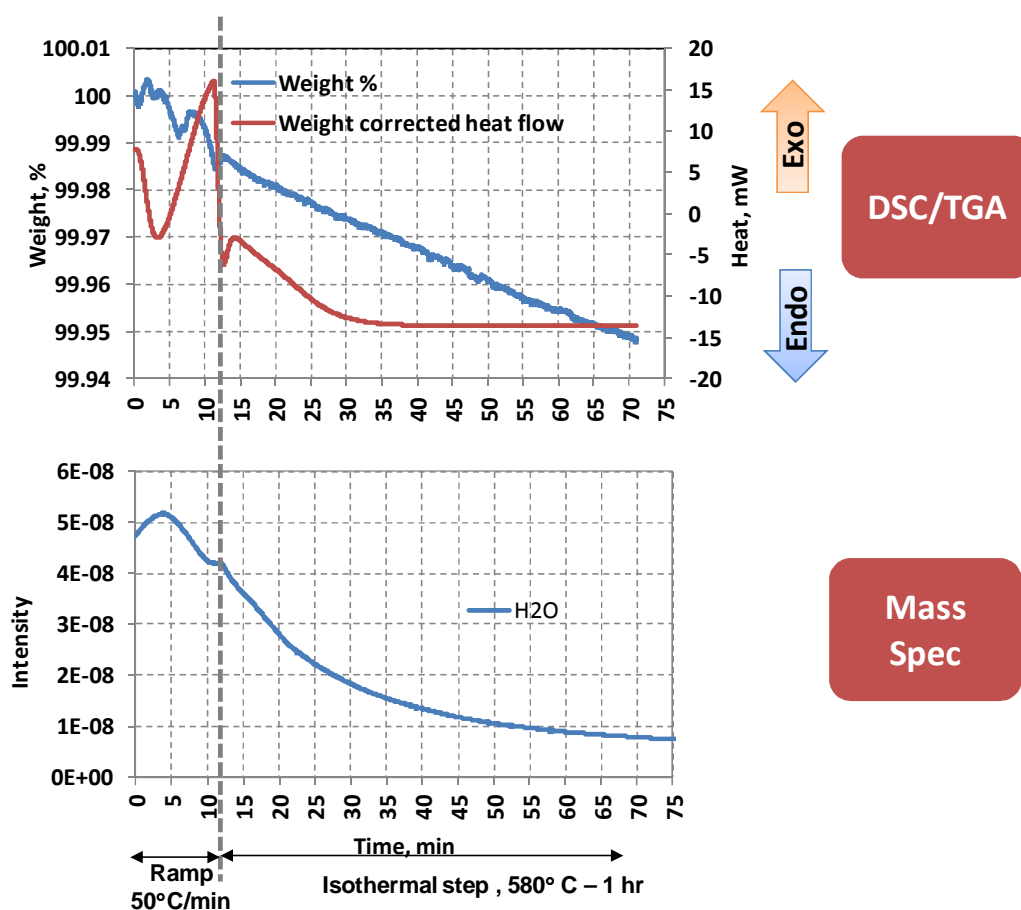


Figure 24. Simultaneous DSC/TGA and Mass Spec analysis during annealing of single layer TMOS-NP-base gel film

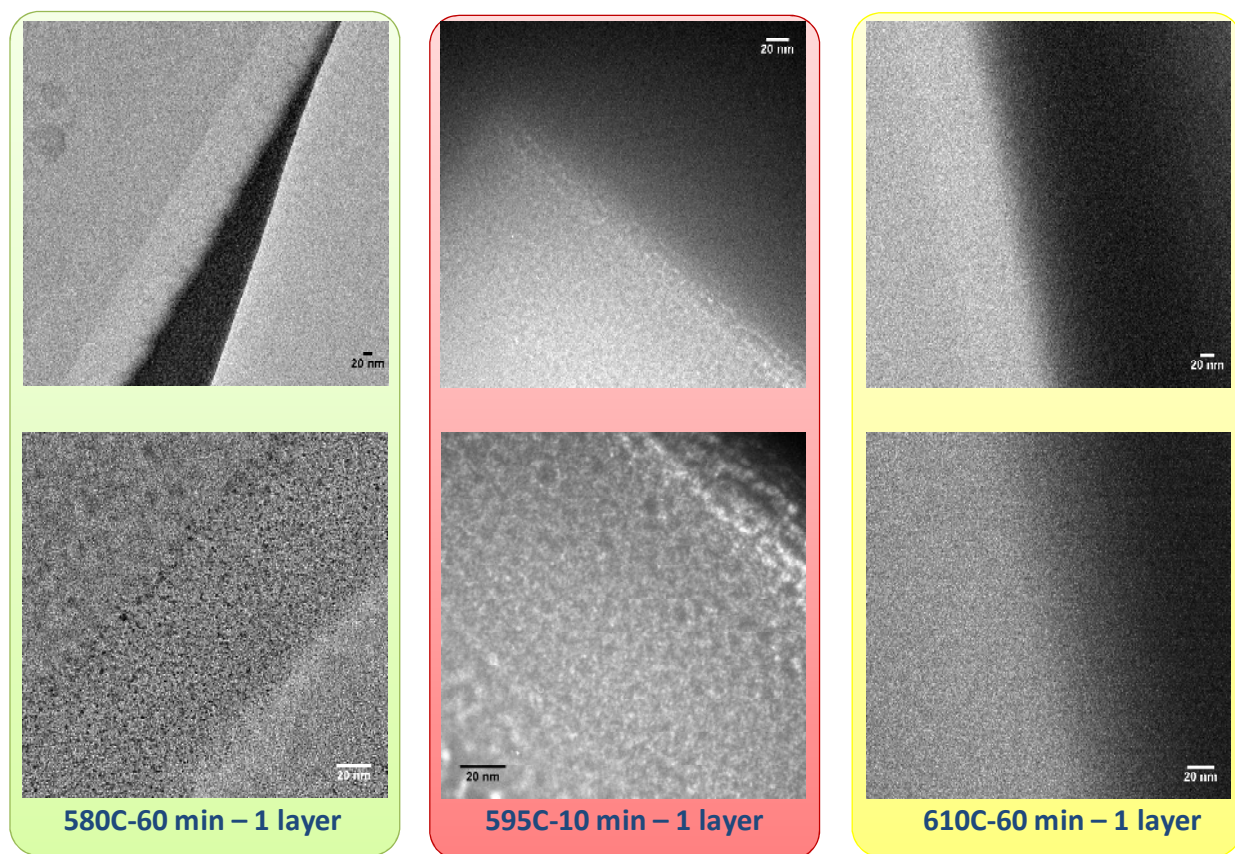
From the DSC curve it can be seen that there is an endothermic dip associated with removal of water around 150°C. This also corresponds to the mass spec curve wherein

the evolution of water over time was tracked during the entire annealing cycle of the sample. Absorbed water on the sample is removed by simple dehydration and peaks around the same temperature. A chemical transition appears to be happening as temperature is increased from 250°C to the annealing temperature of 580°C shown by the exothermic spike. It is hypothesized that this is a reaction step before the Si-O-H bonds are terminated. Subsequent hold at 580°C shows that water is still coming out until 30 minutes during annealing and water evolution is near constant beyond 30 minutes. Since this occurs at temperatures well above dehydration it is hypothesized that these water molecules are derived from the condensation reaction resulting from termination of Si-O-H bonds to form Si-O bonds. The corresponding plateau in the DSC curve suggests constant heat intake to maintain 580°C temperature in the sample. There is continuous weight reduction in the TGA curve suggesting constant out gassing from the sample

Going forward, the absence of cracks at 610°C for the 1L films suggests that longer annealing times in combination with higher temperatures may result in stress relief or, alternatively, the “healing” of cracks via sintering. The high magnification image at 610°C for 60 mins shows signs of nanocracks that may have healed. Softening of the film at higher temperatures could cause the film to flow under viscous creep bringing the film back together which would have sintered more rapidly at the higher temperature. Clustering from particle coarsening is also seen under these conditions suggesting rapid sintering.

For 3L films produced at 595°C for 10 mins, pores averaging less than 100 nm are uniformly distributed across the surface. It is apparent that the presence of preexisting cracks and widely distributed pores can reduce the hardness of the films and lower mechanical properties. At higher temperatures, both 1L and 3L films appear to be very dense leading to the loss in definition of nanofeatures which could explain the loss in optical performance with increasing mechanical performance.

The TEM cross-sectional images reveal other structural detail as shown in Figure 25. In the TEM cross section, several layers are observed. The darkest layer is the top surface of the sample consisting of a PVD chromium layer deposited for the purpose of protecting the sample during FIB milling. The carbon layer is added as a contrast differentiation between the actual sample surface and the chromium layer.



(a)

Figure 25

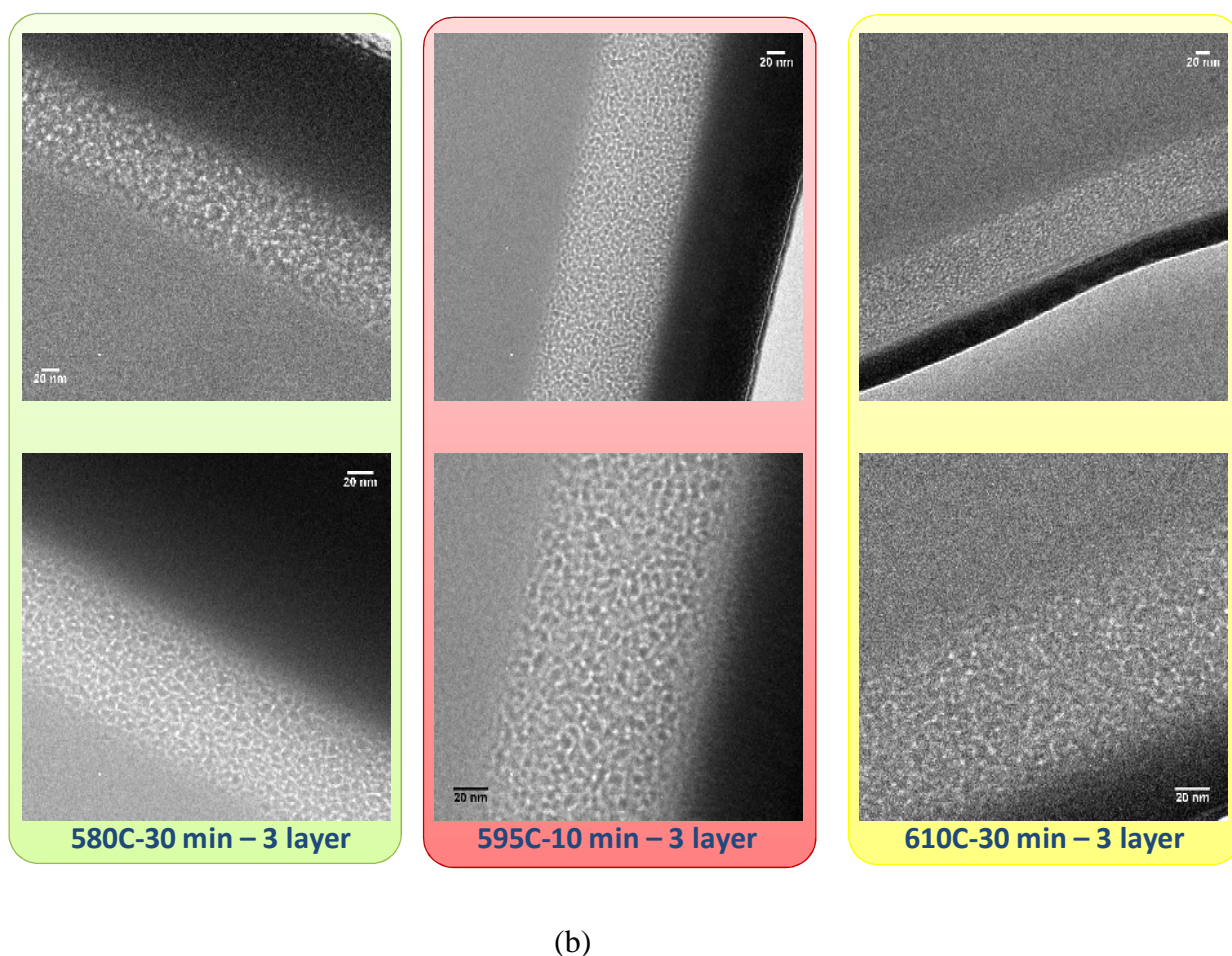


Figure 25. Cross sectional transmission electron micrographs of the films a) 1L and b) 3L. Green, red, and yellow conditions are shown from left to right

In Figure 9a, the black dots seen within the high magnification image of the TMOS-b layer cross-section produced at 580°C for 60 mins are nanoparticles (NPs). At 580°C for 60 mins, there appears to be a NP size gradient which is larger near the film-substrate interface. The NPs appear to cluster as annealing temperature increases. The NP clusters seen at 595°C for 10 minutes appear to be nearly uniform in size and distribution. The sintering effect is apparent at the highest annealing temperature and time (610°C for 60

minutes) showing lack of distinct features. At this annealing condition, the coating behavior approaches that of bulk glass.

In Figure 25b, the three layers of TMOS-based coating are identifiable at higher magnification. The white patches that are visible are the Si-based polymer matrix. The 3L films appear to have a denser distribution of NP clusters than found at the 595°C condition in the 1L film. There appears to be a bidirectional gradient of the NP clustering in the sample exposed to 580°C for 30 minutes with larger clusters especially at the bottom of the film. This structure is not found in the other two 3L samples.

3.3.3. Mechanical behavior of ARC films

The six sample conditions identified above were subjected to nanoindentation and single point microscratch tests to study the mechanical behavior of these films. The nanoindentation tests provided the indentation hardness and elastic modulus of the films as shown in Figure 26 below.

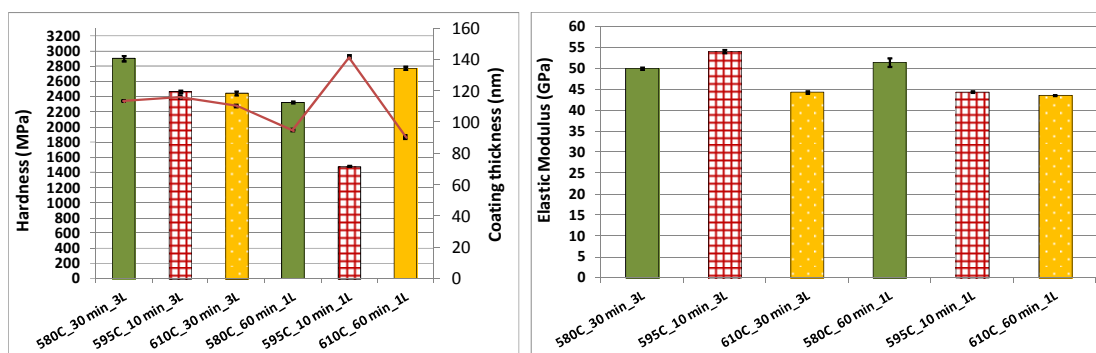


Figure 26. Mechanical properties of 1L and 3L Line plot on the left shows the coating thickness

[– Best, – Worst, – Mid].

Using the nomenclature developed above, the ‘best’ films (solid green) were found to have better hardness and similar modulus in comparison to the ‘worst’ films (hatched red). The ‘in-between’ films (dotted yellow) had mechanical properties comparable to the green films. While these material properties do not explain the mechanical behavior of the films alone, the harder films tended to perform better mechanically. This may suggest the suppression of crack nucleation. The coating thickness measured from the cross-sectional TEM images was overlaid as a line plot onto the hardness values. There appears to be an inverse trend between coating thickness and hardness.

These material properties along with other derived parameters were used to evaluate the important mechanical properties defined earlier. Results are shown in Figures 27-29.

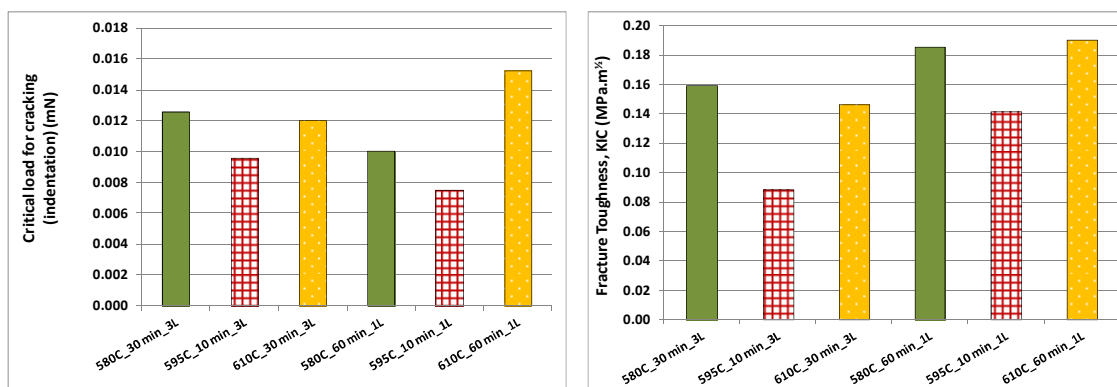


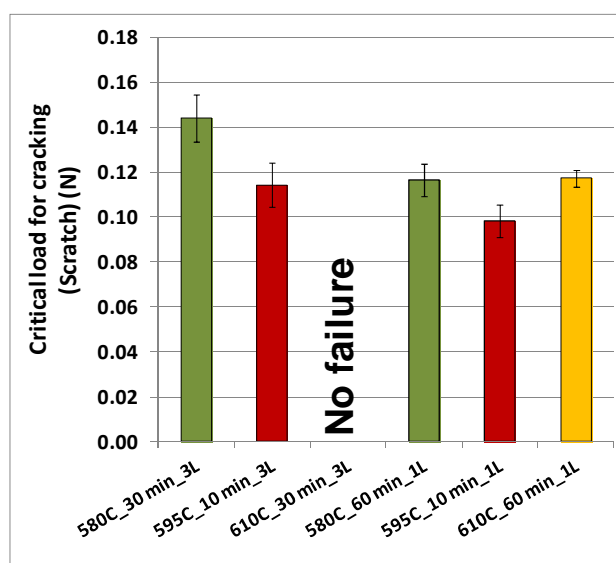
Figure 27. Crack resistance depicted as critical load for cracking under indentation and fracture toughness

The critical load for cracking was computed using Equation 1 which is a function of coating hardness, elastic modulus and the penetration depth of the indenter. It is a strong function of the penetration depth and lesser the penetration depth. Fracture toughness on

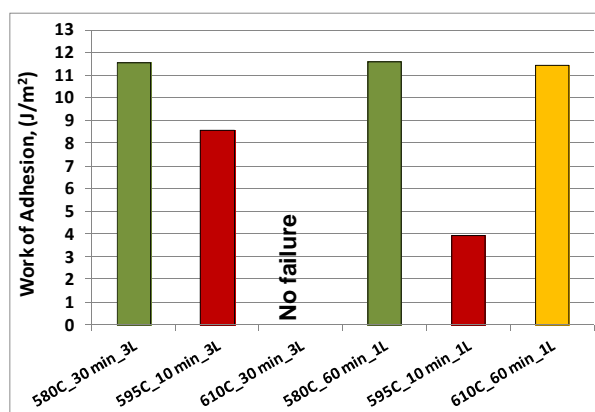
the other hand can be thought of as a material property and is also dependent on the modulus and hardness. However it is a stronger function of the length of the radial cracks which appear to grow perpendicular to the direction of loading. This is basically the energy required to nucleate a crack and hence dictates the crack resistance of the coating. The penetration depth indirectly affects the crack size as well.

Crack nucleation results appear to follow abrasion resistance results. The best 3L film (green) has 30% higher critical load for cracking (P) defined as a measure of crack nucleation resistance compared to the best 1L film (green). It is expected that the 3L has better crack nucleation resistance largely due to higher hardness. This is consistent with the larger nanoparticles found in the TMOS-b layer for the 3L film. It is interesting that the fracture toughness does not follow abrasion resistance results suggesting that crack nucleation may be a more important factor in determining the abrasion resistance of the films. The fracture toughness of the best 1L film (580°C-60 min) is about 16% higher than that of the best 3L film (580°C-30 min) on average which appears to be significant. The reduced fracture toughness may be due to the porosity observed in the 3L film compared with the nanoparticles being the major phase observed in the 1L film. It is also possible that the 3L coatings have a lower fracture toughness compared to 1L coatings due to the amorphous TMOS-a layer on top which provides lower resistance to crack propagation than the continuous layer filled with crystalline nanoparticles. Since in an indentation test the radial crack initiation is directly below the indenter tip and observing that the average depth of penetration for these films is about 45 nm, we can conclude that crack nucleation occurs within the TMOS-b layer on both 3L and 1L. The amorphous

TMOS-a layer appears to be detrimental to crack propagation resistance. The samples at 595°C and 10 mins are weaker in both structures. Since the in-between level samples selected had high mechanical performance, it follows that these films have better crack resistance as well.



(a) -



(b)

Figure 28. Scratch resistance depicted using critical loads (LC1) and delamination resistance depicted using work of adhesion

Figure 28 shows the results derived from the models described earlier for scratch resistance and delamination resistance. Scratch resistance can be thought of as a resistance for crack propagation and while delamination resistance affects crack propagation as well when it reaches an interface. The critical loads reported in Figure 28a are experimentally measured while the work of adhesion is derived from Equation 7. Work of adhesion is basically the work done in separating two materials from each other and hence in this case is a function depicting the film-substrate interaction. The work of adhesion is a function of the friction coefficient which was determined by the scratch test. From Figure 7b, it is again apparent that the worst film is indeed worst in scratch and delamination resistance as well. It is to be highlighted that the high mechanical performance coating made at 610°C for 30 minutes did not fail under the testing conditions maintained for the other samples. The friction coefficient for this coating condition was also the lowest at 0.03 while the rest had above 0.08. The values calculated for W_a were found to be comparable to that reported by others for similar coatings [46, 47].

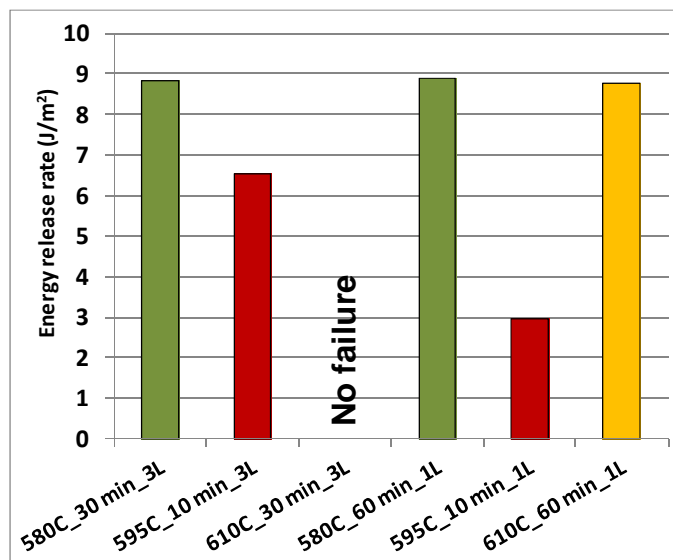


Figure 29. Spallation resistance depicted using strain energy release rate

In Figure 29, the spallation resistance of the various coatings is shown based on Equation 8 for the strain energy release rate during crack growth. This graph is similar to the prior two graphs showing the strain energy release rate is generally higher for the three layer film. It is expected that the acid gel allows for better structural transition from the substrate to the film thus improving the adhesion in contrast to the sharp change in material composition and structure in the 1L film.

Upon reviewing all the metrics, the best 3L film had better optical performance than the best 1L film, slightly better abrasion resistance (based on residual AR), better crack nucleation resistance, scratch resistance, delamination resistance and spallation resistance. The optical performance and delamination resistance is primarily attributed to the smoother transition in structure and density from substrate to the coating which

primarily arose from lower thermal gradients during annealing. The key to better abrasion resistance is the better crack nucleation resistance which is

4. Conclusions

Overall, the mechanistic models developed for describing thin film behavior appear to adequately describe the abrasion resistance for the gradient ARCs described in this paper. Several inferences can be drawn from this work. First, the abrasion resistance of gradient ARCs can be decoupled from the optical characteristics of these coatings through clever design. The processing of the films affects the structure of the films and ultimately differentiates the films in terms of performance. The presence of defects such as pores and cracks in the coatings caused during annealing reduced the mechanical performance of the coatings. Results show that the abrasion resistance of the three layer coating was better because of superior hardness and crack nucleation resistance. In addition, the 3L structure enhanced the interfacial properties like work of adhesion and energy release rate. The glass is an amorphous structure and TEM results show that the TMOS-a is mainly amorphous. Thus a shallower structural gradient and density gradient at the interface in 3L compared to 1L improves the delamination resistance while the same soft TMOS-a layer on top reduces fracture toughness (crack propagation) in the 3L coating. Overall the abrasion resistance as well as the optical performance of the 3L coating was found to be superior to the 1L coating.

5. References

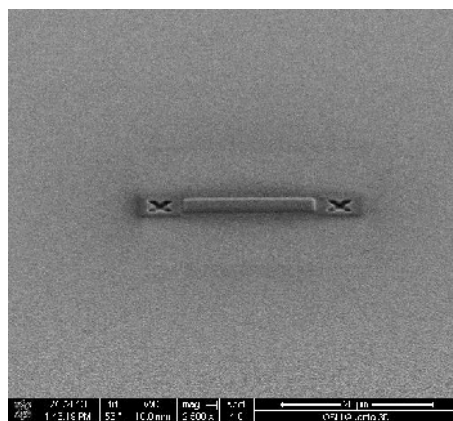
- [1] Gombert, A., Glaubitt, W., Rose, K., Dreibholz, J., Bläsi, B., Heinzel, A., Sporn, D., Döll, W., and Wittwer, V., 1999, "Subwavelength-structured antireflective surfaces on glass," *Thin Solid Films*, 351(1–2), pp. 73-78.
- [2] Raut, H. K., Ganesh, V. A., Nair, A. S., and Ramakrishna, S., 2011, "Anti-reflective coatings: A critical, in-depth review," *Energy & Environmental Science*, 4(10), pp. 3779-3804.
- [3] Kuhr, M., Bauer, S., Rothhaar, U., and Wolff, D., 2003, "Coatings on plastics with the PICVD technology," *Thin Solid Films*, 442(1), pp. 107-116.
- [4] Martinu, L., and Poitras, D., 2000, "Plasma deposition of optical films and coatings: A review," *Journal of Vacuum Science & Technology A: Vacuum, Surfaces, and Films*, 18(6), pp. 2619-2645.
- [5] Bernhard, C., Boethius, J., Gemne, G., and Struwe, G., 1970, "Eye ultrastructure, colour reception and behaviour."
- [6] Bernhard, C. G., Gemne, G., and Sällström, J., 1970, "Comparative ultrastructure of corneal surface topography in insects with aspects on phylogenesis and function," *Journal of Comparative Physiology A: Neuroethology, Sensory, Neural, and Behavioral Physiology*, 67(1), pp. 1-25.
- [7] Dobrowolski, J. A., 1995, "Optical properties of films and coatings," *Handbook of Optics*, 1, pp. 42.41-42.130.
- [8] Glaser, T., Ihring, A., Morgenroth, W., Seifert, N., Schröter, S., and Baier, V., 2005, "High temperature resistant antireflective moth-eye structures for infrared radiation sensors," *Microsystem technologies*, 11(2), pp. 86-90.
- [9] Sun, C. H., Jiang, P., and Jiang, B., 2008, "Broadband moth-eye antireflection coatings on silicon," *Applied Physics Letters*, 92(6), pp. 061112-061112-061113.
- [10] Minot, M. J., 1976, "Single-layer, gradient refractive index antireflection films effective from 0.35 to 2.5 μ ," *JOSA*, 66(6), pp. 515-519.
- [11] Chaoui, R., Mahmoudi, B., and Si Ahmed, Y., 2008, "Porous silicon antireflection layer for solar cells using metal-assisted chemical etching," *physica status solidi (a)*, 205(7), pp. 1724-1728.
- [12] Yanagishita, T., Nishio, K., and Masuda, H., 2009, "Anti-reflection structures on lenses by nanoimprinting using ordered anodic porous alumina," *Applied physics express*, 2(2), p. 2001.
- [13] Katayama, Y., Ando, E., and Kawaguchi, T., 1992, "Characterization of SiO₂ films on glass substrate by sol-gel and vacuum deposition methods," *Journal of non-crystalline solids*, 147, pp. 437-441.
- [14] Haereid, S., Dahle, M., Lima, S., and Einarsrud, M. A., 1995, "Preparation and properties of monolithic silica xerogels from TEOS-based alcogels aged in silane solutions," *Journal of non-crystalline solids*, 186, pp. 96-103.
- [15] Chen, D., 2001, "Anti-reflection (AR) coatings made by sol-gel processes: a review," *solar energy materials and solar cells*, 68(3), pp. 313-336.

- [16] Cook, R. F., and Pharr, G. M., 1990, "Direct Observation and Analysis of Indentation Cracking in Glasses and Ceramics," *Journal of the American Ceramic Society*, 73(4), pp. 787-817.
- [17] Mittal, K., and Kern, W., 1987, "Selected bibliography on adhesion measurement of films and coatings," *Journal of Adhesion Science and Technology*, 1(1), pp. 247-262.
- [18] Vossen, J., 1978, "Adhesion Measurement of Thin Films, Thick Films and Bulk Coatings," *ASTM Spec. Tech. Publ*, 640, pp. 122-131.
- [19] Davies, P., Blackman, B. R. K., and Brunner, A. J., 1998, "Standard Test Methods for Delamination Resistance of Composite Materials: Current Status," *Applied Composite Materials*, 5(6), pp. 345-364.
- [20] Malzbender, J., de With, G., and den Toonder, J. M. J., 2000, "Determination of the elastic modulus and hardness of sol-gel coatings on glass: influence of indenter geometry," *Thin Solid Films*, 372(1-2), pp. 134-143.
- [21] Malzbender, J., de With, G., and den Toonder, J. M. J., 2000, "Elastic modulus, indentation pressure and fracture toughness of hybrid coatings on glass," *Thin Solid Films*, 366(1-2), pp. 139-149.
- [22] Anstis, G., Chantikul, P., Lawn, B. R., and Marshall, D., 1981, "A critical evaluation of indentation techniques for measuring fracture toughness: I, direct crack measurements," *Journal of the American Ceramic Society*, 64(9), pp. 533-538.
- [23] Nastasi, M. A., Parkin, D. M., and Gleiter, H., 1993, *Mechanical properties and deformation behavior of materials having ultra-fine microstructures*, Springer.
- [24] Malzbender, J., de With, G., and den Toonder, J., 2000, "The $P-h^2$ relationship in indentation," *Journal of materials research*, 15(05), pp. 1209-1212.
- [25] Gerberich, W., Mook, W., Carter, C., and Ballarini, R., 2007, "A crack extension force correlation for hard materials," *International Journal of Fracture*, 148(2), pp. 109-114.
- [26] Bull, S. J., 2011, "Analysis methods and size effects in the indentation fracture toughness assessment of very thin oxide coatings on glass," *Comptes Rendus Mecanique*.
- [27] Bull, S. J., Rickerby, D. S., Matthews, A., Leyland, A., Pace, A. R., and Valli, J., 1988, "The use of scratch adhesion testing for the determination of interfacial adhesion: The importance of frictional drag," *Surface and Coatings Technology*, 36(1-2), pp. 503-517.
- [28] Blees, M. H., Winkelman, G. B., Balkenende, A. R., and den Toonder, J. M. J., 2000, "The effect of friction on scratch adhesion testing: application to a sol-gel coating on polypropylene," *Thin Solid Films*, 359(1), pp. 1-13.
- [29] Attar, F., and Johannesson, T., 1996, "Adhesion evaluation of thin ceramic coatings on tool steel using the scratch testing technique," *Surface and Coatings Technology*, 78(1), pp. 87-102.
- [30] Evans, A., and Hutchinson, J., 1984, "On the mechanics of delamination and spalling in compressed films," *International Journal of Solids and Structures*, 20(5), pp. 455-466.
- [31] Hutchinson, J., and Suo, Z., 1992, "Mixed mode cracking in layered materials," *Advances in applied mechanics*, 29(63), p. 191.

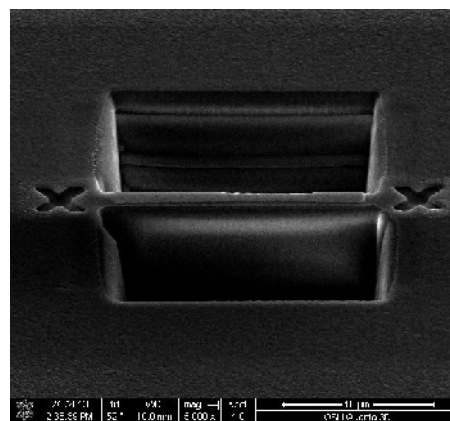
- [32] Rickerby, D., 1988, "A review of the methods for the measurement of coating-substrate adhesion," *Surface and Coatings Technology*, 36(1), pp. 541-557.
- [33] Laugier, M. T., 1984, "An energy approach to the adhesion of coatings using the scratch test," *Thin Solid Films*, 117(4), pp. 243-249.
- [34] Liang, L., You, X., Ma, H., and Wei, Y., 2010, "Interface energy and its influence on interface fracture between metal and ceramic thin films in nanoscale," *Journal of Applied Physics*, 108(8), p. 084317.
- [35] Zou, M., and Yang, D., 2006, "Nanoindentation of silica nanoparticles attached to a silicon substrate," *Tribology letters*, 22(2), pp. 189-196.
- [36] Vong, M., and Sermon, P., 1997, "Observing the breathing of silica sol-gel-derived anti-reflection optical coatings," *Thin Solid Films*, 293(1), pp. 185-195.
- [37] Wongcharee, K., Brungs, M., Chaplin, R., Hong, Y., and Sizgek, E., 2002, "Scratch Resistance Improvement of Sol-Gel Derived Antireflective Coatings by Incorporation of Polyethylene Glycol in Acid Catalysed Sols," *Journal of the Australasian Ceramic Society*, 38(1), pp. 40-43.
- [38] Li, X., and Shen, J., 2011, "A scratch-resistant and hydrophobic broadband antireflective coating by sol-gel method," *Thin Solid Films*, 519(19), pp. 6236-6240.
- [39] Floch, H. G., and Belleville, P. F., "Scratch-resistant single-layer antireflective coating by a low-temperature sol-gel route."
- [40] Henning, S., and Svensson, L., 1981, "Production of silica aerogel," *Physica Scripta*, 23(4B), p. 697.
- [41] Hæreid, S., Anderson, J., Einarsrud, M., Hua, D., and Smith, D., 1995, "Thermal and temporal aging of TMOS-based aerogel precursors in water," *Journal of non-crystalline solids*, 185(3), pp. 221-226.
- [42] http://www.agc-solar.com/agc-solar-products/patterned-glass/solite.html#uid_2_tech.
- [43] Han, S.-Y., Paul, B. K., and Chang, C.-h., 2012, "Nanostructured ZnO as biomimetic anti-reflective coatings on textured silicon using a continuous solution process," *Journal of Materials Chemistry*, 22(43), pp. 22906-22912.
- [44] Masalov, V., Sukhinina, N., Kudrenko, E., and Emelchenko, G., 2011, "Mechanism of formation and nanostructure of Stöber silica particles," *Nanotechnology*, 22(27), p. 275718.
- [45] Cumming, G., 2007, "Inference by eye: Pictures of confidence intervals and thinking about levels of confidence," *Teaching Statistics*, 29(3), pp. 89-93.
- [46] Fabbri, P., Singh, B., Leterrier, Y., Månson, J.-A., Messori, M., and Pilati, F., 2006, "Cohesive and adhesive properties of polycaprolactone/silica hybrid coatings on poly (methyl methacrylate) substrates," *Surface and Coatings Technology*, 200(24), pp. 6706-6712.
- [47] Volinsky, A., Moody, N., and Gerberich, W., 2002, "Interfacial toughness measurements for thin films on substrates," *Acta Materialia*, 50(3), pp. 441-466.

Appendix 1

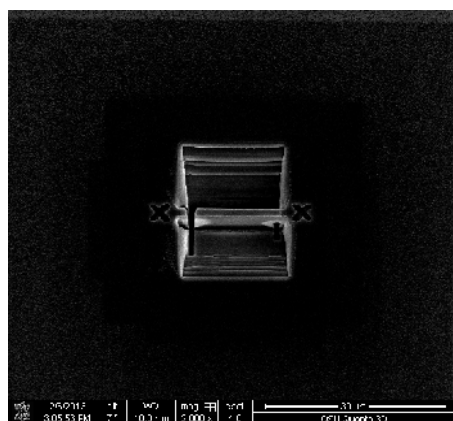
Step 1: Pt bar deposition



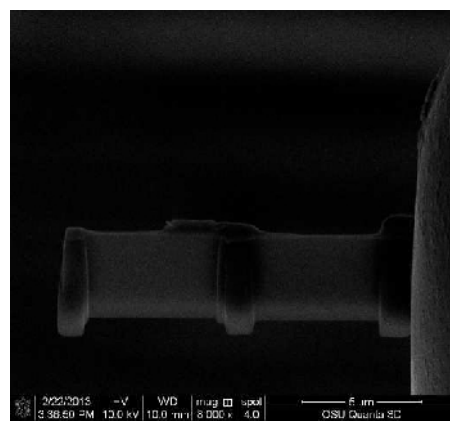
Step 2: Trench cut around membrane



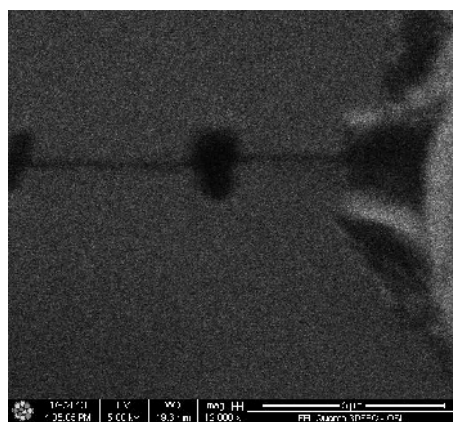
Step 3: J-cut before lift out



Step 4: Weld to Cu grid after lift out



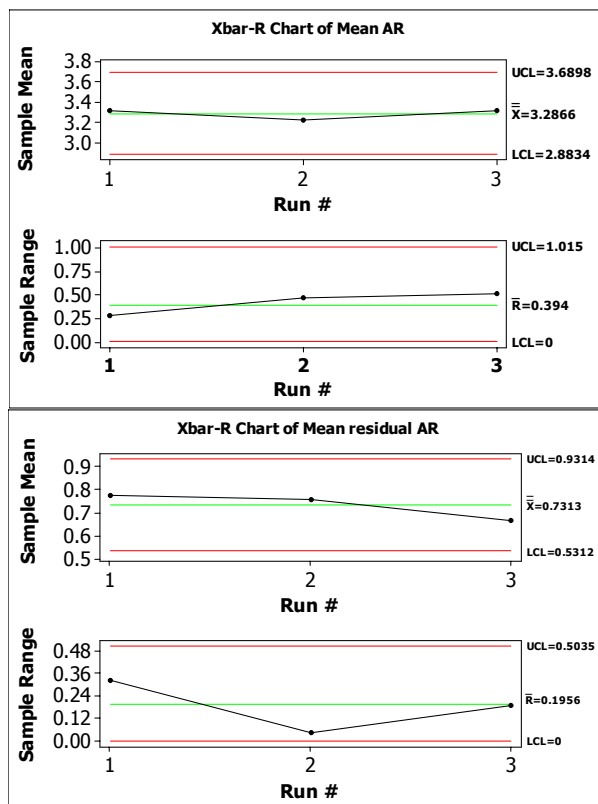
Step 5: Final thinning



Appendix 2

A2.1 Repeatability

In order to evaluate the link between structure-property-processing, the robustness of the processing steps and equipment needed to be tested. For this purpose a 3 layer ARC on glass comprising of TMOS-a/b/a was chosen to evaluate whether the process was in control. Nine ARC samples were fabricated spread across three runs to evaluate batch-batch variation.



a)

b)

Figure A2.1. Process control X-bar R charts based on a) Optical performance b) Mechanical performance

From the above charts it can be observed that the process appears to be within control as all the data points lie within upper and lower control limits both before and after ABR test. Thus any variation can be taken as random when a process is under control.

A2.2. Identify ARC structures that have equivalent optical performance but different mechanical behavior

In order to identify equivalent optical films a stage 1 general factorial design was created and is shown in table 1

Table A2.1 First level general factorial design

Std Order	Run Order	Recipe	Spin speed (rpm)
1	1	A	1500
5	2	B	1650
4	3	B	1500
2	4	A	1650
3	5	A	1800
6	6	B	1800

The above 6 runs were carried out for both films A and B with keeping the annealing conditions constant at 580°C for 1 hour. The design was replicated twice with 3 sample per each run to get improve statistical significance. Here, Mean AR and Mean residual AR were used as statistical indicators to evaluate the optical and mechanical performance. Based on the results a regression fit was performed to evaluate the influence of RPM on the indicators and is shown in Figure 4 and 5.

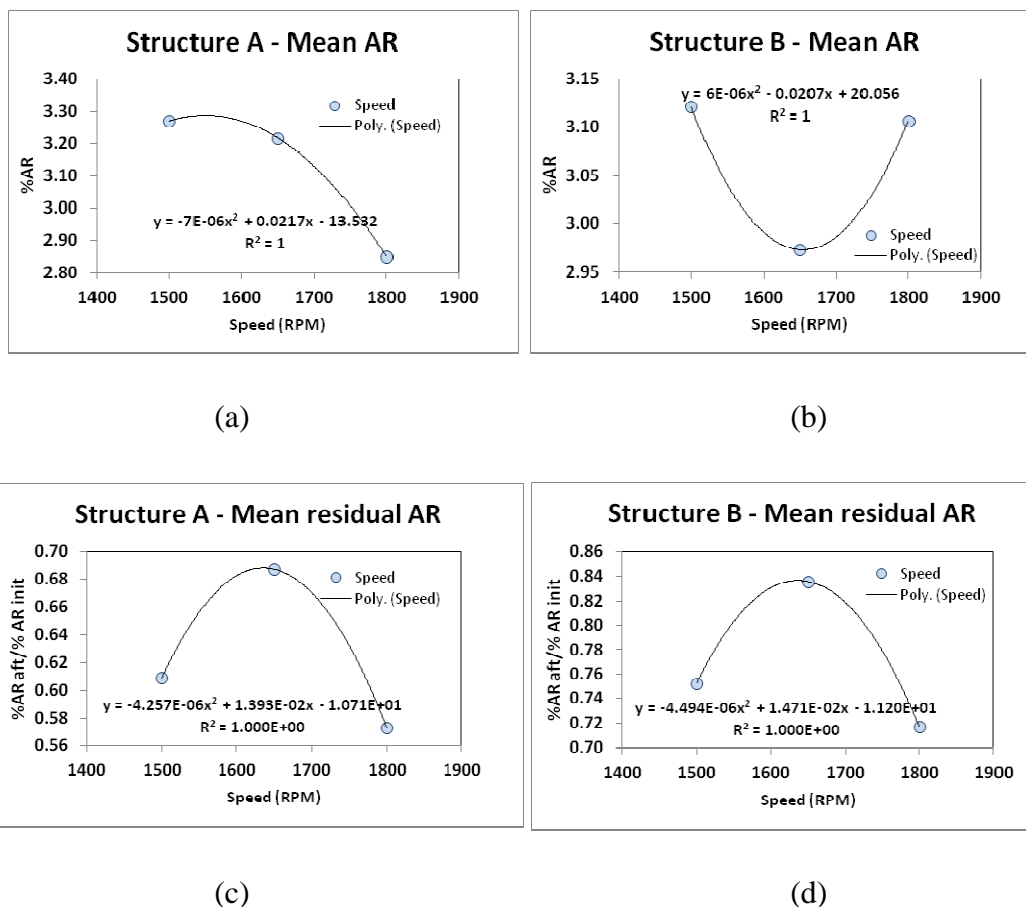
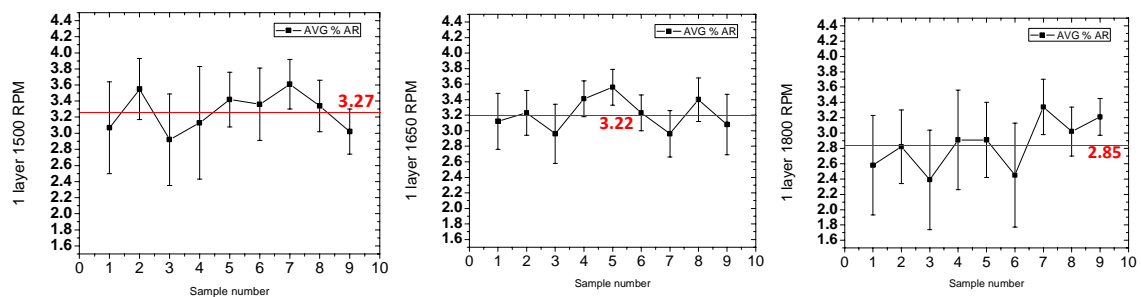


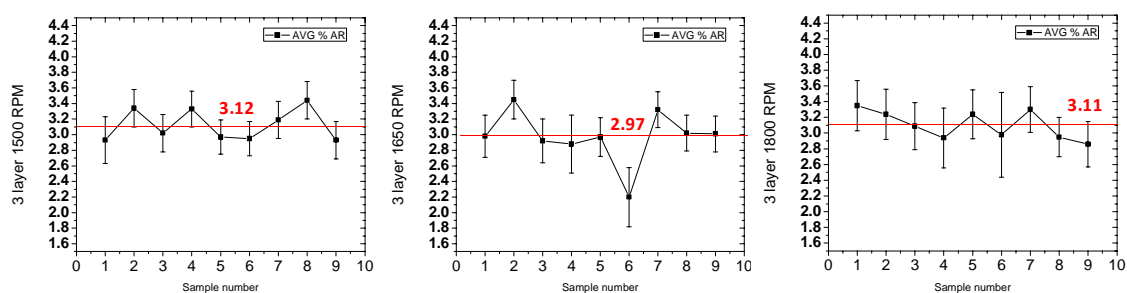
Figure A2.3. Non linear regression model describing the dependence of RPM on indicators a & b) Mean AR and c & d) Mean residual AR

It can be noted that the data doesn't follow a simple linear regression suggesting complex interaction between RPM and the indicators.

Further a point to point representation of the indicators for each experimental condition for the two structures was performed and is summarized in Figure 5 and 6.



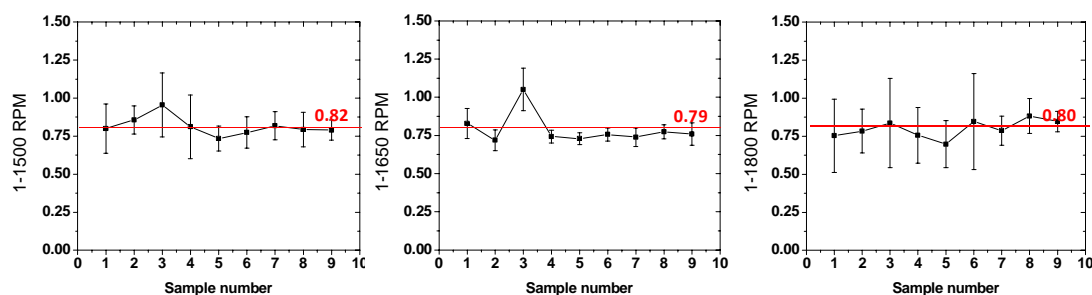
(a)



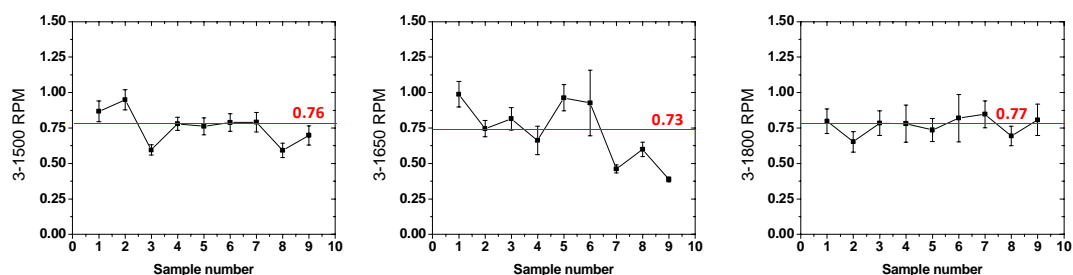
(b)

Figure A2.4. Sample to sample variation of Mean AR for a) Structure A and b) Structure B

(red line indicates mean across the 9 samples)



(a)



(b)

Figure A2.5. Sample to sample variation of Mean residual AR for a) Structure A and b) Structure B

(red line indicates mean across the 9 samples)

From the above plots, data was scrutinized to identify sample conditions with minimal sample to sample variation. Following that, it can be observed that 1500 RPM for structure A and 1800 RPM for structure were very similar in optical performance while they differed in mechanical performance. Thus these two films were taken forward for the next stage.